ISSN 1860-0387

PHD DISSERTATION 4 | 2019

PHD DISSERTATION 4 | 2019
Helmholtz Centre for Environmental Research – UFZ
Department of Solar Materials

Christian David

Biocatalyst design for 1,2-propanediol synthesis from CO_2 employing the photoautotrophic strain *Synechocystis* sp. PCC 6803

4 | 2019

HELMHOLTZ CENTRE FOR ENVIRONMENTAL RESEARCH – UFZ

Helmholtz Centre for
Environmental Research – UFZ
Permoserstraße 15
04318 Leipzig I Germany
www.ufz.de

Christian David | Biocatalyst design for 1,2-propanediol synthesis from CO_2 employing ...

Biocatalyst design for 1,2-propanediol synthesis from CO_2 employing the photoautotrophic strain *Synechocystis* sp. PCC 6803

Von der Fakultät Maschinenwesen

der Technischen Universität Dresden

genehmigte

DISSERTATION

zur Erlangung des akademischen Grades

Doktor der Ingenieurwissenschaften

(Dr.-Ing.)

vorgelegt von

Dipl.-Ing. Christian David

geboren am 31.08.1983 in Meerbusch

Gutachter: Prof. Dr. Katja Bühler (Technische Universität Dresden)

Prof. Dr. Thomas Walther (Technische Universität Dresden)

Prof. Dr. Annegret Wilde (Universität Freiburg)

Tag der Verteidigung: 12.04.2019

Acknowledgements

After five years of Ph.D. studies, a long journey has finally come to an end. The research for this thesis started five years ago back in Dortmund at the Laboratory of Chemical Biotechnology and was finally concluded in Leipzig at the Department of Solar Materials. During these five years in Dortmund and Leipzig, I learned a lot, and I had the privilege to work with many colleagues to whom I would like to express my gratitude.

First and foremost, I would like to thank my supervisor Prof. Katja Bühler for inviting me to be part of her research group. Thank you, Katja, for your guidance and support during these past few years. You introduced me to the world of catalytic biofilms and encourage me by always staying positive, giving constructive criticism, and lots of good advice. Thank you for seeing the finishing line when I could not.

I also wish to thank Prof. Andreas Schmid for welcoming me to his new Department at the Helmholtz Centre for Environmental Research and for introducing me to the new world of photosynthetic biocatalysis.

Especially, I wish to thank Prof. Annegret Wilde, who provided us with the first hands-on experience in cyanobacterial lab procedures when we were new to this field and also for contributing the Northern Blotting for this work. I would also like to thank Prof. Lorenz Adrian for contributing the shotgun proteomics analysis.

Special thanks go to our lab manager Jochen and our technicians, Kristin, Sebastian, and Ron, who handled the logistics, organized the lab infrastructure, and thereby ensured a pleasant working atmosphere. Thank you, Kristin and Sebastian, for your help with my experiments.

I would like to thank my students Stephan Altmann and Lisa Schmidt who contributed to this work with their experiments.

Special thanks also go to all my colleagues in the department of Solar Materials as well as in the former BT group. Thank you for all the discussions and for creating a pleasant working atmosphere. To all my colleagues from the biofilm group, thank you for all our entertaining cooking/discussion events (especially at Rohan's home).

I would like to thank Manfred, Mattijs, and Christian, who supervised my student works, guided me through my first steps in practical lab work and thereby willingly shared their hard-earned lab skills.

Special thanks also to Marcel. Although the principle “a problem shared is a problem halved” did not always work out, we somehow managed to “survive”. Also, thanks to Kristin for always making time for a talk and to eat quite a lot of sushi. Thank you, Bruno, for willingly sharing your expertise, wine, grappa, and BBQ.

Finally, I would like to express my deepest gratitude to my family, to my parents, my sister and my wife, Laura. Without your encouragement, support, and patience during my studies this would not have been possible. Laura, thank you so much for your kind understanding and your support. Thank you for making the distance between Leverkusen and Leipzig seem so small.

Table of contents

Zusammenfassung

Der Einsatz von photoautotrophen Mikroorganismen als Chassis für die Ganzzellbiokatalyse erlaubt die biotechnologische Produktion von Basischemikalien und Biokraftstoffen auf Basis von CO_2. Statt organische Kohlenstoffverbindungen zu nutzen, (Re-)Aktivieren diese mikrobiellen Zellfabriken CO_2 mit Hilfe von Sonnenlicht. Trotz einer Großzahl an entwickelten Biokatalysatoren scheitert die großtechnische Umsetzung solcher Prozesse an den bislang begrenzten Produktionsraten und Titern. Diese erlauben zum jetzigen Zeitpunkt keine wirtschaftlich sinnvolle Anwendung. Um das Potential dieser Ganzzellbiokatalysatoren auszuschöpfen sind weitere Fortschritte im Bereich der Biokatalysator- und Prozessentwicklung notwendig.

Die vorliegende Arbeit beschäftigte sich mit dem Design, der Konstruktion und Charakterisierung eines photoautotrophen Ganzzellbiokatalysators zur Produktion von 1,2-Propandiol (Propylenglykol). Besonderes Augenmerk wurde dabei auf den Einfluss von Speicherstoffen auf die Aktivität des synthetischen Stoffwechselweges gelegt. Um die Propandiolproduktion zu ermöglichen wurde ein synthetischer Stoffwechselweg bestehend aus einer Methylglyoxalsynthase, einer Aldehydreduktase und einer Alkoholdehydrogenase in *Synechocystis* sp. PCC 6803 eingebracht. Die daraus entstehenden Enzymaktivitäten ermöglichen die Umsetzung von Dihydroxyacetonphosphat zu Methylglyoxal, welches weiter zu Acetol und schließlich zu 1,2-Propandiol reduziert wird.

Unter optimierten Kultivierungsbedingungen konnten mit dem so erzeugten Ganzzellbiokatalysator bis zu 1 g L^{-1} (13 mM) 1,2-Propandiol hergestellt werden. Dabei handelt es sich um die bislang höchste publizierte 1,2-Propandiol Konzentration in einem photoautotrophen Organismus. Es konnte eine maximale Produktionsrate von bis zu 2.8 mM d^{-1} erreicht werden, was einer spezifischen Aktivität von ca. 55 µmol h^{-1} g_{CDW}^{-1} entspricht. Hierbei beschränkte sich die Produktion von 1,2-Propandiol auf die späte Wachstums- und stationäre Phase.

Die durchgeführten Experimente zeigten eine deutliche Abhängigkeit der 1,2-Propandiolproduktion vom Abbau des intrazellulären Speicherstoffs Glykogen. Sobald das vorher angesammelte Glykogen aufgebraucht war, stoppte auch die 1,2-Propandiolproduktion. Eine verringerte Glykogensynthese hatte signifikant verringerte 1,2-Propandioltiter zur Folge. Experimente mit ^{13}C markiertem CO_2 identifizierten Glykogen als Quelle für 25% des im Produkt enthaltenen Kohlenstoffs, während die restlichen 75% direkt durch den Calvin Zyklus bereitgestellt wurden. Zusätzliche Experimente ohne Lichtquelle zeigten klar das die Produktion von 1,2-Propandiol von der Verfügbarkeit von Lichtenergie und einen stattfindenden Glykogenabbau abhängt.

Die eingesetzte Methylglyoxalsynthase ist Startpunkt des Methylglyoxal Stoffwechselweges aus *E. coli*, der unter Phosphatmangel und einem Überschuss an GAP/DHAP aktiviert wird. Sequenzübereinstimmungen zwischen den Aminosäuresequenzen implizieren, dass der Methylglyoxalstoffwechselweg in *Synechocystis* sp. PCC 6803 vorhanden ist. Die Ergebnisse der durchgeführten Experimente deuten darauf hin, dass die Regulation des Methylglyoxalstoffwechselweges über die Methylglyoxalsynthase die Produktion von 1,2-Propandiol auf die stationäre Phase beschränkt. Diese Auswirkungen zeigen sich in allen rekombinanten Stämmen die via Methylglyoxalsynthase auf DHAP zugreifen. Damit ist die Methylglyoxalsynthase ein logischer Ansatzpunkt für die weitere Stammoptimierung.

Bei der Maßstabsvergrößerung von Schüttelkolbenkulturen in den 2-3L Bioreaktormaßstab reduzierte sich die produzierte 1,2-Propandiolmenge um ca. 50%. Zusätzliche Messungen der Kohlenstoffdioxidaufnahmerate des Bioreaktors ergaben eine netto CO_2 Freisetzung während der 1,2-Propandiolproduktion, die einherging mit einer netto Sauerstoffaufnahme. Dies deutet auf eine reduzierte Aktivität des Calvin Zyklus hin und erklärt die verringerte Produktkonzentration im Vergleich zu den vorherigen Experimenten.

Als Alternative zur planktonischen Kultivierung wurde die Biofilmbildung von *Synechocystis* sp. PCC 6803 untersucht. Es gelang *Synechocystis* Biofilme in Glaskapillaren zu kultivieren. Durch die Einführung zusätzlicher Scherkräfte in Form von Gassegmenten gelang es das Biomassewachstum zu begrenzen. Hierdurch konnte sich ein stabiler Biofilm mit einer Schichtdicke von 70–120 µm entwickeln. Ab diesem Zeitpunkt konnte kein weiteres Biofilmwachstum beobachtet werden, es kam auch nicht zu einer Ablösung von Biomasse. Die Weiterentwicklung dieses Reaktorkonzepts könnte in Zukunft die kontinuierliche Produktion von Wertprodukten aus CO_2 und Sonnenlicht ermöglichen.

Summary

The application of photoautotrophic microorganisms in biotechnology enables the development of next-generation microbial cell factories, which utilize sunlight to (re-)activate carbon dioxide. This enables the cells to provide carbon skeletons for the production of chemical feedstock and biofuels without the need for an organic carbon and energy source. However, up to now, the production rates and product titers achieved with these cell factories are low and far away from an economically feasible process. Further progress has to be made in biocatalyst and process engineering to increase the understanding and fully exploit the capacities of these biocatalysts.

This work focused on the development of a photoautotrophic whole-cell biocatalyst for the production of 1,2-propanediol (propylene glycol). Particular focus was placed on the interconnection between the accumulation of internal storage compounds and the influence on the production capacity of the synthetic pathway. A synthetic pathway comprising a methylglyoxal synthase, an aldehyde reductase, and an alcohol dehydrogenase was inserted into *Synechocystis* sp. PCC 6803 to convert dihydroxyacetone phosphate to methylglyoxal, which is subsequently reduced to acetol and then to 1,2-propanediol.

The recombinant strain successfully produced 1,2-propanediol at an approximate rate of 2.8 mM d^{-1} (55 µmol h^{-1} g_{CDW}^{-1}). Surprisingly, maximal productivity was observed in the stationary phase. Optimization of cultivation conditions allowed final product titers of almost 1 g L^{-1} (13 mM), which are the highest values published so far for the photoautotrophic production of this compound.

The production of 1,2-propanediol was coupled to the turn-over of intracellular glycogen. Upon depletion of the glycogen pool, product formation stopped. Reducing the carbon flux to glycogen significantly decreased final product titers. Experiments utilizing ^{13}C-labeled carbon dioxide revealed carbon fluxes and partitioning between biomass, storage compounds, and product. About one-quarter of the carbon incorporated into 1,2-propanediol originated from glycogen, while the rest was derived directly from CO_2 fixed in the Calvin cycle. Furthermore, experiments conducted in darkness showed that 1,2-propanediol synthesis was depending on the availability of photosynthetic active radiation and glycogen catabolism.

The applied methylglyoxal synthase is part of the methylglyoxal bypass of *E.coli*, which is activated under phosphate starvation and excess of GAP/DHAP. Homology comparison of the genomic sequence to genes encoding for the methylglyoxal bypass in *E.coli* suggested the exist-

ence of such a pathway also in *Synechocystis* sp. PCC 6803. There are indications that the regulation of the methylglyoxal bypass via methylglyoxal synthase interferes with the synthetic pathway leading to 1,2-propanediol in *Synechocystis* sp. PCC 6803. These findings are essential for all heterologous pathways coupled to the Calvin cycle-intermediate dihydroxyacetone phosphate via a methylglyoxal synthase. The methylglyoxal synthase was identified as a future engineering target for rational strain optimization.

The transfer of the process from cultivation in shaking flask to the 2-3 L benchtop bioreactor scale led to a reduced process performance with only half of the titers observed previously in shaking flasks. Additional measurement of carbon uptake rates indicated a different picture compared to the experiments in shaking flasks concerning the carbon fluxes. Here, no Calvin cycle activity accompanying 1,2-propanediol production could be detected. Instead, only glycogen catabolism with CO_2 evolution and oxygen consumption was observed.

Additionally to the conventional planktonic cultivation, also the cultivation of *Synechocystis* sp. PCC 6803 as a biofilm was investigated. *Synechocystis* sp. PCC 6803 could be grown in a biofilm covering the surface of glass capillaries. The additional hydrodynamic forces generated by a segmented flow prevented excessive biomass formation and clogging. The biofilm developed up to a thickness of 70–120 µm. The biofilm stopped growing at this thickness and stayed constant without any detachment events occurring afterwards. This biofilm reaction setup may enable continuous light-driven synthesis of value-added compounds in the future.

1 Introduction

1.1 Industrial biotechnology for a new bioeconomy

With the beginning of the 21st century, society faces the challenge to adapt to the limited availability of fossil carbon-based feedstocks and their negative impact on the global environment caused by the released carbon dioxide. In the context of an ever-growing global population, a transition from a fossil fuel-based economy to a sustainable and climate-friendly *bio-economy* is becoming inevitable for the wellbeing of future generations.

The European Commission defined the term bioeconomy as *"the production of renewable biological resources and the conversion of these resources and waste streams into value-added products, such as food, feed, bio-based products and bioenergy"* (European Commission, 2012). This new economy includes the sectors of agriculture, forestry, fisheries, food and pulp, and paper production, as well as the chemical, biotechnological and energy industries. An essential part of a successful bioeconomy is the production of energy carriers and chemical feedstocks from renewable resources. The resulting reduced dependency on non-renewable resources confines the consequences of climate change and ensures the ongoing supply of chemicals and energy. Thereby major objectives of a bioeconomy can be fulfilled.

In contrast to a non-renewable resource, like fossil fuel, a *renewable resource* overcomes depletion by biological reproduction or other naturally occurring processes. It is thereby of utmost importance that depletion of the resource does not outcompete the timeframe of the reproduction. Therefore, the bio-based renewable production of carbon-based compounds requires the recirculation of carbon dioxide within a reasonable time frame. The assembly of CO_2 into biomass is part of the naturally occurring carbon cycle. Hereby, CO_2 is utilized as an abundant and renewable carbon source fueled by solar irradiation.

Regrowing biomass can be converted by physical, chemical, and biochemical means into energy carriers and building blocks for the chemical industry in a biorefinery (Suhag and Sharma, 2015). However, plants still need arable land and are slow growing in comparison to algae and cyanobacteria. Microorganisms have proven to be versatile, fast growing and robust chassis for biotechnology. Therefore, an even more direct way of CO_2 utilization is the direct microbial conversion of CO_2 into chemical feedstocks.

Industrial biotechnology, also known as white biotechnology refers to the application of enzymes or microorganisms for the production of industrially relevant chemical compounds. Since the beginning of the last century, white biotechnology applies microbial cell factories for the pro-

duction of fermentation products from carbohydrate-based carbon sources. Starting with the late 1990s, also cyanobacteria and algae were utilized for the direct production of biofuels and value-added chemicals. Thereby, value-added compounds are directly produced from CO_2, water, and sunlight by photosynthetic microbial cell factories (PMCFs, Figure 1-1).

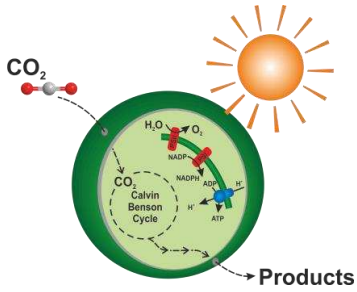

Figure 1-1: Photosynthetic microbial cell factory

The benefits of this approach are manifold. First, carbon dioxide is an abundant, non-fossil, and inexpensive feedstock. Second, the cultivation of algae and cyanobacteria does not depend on arable land and does therefore not compete with the food supply of the increasing worldwide population. And third, a new feedstock for the chemical industry is made available, which finally reduces the dependency on fossil fuels.

1.2 Photoautotrophic microorganisms for the production of chemicals

Photoautotrophic microorganisms performing oxygenic photosynthesis can be divided into prokaryotic cyanobacteria and eukaryotic algae. Oxygenic photosynthesis developed approximately 3 billion years ago in cyanobacteria and changed the way life developed on earth. Since then, light is utilized to extract electrons from water. Thereby biochemical energy and reduction potential are generated, and also, molecular oxygen is released as a side product. For several billion years, cyanobacteria accumulated oxygen in the atmosphere, which further enabled the evolution of aerobic microorganisms. It is widely believed that later on, endosymbiotic events led to the development of the modern eukaryotic cell. Thereby, endobiosis of a photoautotrophic cyanobacterium led to the development of eukaryotic algae and finally to the evolution of higher plants.

Consequently, either algae or cyanobacteria are applied as PMCFs. The ideal photoautotrophic microbial chassis would be easily accessible for genetic manipulation, would have a high carbon capture capability and would harvest light with high efficiency. Additionally, it would be resistant to contamination, have minimal nutritional needs, would growth in and utilize non-potable water sources, and have a low requirement for fertilizers (Hays and Ducat, 2015).

Whereas some green algae like *Chlamydomonas reinhardtii* are now accessible for genetic engineering, the ability in genetic modification of eukaryotic algae is still limited (Wijffels et al., 2013). In contrast, cyanobacteria are less complex and generally easier accessible for genetic modification. *Cyanobacteria* are a genetically diverse class of eubacteria inhabiting a wide range of different ecosystems (Beck et al., 2012). They can be isolated from fresh water, salt water, and terrestrial habitats distributed over all climatic zones (Mazard et al., 2016). Thus, cyanobacteria are promising chassis for industrial applications. Despite that, mainly two cyanobacterial strains are currently applied as PMCFs.

The first one, *Synechocystis* sp. PCC 6803 (hereafter referred to as *Synechocystis*) was isolated from a freshwater lake in California in 1968 (Stanier et al., 1971). Since then it was extensively studied as the first photoautotroph which genome was completely sequenced (Kaneko and Tabata, 1997). In addition, this strain is highly amenable to genetic modification and can grow photomixotrophically on glucose. These advantages made it the ideal choice for photosynthesis research. Consequently, *Synechocystis* is the best known and investigated cyanobacterial strain up to today. These are the characteristics which made it also an obvious choice for metabolic engineering approaches.

The other often used strain for metabolic engineering in cyanobacteria is the obligate photoautotrophic *Synechococcus elongatus*, which was first described by Nägeli in 1849 (Nägeli, 1849). The today applied strain *Synechococcus elongatus* PCC 7942 (hereafter referred to as *Synechococcus*) was isolated from freshwater in California in 1973 (Codd and Stewart, 1976). Recently, the whole genome sequence was made available by the Joint Genome Institute (JGI, USA).

In addition to these two strains, only a few others are applied because of their unique abilities. *Synechococcus* PCC 7002 is a fast-growing marine cyanobacterium that is of interest for an industrial application because it can grow at elevated salt concentrations and temperatures (Ruffing et al., 2016). *Thermosynechococcus elongatus* is of interest because of its ability to grow at elevated temperatures and *Anabaena*/ *Nostoc* sp. PCC 7120 strains were used if nitrogen fixation was involved, especially for the production of hydrogen by nitrogenases (Heidorn et al., 2011). Up to now, strains were not selected for a specific purpose, and there might still be a vast potential for improvement.

1.3 Bioprocess development utilizing PMCFs

For the successful implementation of PMCFs in industrial biotechnology, the integrated development of the different levels of bioprocess engineering is crucial. Figure 1-2 shows an overview of these development steps. The following chapters will focus on the most critical aspects of cyanobacterial bioprocess engineering.

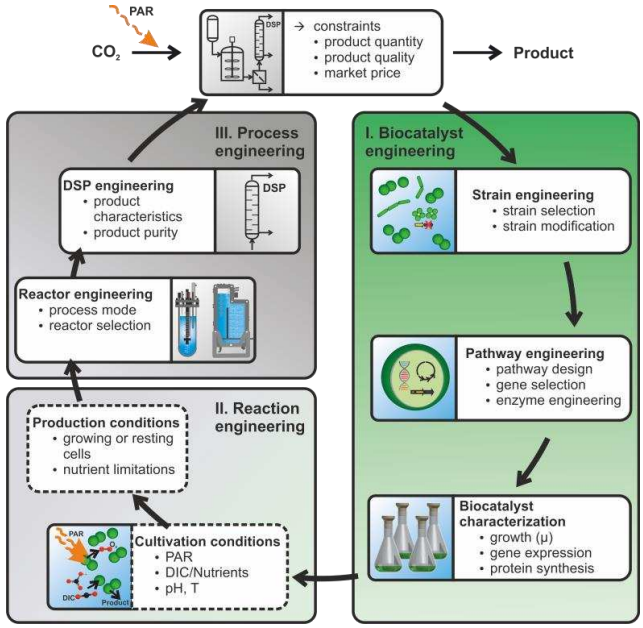

Figure 1-2: Bioprocess development for photofermentation

Illustration showing the different development stages from biocatalyst engineering via reaction engineering to process engineering that have to be addressed in the development of a biotechnological process applying a photoautotrophic biocatalyst.

1.3.1 Pathway engineering principles

The foundation for successful metabolic engineering is the availability of well-established molecular biological methods. Molecular biological bricks for *Synechocystis* and *Synechococcus* are available, but not to the extent as they are for other industrial relevant strains like *E.coli*. Therefore, further progress in the development of synthetic parts that allow enhanced strain and metabolic engineering in cyanobacteria is needed. Nevertheless, during the last decade, synthetic pathways have been engineered in cyanobacteria, and numerous studies have demonstrated the potential of cyanobacteria as a biotechnological platform. Proof of concept for the production of

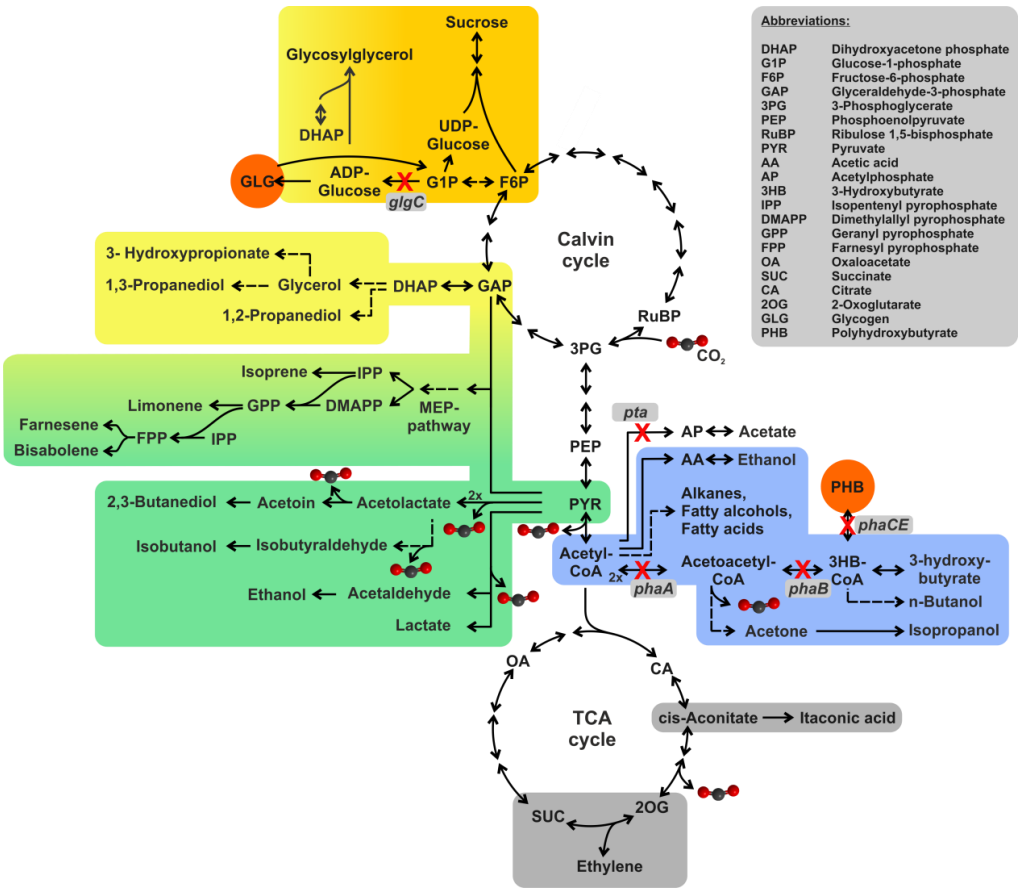

Figure 1-3: Established synthetic pathways in cyanobacteria

Overview showing the simplified core carbon metabolism of cyanobacteria, previously constructed synthetic pathways, and genes and reactions that are commonly targeted to disable competing pathways. Matching colors are indicating pathways starting from the same intermediate within the central carbon metabolism (blue – acetyl-CoA, green – pyruvate, yellow – DHAP/GAP, orange – F6P, grey – TCA cycle intermediate). Additionally, the two primary storage compounds accumulating in cyanobacteria, glycogen (GLG) and polyhydroxybutyrate (PHB) are marked in orange (see also Table 1-1 for details and sources).

ethanol, isopropanol, 1,2-propanediol, 1,3-propanediol, n-butanol, isobutanol, 2,3-butanediol, glycerol, lactic acid, isoprene, acetone, alkanes, ethylene, and also some fine chemicals have been shown. During the last years, the metabolic engineering work in cyanobacteria has been extensively reviewed (Angermayr et al., 2015; Oliver and Atsumi, 2014; Savakis and Hellingwerf, 2015, and numerous others). Table 1-1 (page 10ff.) shows a summary of the current state-of-the-art processes, comparing the industrially relevant process parameters such as light regime and DIC supply and the resulting titers and rates on a C-mol basis. Moreover, metabolic engi-

neering parameters such as used precursors, applied promotors and heterologous as well as deleted genes are listed.

Figure 1-3 shows the integration of the products listed in Table 1-1 into the cyanobacterial metabolism. Matching background colors indicate pathways starting from the same intermediate within the central carbon metabolism. The two primary storage compounds accumulating in cyanobacteria, glycogen (GLG) and polyhydroxybutyrate (PHB) are highlighted in orange. Also, possible targets for the deletion of pathways, which compete for carbon, are highlighted.

The pathways are divided into five groups based on the starting intermediate (hexoses, GAP/DHAP, pyruvate, acetyl-CoA, and TCA cycle intermediates). A majority of the synthetic pathways withdraws either pyruvate or acetyl-CoA from the central carbon metabolism. Also, the most successful metabolic engineering approaches for the production of ethanol (Gao et al., 2012; Namakoshi et al., 2016) and 2,3-butanediol (Oliver et al., 2013) are connected to these two precursors. Another significant junction is represented by glyceraldehyde-3-phosphate (GAP) and dihydroxyacetone phosphate (DHAP). Those precursors are the closest one to the CO_2 fixation. Additionally, hexose phosphates are utilized directly from the Calvin-Benson-Bassham cycle (hereafter Calvin cycle). In contrast, only two of the listed products were produced directly from tricarboxylic acid (TCA-) cycle intermediates (ethylene and itaconic acid shown in gray). The TCA cycle is seldomly used for metabolic engineering because it is less active in cyanobacteria as in heterotrophic organisms. Moreover, it was only recently described (Steinhauser et al., 2012). The storage compounds are competing for carbon and therefore represent a frequent target for gene deletions.

Reviewing the product titers, yields, and production rates in Table 1-1 allow conclusions concerning *pathway engineering principles* in cyanobacteria (Figure 1-4). Several factors will influence the production rate of a synthetic pathway, including efficient carbon fixation, an abundant metabolite pool, usage of abundant cofactors (e.g., NADPH), and low carbon loss within the pathway. Also, a pathway stoichiometry allowing a linear electron transport and irreversible reaction steps or steps with a high driving force can be beneficial (Angermayr et al., 2015; Oliver and Atsumi, 2014) (Figure 1-4). Pathways, where the cofactor dependency could be changed from NADH dependent to NADPH dependent reductases, showed improved performance (Gao et al., 2012; Li and Liao, 2013; Oliver et al., 2013). In cases where this was not possible, the introduction of a transhydrogenase enabled higher production rates (Angermayr et al., 2012; Niederholtmeyer et al., 2010; Varman et al., 2013b). Since the carbon spreads over the metabo-

lism, production pathways originated directly at the Calvin cycle, before further branching points in the carbon flux are reached, are expected to reach higher production rates and titer.

Figure 1-4: Pathway design principles

Illustration covering the 10 basic design principles that can be derived from the processes developed with cyanobacteria so far (listed in Table 1-1).

(based on Oliver and Atsumi, 2014)

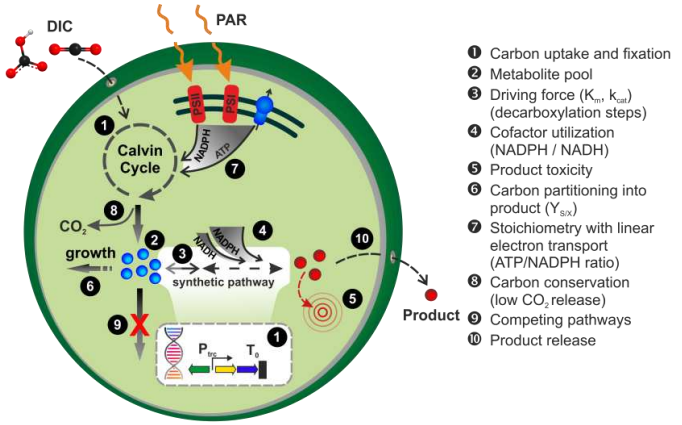

Several strategies were applied to increase carbon flux towards heterologous products. The most prominent strain engineering approaches are the knockout of the glycogen synthesis by replacement of the *glgC* gene and of the polyhydroxybutyrate (PHB) synthesis by replacement of either one of the *phaA, phaB, phaCE* genes (Anfelt et al., 2015; Namakoshi et al., 2016; Wang et al., 2013; Van der Woude et al., 2014 and many more). Additionally, if the product is derived from acetyl-CoA the *pta* gene was targeted, which is partly responsible for the conversion of acetyl-CoA to acetate (Carpine et al., 2017; Zhou et al., 2012; Zhou et al., 2014). Knockout of the glycogen synthesis increased the production of organic acids and compounds derived from pyruvate. The deletion of the PHB pathway had only a minor effect on the production of heterologous compounds. Additionally, dark anoxic conditions were applied to increase the yield of common fermentation products. With this strategy, several organic acids including succinate and acetate could be produced. This fermentation strategy is directly coupled to glycogen. Without photosynthetic activity, carbon and energy are delivered by storage compounds (Hasunuma et al., 2016).

To conclude, although production rates and titers are still limiting the industrial application, a broad data basis was obtained during the last decade.

1,2-propanediol. One pathway fulfilling the derived design principles is the synthetic pathway towards 1,2-propanediol. 1,2-propanediol, more commonly known as propylene glycol, is a commodity chemical. Industrial grade 1,2-propanediol is used in unsaturated polyester resins,

coolants, and anti-freeze agents, whereas high-grade 1,2-propanediol is used as a humectant, solvent, and preservative in the food, pharma, and cosmetics industry.

1,2-propanediol is currently produced from petroleum-based feedstock. 2.18 million tons are produced per year. The expected market growth rate until 2020 is about 4.5% each year. The market value is in between 790-830 € t^{-1} on the European market (Bridgwater et al., 2010). In context with the development of more sustainable and greener processes to reduce the dependency on fossil fuels, this chemical is highly attractive. The negative environmental impact of the conventional 1,2-propanediol production in combination with the finite nature and instability of fossil carbon supply is anticipated to drive the demand for bio-based 1,2-propanediol production on a global scale (Saxena et al., 2010). New 1,2-propanediol production plants based on glycerol as renewable feedstock were constructed within the last years. Cargill in cooperation with Ashland Inc. operated a 1,2-propanediol process based on glycerol obtained from the biodiesel industry with a capacity of 65 kt per year. Additionally, Cargill presented processes for the production of 1,2-propanediol from carbohydrates with heterotrophic microorganisms. Despite the discussed advantages of a microbiological production of commodity chemicals, the economic feasibility of such processes remains highly questionable. Disadvantages of such processes are mainly the high costs of the raw materials, low reaction rates and low product concentrations (Saxena et al., 2010).

Microbiological production involving heterotrophic strains depending on glucose or glycerol as a renewable resource competes with the food industry and arable land. In contrast, the production of bulk chemicals directly from carbon dioxide with photoautotrophic microorganisms powered by sunlight would be independent of valuable resources and would reduce greenhouse gas emissions. A pathway allowing photoautotrophic production of 1,2-propanediol from DHAP was already successfully introduced into *Synechococcus* by Li and Liao (Li and Liao, 2013).

Advantages of the production of 1,2-propanediol in cyanobacteria are the usage of DHAP as precursor and NADPH as the only necessary cofactor. DHAP is withdrawn directly from the Calvin cycle, only three steps apart from the CO_2 fixation. NADPH is the most abundant redox-cofactor in cyanobacteria and therefore highly available. Additionally, the conversion of DHAP to methylglyoxal is irreversible. The results of Li and Liao indicated that 1,2-propanediol could be produced during the stationary phase.

Table 1-1: Process parameters of cyanobacterial production processes

Selected photoautotrophic fermentations conducted in different cyanobacterial host strains. Fatty acids, fatty alcohols, alkenes, and processes with insufficient information, as well as hydrogen production were excluded.

Product	Titer [mMC]	Rate [mM_C day^{-1}]	Precursor	Promotor	heterologous genes	gene deletions	DIC supply CO_2 in air [%]	$NaHCO_3$ [mM]	Light regime PAR [µmol m^{-2} s^{-1}]	(light source, regime)	Reference
Synechocystis sp. PCC 6803											
2,3-butanediol	26	1	Pyruvate	P_{trc}	*als, aldc, butA*	-	ambient	-	30-40	(cool white light, constant)	(Savakis et al., 2013)
3-Hydroxybutyrate	16	1	Acetyl-CoA	P_{tac}	*tesB, phaA, phaB*	*phaC, phaE*	ambient	-	120	(n/a, constant)	(Wang et al., 2013)
Acetone	2	0.5	Acetyl-CoA	P_{cpc}	*adc, ctfAB*	*phaC, phaE, pta*	ambient	-	100	(n/a, constant)	(Zhou et al., 2012)
Ethanol	26	2	Pyruvate	n/a	*zwf, pdc, yqhD*	-	ambient	-	50	(n/a, constant)	(Choi and Park, 2015)
Ethanol	24	15	Pyruvate	P_{psbA2}	*pdc, adhII*	-	pH controlled	-	1000	(light bulbs)	(Dexter and Fu, 2009)
Ethanol	239	9	Pyruvate	P_{rbc}	*pdc, adhII*	*phaA, phaB*	5	-	100	(white light, constant)	(Gao et al., 2012)
Ethanol	33	5	Pyruvate	P_{nrsB}, P_{psbA2}	*fbaA, adh, pdc*	-	ambient	50	65	(n/a, constant)	(Liang et al., 2018)
Ethanol	100	15	Pyruvate	P_{rbcL}	*pdc, adhII*	-	5	-	100	(white light, constant)	(Luan et al., 2015)
Ethanol	129	87	Pyruvate	P_{nblA}	*pdc, adh*	*glgC, phaC, phaE*	ambient	100	80	(n/a, constant)	(Namakoshi et al., 2016)
Ethylene	-	0.4	2OG	P_{trc}	*efe*	-	1	-	100	(n/a, constant)	(Guerrero et al., 2012)
Ethylene	-	12	2OG	P_{psbA}	*2x efe*	-	5	20	50	(white fluorescent light, constant)	(Ungerer et al., 2012)
Glucosylglycerol	6	1	DHAP, G6P	-	-	*ggtc, ggtd, ggpr*	5	-	100	(n/a, constant)	(Tan et al., 2015)
Glycerol	42	5	DHAP	P_{trc}	*gpp*	-	ambient	-	30-40	(cool white light, constant)	(Savakis et al., 2015)
Isobutanol	0.2	0.02	Pyruvate	P_{trc}	*kivd*	-	ambient	50	50	(n/a, constant)	(Miao et al., 2017)
Isobutanol	16	-	Pyruvate	P_{tac}	*kivd, adhA*	-	ambient	50	50	(n/a, constant)	(Varman et al., 2013a)
Isoprene	0.03	0.003	IPP, DMAPP	P_{psbA2}	*IspS*	-	100	-	150	(n/a, constant)	(Bentley and Melis, 2012)
Isoprene	0.02	0.006	IPP, DMAPP	P_{psbA2}	*IspS, hmgR, hmgS, atoB, fni, mk, pmd, pmk*	-	100	-	150	(n/a, constant)	(Bentley et al., 2014)

Product	Titer [mMC]	Rate [mM_C day^{-1}]	Precursor	Promotor	heterologous genes	gene deletions	DIC supply CO_2 in air [%]	$NaHCO_3$ [mM]	Light regime PAR [µmol m^{-2} s^{-1}]	(light source, regime)	Reference
Synechocystis sp. PCC6803											
Isoprene	-	0.006	IPP, DMAPP	P_{psbA2}	*IspS*	-	ambient	-	40	(n/a, constant)	(Lindberg et al., 2010)
Itaconic acid	0.6	>0.1	cis-Aconitate	P_{tac}	*cad*	-	ambient	50	30	(LED, constant)	(Chin et al., 2015)
Lactate	10	1	Pyruvate	P_{trc}	*ldh, sth*	-	ambient	-	30	(cool white light, constant)	(Angermayr et al., 2012)
Lactate	62	3	Pyruvate	P_{trc}	*ldh*	-	ambient	-	30-40	(cool white light, constant)	(Angermayr and Hellingwerf, 2013)
Lactate	27	3	Pyruvate	P_{trc2}	*pk, ldh*	-	ambient	-	35	(white light, constant)	(Angermayr et al., 2014)
Lactate	0.5	0.1	Pyruvate	P_{psbA2}	*ldh, lldp*	-	ambient	-	50	(n/a, constant)	(Joseph et al., 2013)
Lactate	6	5	Pyruvate	P_{trc}	*ldh*	*glgC*	ambient	-	35	(n/a, constant)	(Van der Woude et al., 2014)
Lactate	38	3	Pyruvate	P_{trc}	*gldA*	-	ambient	-	100	(n/a, constant)	(Varman et al., 2013b)
Lactate	35	12	Pyruvate	P_{cpc560}	*ldh*	*phaC, phaE, pta*	ambient	-	100	(partly dark, anaerobic)	(Zhou et al., 2014)
Limonene	0.07	0.004	IPP, DMAPP	P_{trc}	*lms, dxs, crtE, ipi*	-	1	-	50	(white fluorescent light, constant)	(Kiyota et al., 2014)
n-Butanol	2	0.4	Acetyl-CoA	P_{psbA2}/ P_{trc}	*phaJ, ter, adhE2*	*phaC, phaE*	1	50	50	(n/a, constant)	(Anfelt et al., 2015a)
p-Coumaric acid	5	1	Tyrosine	P_{psbA2}	*sam8*	*yfiH*	ambient	-	50	(n/a, constant)	(Xue et al., 2014)
PHB	9	0.3	Acetyl-CoA	P_{trc}	*xfpk*	*pta, ach*	2	-	260	(white fluorescent light, diel light/dark cycle	(Carpine et al., 2017)
Succinate	4	1	2OG	-	-	-	ambient	100	n/a	(partly dark, anaerobic)	(Hasunuma et al., 2016)
Succinate	6	2	2OG	P_{trc}	*ppc*	-	ambient	100	n/a	(partly dark, anaerobic)	(Hasunuma et al., 2016)
Sucrose	11	7	F6P	P_{petE}	*sps, spp, ugp*	*ggpS*	5	-	100	(white light, constant)	(Du et al., 2013)

Product	Titer [mM C]	Rate [mM_C day^{-1}]	Precursor	Promotor	heterologous genes	gene deletions	DIC supply CO_2 in air [%]	$NaHCO_3$ [mM]	Light regime PAR [µmol m^{-2} s^{-1}]	(light source, regime)	Reference
***Synechococcus elongatus* PCC 7942**											
1,2-Propanediol	6	1	DHAP	P_{trc}	*mgsA, yqhD, adh*	-	ambient	50	100	(white fluorescent light, constant)	(Li and Liao, 2013)
1,3-Propanediol	11	2	DHAP	P_{lacO1}	*dhaB1 - 3, gdrA , grdB, yqhD, gpd1, hor2*	-	3	-	100	(white fluorescent light, constant)	(Hirokawa et al., 2016)
1,3-Propanediol	13	4	DHAP	P_{lacO1}	*dhaB1 - 3, gdrA , grdB, yqhD, gpd1, hor2*	*ndhF1*	3	-	100	(white fluorescent light, constant)	(Hirokawa et al., 2017)
2,3-Butanediol	133	17	Pyruvate	P_{trc}/P_{lacO1}	*alsS, alsD, ad, galP*	-	ambient	10	65	(white fluorescent light, constant)	(McEwen et al., 2016)
2,3-Butanediol	106	8	Pyruvate	P_{lacO1}	*alsS, alsD, adh*	-	ambient	50	55	(white fluorescent light, constant)	(Oliver et al., 2013)
2-Methylbutanol	8	1	Pyruvate, Acetyl-CoA	P_{trc}	*kivD, yqhD, cimA, leuB, leuC, leuD*	-	ambient	50	150	(n/a, constant)	(Shen and Liao, 2012)
3-Hydroxypropionate	22	3	Acetyl-CoA	P_{trc}	*mcr, msr*	-	ambient	50	50	(white fluorescent light, constant)	(Lan et al., 2015)
3-Hydroxypropionate	1	0.1	DHAP	P_{trc}	*gpp1, dhaB, puu*	-	5	-	100	(partly dark, anaerobic)	(Wang et al., 2015)
Dihydroxyacetone	3	0.3	DHAP	P_{trc}	*gpp1, dhaB*	-	ambient	-	100	(n/a, constant)	(Wang et al., 2015)
Ethanol	10	0.4	Pyruvate	P_{rbcLS}	*pdc, adh*	-	ambient	-	50	(white fluorescent light, constant)	(Deng and Coleman, 1999)
Ethanol	8	3	Acetyl-CoA	P_{trc}	*pduP, yqhD*	-	ambient	50	50	(white fluorescent light, constant)	(Lan et al., 2013)
Ethylene	-	0.004	SAM	P_{trc}	*ACS-Ctdoc, ACO-Acdoc, Cip2*	-	ambient	-	100	(n/a, constant)	(Jindou et al., 2014)
Ethylene	-	0.5	2OG	P_{psbA1}	*efe*	-	ambient	-	n/a	n/a	(Takahama et al., 2003)
Glycerol	38	3	DHAP	P_{lacO1}	*dhaB1 - 3, gdrA , grdB, yqhD, gpd1, hor2*	-	3	-	100	(white fluorescent light, constant)	(Hirokawa et al., 2016)
Glycerol	91	7	DHAP	P_{lacO1}	*dhaB1 - 3, gdrA , grdB, yqhD, gpd1, hor2*	*ndhF1*	3	-	100	(white fluorescent light, constant)	(Hirokawa et al., 2017)
Glycerol	56	6	DHAP	P_{trc}	*gpp1*	-	5	-	100	(n/a, constant)	(Wang et al., 2015)
Hexoses	2	0.6	F6P	P_{trc}	*glf, invA, galU*	-	ambient	-	n/a	Dark/ light cycles	(Niederholtmeyer et al., 2010)
Isobutanol	24	4	Pyruvate	P_{trc}/P_{lacO1}	*alsS, ilvC, ilvD, kivd, yqhD*	-	ambient	50	n/a	n/a	(Atsumi et al., 2009)

Product	Titer [mMC]	Rate [mM_C day^{-1}]	Precursor	Promotor	heterologous genes	gene deletions	DIC supply CO_2 in air [%]	$NaHCO_3$ [mM]	Light regime PAR [µmol m^{-2} s^{-1}]	(light source, regime)	Reference
***Synechococcus elongatus* PCC 7942**											
Isobutanol	15	1	Pyruvate	P_{trc}	*kivD, yqhD*	-	ambient	50	150	(n/a, constant)	(Shen and Liao, 2012)
Isobutyraldehyde	61	8	Pyruvate	P_{tac}/P_{trc}/P_{lacO1}	*rbcL, rbcS, alsS, ilvC, ilvD*	-	ambient	50	n/a	n/a	(Atsumi et al., 2009)
Isopropanol	7	1	Acetyl-CoA	P_{lacO1}	*thl, atoAD, adc, sadh*	-	5	-	150	(partly dark, anaerobic)	(Hirokawa et al., 2015)
Isopropanol	1	0.3	Acetyl-CoA	P_{lacO1}	*thl, atoAD, adc, adh*	-	5	-	50	(partly dark, anaerobic)	(Kusakabe et al., 2013)
Lactate	44	7	Pyruvate	P_{trc}	*ldhDc, lldP*	-	5	-	100	(white fluorescent light, constant)	(Li et al., 2015)
Lactate	2	0.5	Pyruvate	P_{trc}	*ldhA, lldP*	-	ambient	-	n/a	Dark/ light cycles	(Niederholtmeyer et al., 2010)
n-Butanol	1	0.2	Acetyl-CoA	P_{lacO1}	*ter, crt, hbd*	-	5	50	150	(partly dark, anaerobic)	(Lan and Liao, 2011)
n-Butanol	2	0.1	Acetyl-CoA	P_{trc}/P_{lacO1}	*pduP, yqhD, ter, nphT7, crt , hbt*	-	ambient	50	100	(white fluorescent light, constant)	(Lan and Liao, 2012)
n-Butanol	22	3	Acetyl-CoA	P_{trc}/P_{lacO1}	*pduP, yqhD, ter, nphT7, crt , hbt*	-	ambient	50	50	(white fluorescent light, constant)	(Lan et al., 2013)
Sucrose	96	30	F6P	P_{trc}	*cscB*	*invA, glgC*	2	-	65	(white fluorescent light, constant)	(Ducat et al., 2012)
***Synechococcus* sp. PCC 7002**											
Bisabolene	0.04	0.01	FPP	P_{cpc}	*BiS*	-	1	-	250	(n/a, constant)	(Davies et al., 2014)
Limonene	0.3	0.1	GPP	P_{cpc}	*LS*	-	1	-	250	(n/a, constant)	(Davies et al., 2014)
Mannitol	36	5	F6P	P_{psbA}	*mtlD, mlp*	*glgA1, glgA2*	1	-	250	(white fluorescent light, constant)	(Jacobsen and Frigaard, 2014)
***Nostoc / Anabaena* sp. PCC 7120**											
Farnesene	0.02	0.002	FPP	P_{psbA1}	*FaS*	-	1	-	50	(n/a, constant)	(Halfmann et al., 2014)

1.3.2. Reaction engineering for PMCFs

The reaction engineering for photoautotrophic whole-cell biocatalysts is still at an early stage of development. The different processes apply a wide range of different cultivation and reaction conditions (see Table 1-1). Diverse sources for photosynthetically active radiation (PAR), a considerable range of applied light regimes ranging from 30 – 250 µmol m^{-2} s^{-1}, and different ways to supply dissolved inorganic carbon (DIC) during cultivation make it difficult to compare these studies on a process level. Furthermore, in some cases additional heterotrophic carbon sources were utilized (Choi and Park, 2015; McEwen et al., 2016; Varman et al., 2013a) or cells were cultivated under dark anoxic conditions during the production phase (Hasunuma et al., 2016; Hirokawa et al., 2015; Kusakabe et al., 2013; Lan and Liao, 2011; Wang et al., 2015; Zhou et al., 2014).

In general, photofermentations are different in comparison to heterotrophic fermentations regarding reaction engineering. Photoautotrophic microorganisms realize two fundamental processes: the conversion of light into biological energy and the application of this energy to activate carbon dioxide. Therefore, the most important parameters which have to be considered are the primary energy source light and the primary carbon source that is dissolved inorganic carbon.

Photosynthetically active radiation. The energy utilized by phototrophic growing organisms has to be provided by either natural sunlight or artificial light sources, like light-emitting diodes (LEDs) or fluorescent light bulbs. The irradiation spectrum provided by applied light sources is highly diverse. Not all wavelengths can be utilized for photosynthesis. Therefore, light composition plays an important role. Irradiation that can be absorbed by photopigments and is utilized by different phototrophic growing organisms is referred to as photosynthetically active radiation. That includes mainly the visible spectrum of light with wavelengths in between 400 to 700 nm. Wavelengths below 400 nm (ultraviolet light) are mostly harmful to living organisms due to their high energy content, whereas irradiation with longer wavelengths (infrared light) does not provide enough energy to enable photosynthesis. However, there are exceptions were near-infrared light is utilized to support life. Depending on their arsenal of photopigments microorganisms can utilize different parts of the PAR spectrum.

The host strains *Synechocystis* and *Synechococcus* have a phycobilisome consisting of an allophycocyanin core and phycocyanin rods. Together with chlorophyll A, this enables the cells to utilize

mainly blue and red light (Kopecna et al., 2012). However, not only the quality of the light but also the quantity plays an essential role in phototrophic growth. Figure 1-5 (A) shows a schematical representation of the relationship between incident light intensity and growth rate.

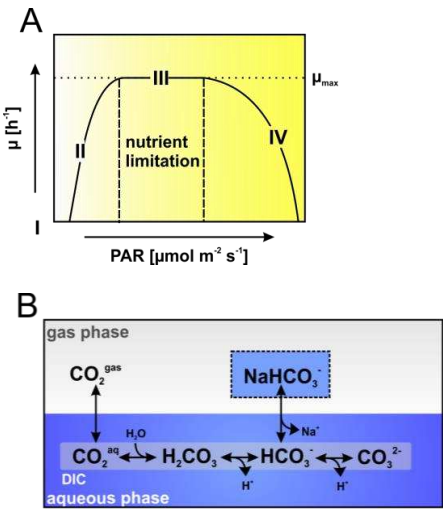

Figure 1-5: (A) Relationship between incident light intensity and growth

Schematic diagram illustrating the resulting growth rates of a photoautotrophic strain under different light intensities (PAR). The responding growth can be divided into 4 different regimes: (I) Insufficient light for growth (II) Light limited growth (III) Growth that is unlimited by light (IV) Photoinhibition.

(modified from Zevenboom et al., 1980)

(B) Carbonate equilibrium

Illustration of the carbonate equilibrium in water and different feeding strategies. DIC can either be supplied via the diffusion of CO_2 from the headspace of the culture, or it can be provided in the form of a bicarbonate solution (e.g., sodium bicarbonate).

Without sufficient incident light, growth is not possible (Figure 1-5 A, Regime I), even needs for maintenance cannot be covered, and cells will start to die when they incubate under extended periods of darkness. Upon a certain threshold, with increasing light intensity, the growth rate increases (Figure 1-5 A, Regime II) until additional light cannot be utilized anymore and the maximal growth rate is reached (Figure 1-5 A, Regime III). Below the curve representing the maximal possible growth rate, growth is limited by nutrient accessibility (Tilzer, 1987; Zevenboom et al., 1980). When the light intensity exceeds a certain limit, photoinhibition occurs and limits the growth rate (Figure 1-5 A, Regime IV).

Another challenge connected to the substrate light is the inhomogeneity within the culture. Self-shading of the cells leads to declining PAR with increasing distance from the light source and culture depth. With increasing cell concentrations, this effect becomes more pronounced. Light distribution within the culture is one of the major obstacles which have to be solved for a successful application of PMCFs in industrial biotechnology. Under realistic cultivation conditions with the application of sunlight as the energy source, the cells face a diel light regime with a wide range of light intensities. The internal regulation of growth, carbon flow, and energy flow during changing light intensities is not yet understood. Therefore, also the influence on production processes cannot be predicted.

Dissolved inorganic carbon. The other essential resource needed for photoautotrophic growth is the carbon source CO_2. Carbon is taken up either as CO_2 or as bicarbonate (HCO_3^-) by the cells. The CO_2 is then activated and incorporated by the enzyme ribulose-1,5-bisphosphate carboxylase/oxygenase (RuBisCO). Consequently, dissolved inorganic carbon has to be provided in sufficient amounts to sustain growth and production. Two ways to provide DIC are commonly applied in this context: either CO_2 is supplied via the gas phase during cultivation, or sodium bicarbonate (Na_2HCO_3) is repeatedly fed to the medium. Independently of the used supply strategy, carbon dioxide is part of the carbonate equilibrium. Dissolved CO_2 is in equilibrium with carbonic acid, which dissolves into bicarbonate and further into carbonate depending on the pH value of the solution (Figure 1-5, B). If CO_2 is delivered via the gas phase, the Henry coefficient for CO_2 determines the equilibrium concentration of CO_2 in the aqueous phase. All components of the carbonate equilibrium inside the aqueous phase build the pool of dissolved inorganic carbon.

To conclude, a wide range of light and DIC supply strategies exist. However, up to now the influence on growth and especially on the production of value-added products is not well understood and limits the photobiocatalyst performance and its industrial applicability.

1.3.3. Process engineering

The same parameters that are most important for the reaction engineering (PAR, DIC) do also significantly influence the reactor development. Consequently, well established reactor concepts for heterotrophic microorganisms do not meet the demands of phototrophic cultivation, especially concerning the distribution of light. Therefore, new photobioreactor concepts have been developed. A large number of these cultivation systems are currently applied in lab-scale, whereof only a few can be up-scaled to an industrial scale.

Figure 1-6 and Table 1-2 give an overview showing current industrially applied reactor concepts for algae cultivation. Large-scale photobioreactors can be divided into open and closed systems (Carvalho et al., 2006). *Open bioreactor* systems consist mainly of different types of circular ponds (CP) and raceway ponds (RP). Circular ponds are simple open vessels mixed by a rotating arm, whereas raceway ponds are closed-looped flow channels, with a paddle wheel providing the flow. Open ponds are applied in wastewater treatment since the 1950s and are still the most

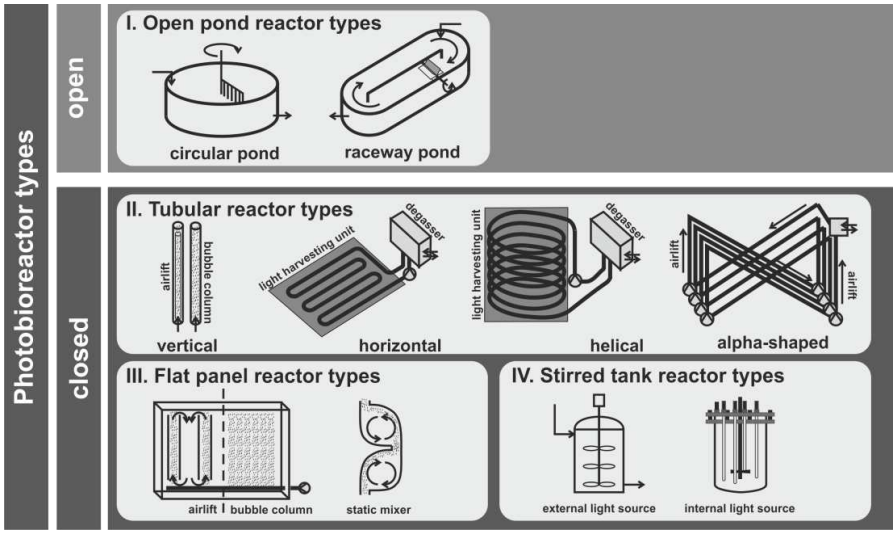

Figure 1-6: Commercially available photobioreactors

Schematic representation of commercially available photobioreactors divided into open and closed systems. Whereas open systems are mainly represented by different types of ponds (I), closed systems can be further distinguished into tubular reactor types (II), flat panel reactor types (III), and stirred tank reactor types (IV).

often applied concept in the industry. They are easy to operate and very cost efficient. For algal cultivation and

maximized growth, the raceway pond can be equipped with CO_2 spargers to overcome mass transport limitations and to enable pH control. The significant drawbacks include chemical and biological contaminations, grazers, the influence of weather, and the incompatibility with regulations concerning the release of genetically modified organisms (GMOs). Also, due to technical limitations, these systems have to have at least 0.2 m culture depth, which limits light harvesting efficiency. With these systems, biomass for future processing in a biorefinery may be grown. However, they are not suited for the application of PMCFs and the production of biofuels and chemical feedstock under controlled conditions.

Closed systems can be divided into tubular (TR), flat panel (FPR), and stirred tank-type reactor concepts (STR). With these systems, it becomes possible to grow monocultures. In general, due to the improved light availability, 2-3x the production yield of open ponds concerning biomass can be achieved. Out of these, *tubular reactor concept*s represent the most diverse group of photobioreactors. They include vertical (VTR), horizontal (HTR), and helical tubular photobioreactors (HeTR). VTRs are vertical columns constructed either as simple bubble columns or an airlift reactor. This type of reactor can be easily scaled up by numbering up. Light harvesting and

gas exchange are combined in one unit. In contrast, HTRs consist out of two units, a horizontal light-harvesting unit with parallel or looped tubing and a degasser unit to provide carbon dioxide and remove accumulated oxygen. Mostly, the degasser unit is constructed in an airlift principle to generate the necessary flow. The horizontal construction ensures the highest available light intensity for the light-harvesting part. Further development of this concept is represented by the HeTR, where the light harvesting unit is constructed in a 3-dimensional helical pattern. In comparison to the HTR, it enables a higher reactor-volume-to-footprint ratio and increases the overall light utilization. A particular type of tubular concept is the α-shaped tubular photobioreactor (αTR), which combines the benefits of both vertical and horizontal TRs. The light harvesting part can be oriented for optimal light harvest and operates simultaneously as the downcomer of the airlift that provides gas exchange.

Table 1-2: Advantages and disadvantages of currently available photobioreactor concepts

Photobioreactor	Advantages	Disadvantages
circular and raceway ponds	• cost efficient • easy to operate	• inefficient light harvesting • limited mixing and gas exchange • contaminations • influence of temperature and precipitation
tubular reactors	• efficient light harvesting • efficient mixing • controlled conditions • cultivation of GMOs possible	• dimensions limited by gas exchange • accumulation of oxygen and depletion of CO_2
flatpanel reactors	• highest light harvesting efficiency • direct gas exchange • controlled conditions • cultivation of GMOs possible	• limited mixing • high investment costs
stirred tank reactors	• well-known and characterized • widely applied in industry • controlled conditions • cultivation of GMOs possible	• low light harvesting efficiency • very inhomogeneous light distribution • shear stress

A different concept for photobioreactors does not rely on the use of tubing-like structures. Instead, rectangular vessels generating large surface-to-volume ratios are utilized. This *flatpanel photobioreactors* (FPR) provide a high illuminated surface area, while simultaneously minimizing culture depth. The airlift principle provides carbon dioxide supply and mixing. Additionally, static

mixers can be applied. The highest cell densities for cyanobacterial cultivation were reported for these reactor systems (Gitelson et al., 1996; Hu et al., 1998).

Additionally, STR-like concepts were applied in some cases. Due to the low surface-to-volume ratio in this reactor system, light has to be supplied at different levels within the reactor vessel. Moreover, mixing is provided by mechanical stirring, which causes shear stress to the cells. All of these aspects make this concept the least suitable for a photobioreactor approach.

The different bioreactor types were closely evaluated concerning their technical limitations (Carvalho et al., 2006) and for biomass growth as feedstock for biorefineries (Narala et al., 2016), but not yet concerning the applicability for the direct production of biofuels and chemical feedstock.

Another important aspect of the development towards industrial production is the availability of the different reactor concepts not only in lab-scale but also in pilot-scale and process-scale. Pilot-scale photobioreactors of all four types, namely horizontal and stacked tubular photobioreactors, algal ponds, and flat panel reactors were installed and are operated at the AlgaePARC facility (AlgaePARC pilot facility, Wageningen, Netherlands). Leading suppliers of state of the art photobioreactor equipment include for example Algenol (Algenol Biotech, Fort Myers, Florida, US) or Subitec (Subitec GmbH, Stuttgart, Germany) for fully enclosed, flat panel type photobioreactors and Varicon Aqua Solutions (Varicon Aqua Solutions Ltd, Worcester, UK) for airlift, helical tubular, bubble column, and fence type photobioreactors. The scientific community is well aware of the necessity of further photobioreactor development. Consequently, much research is performed concerning the development of new photobioreactor systems (Carvalho et al., 2006; Kumar et al., 2011).

In conclusion, current photobioreactors were designed to optimize biomass formation from CO_2 and sunlight. However, the optimal conditions for growth are not necessarily the optimal conditions for productivity as well. Therefore, new reactor concepts have to be developed to optimize the formation of value-added products instead of focusing on biomass formation.

1.3.4. Biofilms for white biotechnology

A promising approach for the development of continuous processes with photoautotrophs is the retention of biomass by self-immobilization of the biocatalyst within a biofilm. Biofilms are cellular communities attached to surfaces and embedded in self-produced extracellular polymeric

substances (EPS). In the broadest sense, all kinds of microbial structures like cell aggregates (flocs), sedimented layers or tightly attached films can be defined as biofilms (Flemming and Wingender, 2010; Wingender et al., 1999). Biofilms are omnipresent in nature, where they are often found as multispecies microbial mats. In such structures, a complex system of interrelated dependencies of various organisms comprising phototrophic and heterotrophic strains exist. Biofilms are also very important in artificial medical or technical settings, although there they are mostly unwanted, as biofilms are very persistent and lead to biofouling or severe infections. However, these characteristics could be beneficial regarding process stability and a continuous process mode for biocatalysis and the production of value-added compounds with biologically challenging reactants as shown recently (Gross et al., 2013).

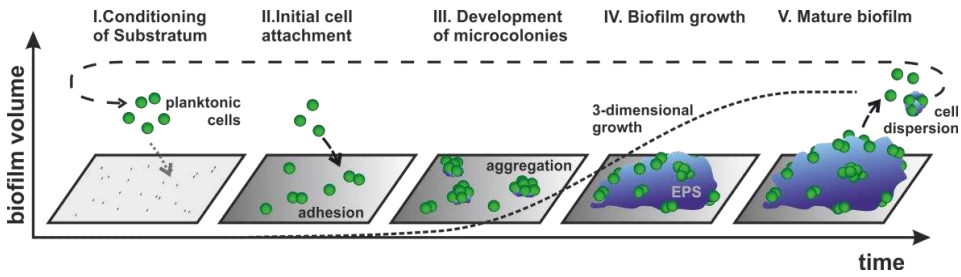

Figure 1-7: Biofilm development stages

Schematic drawing showing the development of a biofilm over time. The development of biofilms can be differentiated into five distinct growth phases. Phase 1: conditioning of substratum, phase 2: initial cell attachment, phase 3: growth of microcolonies, phase 4: 3-dimensional biofilm growth, phase 5: fully developed mature biofilm.

Figure 1-7 shows the different stages of biofilm development. Conditioning of the substratum is followed by initial cell attachment of planktonically free-floating cells. Afterwards, cell attachment becomes irreversible, and microcolonies embedded in EPS develop out of these cells. Those microcolonies grow into a multilayered biofilm. Finally, the biofilm reaches its maximal expansion. In this final stage, the amount of dispersed and re-growing cells within the mature biofilm are in balance, and a stable biofilm thickness is achieved (Halan et al., 2012; Monroe, 2007).

For the industrial application, the maximum persistence of the mature biofilm is essential for continuous production. Higher overall robustness, self-regeneration and immobilization with high biomass retention are the main characteristics for catalytically active biofilms (Halan et al., 2012; Rosche et al., 2009). While applications of heterotrophic biofilms are well described, ex-

amples using photoautotrophic organisms as biofilm catalysts are missing up to date, although numerous studies reported prove of concept for the synthesis of value-added compounds by suspended phototrophic organisms like cyanobacteria and microalgae.

Table 1-3: Advantages and disadvantages of photoautotrophic biofilms

Advantages	Disadvantages
• high biomass accumulation	• mass transport hindrance
• reduced growth-rates	• clogging
• self-immobilization	• up-scale limitations
• continuous operation	• limited experience
• robustness	• increased self-shading
• self-regeneration	

In ecology, natural phototrophic-heterotrophic multispecies biofilm communities play a significant role for ecosystem assessment and are frequently studied (Al-Najjar et al., 2012; Fenchel and Kühl, 2000; Kühl and Fenchel, 2000; Wolf et al., 2007; Zippel et al., 2007; Zippel and Neu, 2005), whereas studies of phototrophic biofilms for synthetic and technical applications are limited (Fresewinkel et al., 2014). Examples of phototrophic biofilms include microbial fuel cells (McCormick et al., 2011) and applications in wastewater treatment (Roeselers et al., 2008). While in wastewater treatment vast amounts of biomass are generated, microbial fuels cells represent a static non-flow system without hydrodynamic forces. Such systems are not suited for applications in whole cell biocatalysis due to mass transfer limitations and uncontrolled biomass growth (van Loosdrecht and Heijnen, 1993).

Key challenges when applying catalytic biofilms in continuous processes include the mass transfer of substrates through the three-dimensional structur of cells and EPS, the sufficient penetration of light, and excessive biomass formation resulting in clogging. One approach to circumvent these bottlenecks is the formation of a flat, compact film. This can be achieved by cultivating the particular microbes in capillary tubings under continuous flow applying hydrodynamic stress. Hydrodynamic stress can, for example, be applied by interfacial forces generated by two-phase segmented flow, consisting of an aqueous and a gaseous phase (Karande et al., 2014)(for more details, please refer to chapter 3.6).

The first biofilm reactor concepts were developed and applied for wastewater treatment (Qureshi et al., 2005). These reactor concepts could partly be transferred for the production of value-added chemicals in industrial biotechnology (Ercan et al., 2015).

Biofilm reactors can be divided into reactors with a moving biofilm (expanded bed) and with a stationary biofilm (fixed bed). Reactor systems with moving biofilms include stirred tank biofilm reactors (STBR), fluidized bed biofilm reactors (FBBR), and rotating disc biofilm reactors (RDBR).

Reactors with stationary biofilm layers include packed bed biofilm reactors (PBBR), trickling bed biofilm reactors (TBBR), and membrane biofilm reactors (MBR). None of these concepts can be easily adapted for phototrophic biofilms. Whereas the mass transfer of gaseous compounds was a design parameter during the development of these systems, the availability of sufficient PAR was not. So far, only a few initial concepts for biofilm reactors for phototrophic cultivation have been developed. The principle of the rotating disc biofilm reactor was transferred to a rotating bed biofilm reactor (Christenson and Sims, 2012). However, as with the photobioreactors for planktonic growth, this reactor is suitable for high biomass production and not optimized for the production of biofuels or chemical feedstock. Another new reactor concept, the emersed biofilm reactor, applies light-emitting glass rods as a substratum for biofilm growth (Kuhne et al., 2013). In this concept, nutrients and water are supplied with an aerosol stream passing the glass rods. This bioreactor concept does reduce medium consumption. However, it is not easily up-scaled into an industrial relevant size.

To conclude, the development of suitable cultivation concepts and the identification and characterization of monospecies biofilms will be essential for applications of phototrophic biofilms as catalysts in synthetic chemical industries.

1.4 Summary

In conclusions, this review shows that the production of a wide range of diverse products from alcohols to organic acids, as well as alkanes, and some fine chemicals can be accomplished in cyanobacteria, but also revealed the gap between these proof of principle studies and an industrial application. Still, certain limitations prevent the successful industrial scale application of this technology. Challenges include low activities, stabilities, and concentrations as well as carbon partitioning in favor of biomass and in the end therefore low economic feasibility. Except of ethanol production, which was commercialized by Algenol (Algenol Biotech, Fort Myers, Florida, US), none of these studies are close to or within the window of operation for an economically feasible industrial process. Even the economically viable industrial implementation of algae or cyanobacterial bioethanol production could not yet be realized following the decrease in oil pric-

es (e.g. algenol, photanol; Laurens, 2017). Consequently, there are no standard process development strategies available and only a limited number of reactor concepts exist.

The application of biofilms is a promising alternative to achieve economically feasible processes for the sustainable production of biofuels and chemical feedstock. The foundation to achieve this goal is an improved understanding of photoautotrophic metabolism. Therefore, the investigation of growth phases, nutrient and energy limitations, and the interconnections with the heterologous production of chemicals and fuels have to become one focus of attention, the uncoupling of growth and heterologous production another.

1.5 Scope of this thesis

As discussed above, process development with photosynthetic microbial cell factories is highly complex and not well understood. This study aimed to gain deep process understanding of bulk chemical production with cyanobacteria.

Therefore, a biocatalyst producing a model bulk chemical was designed to investigate cultivation and production conditions. Based on this, up-scaling into bioreactor scale and finally evaluation of continuous cultivation in biofilms was performed.

Based on known pathway design principles, 1,2-propanediol was chosen as the model product used in this study. Following the cycle of bioprocess engineering described before (Figure 1-2), this thesis focused on the process development from strain engineering to reactor engineering. After the selection of a suitable strain, the metabolic pathway was designed and integrated. The resulting biocatalyst was characterized regarding growth, recombinant gene expression, and protein synthesis. Reaction and cultivation conditions were investigated and optimized, enabling rational reactor development. Finally, the results of this research were evaluated regarding suitability and applicability for the industrial and sustainable production of bulk chemicals based on carbon dioxide.

2 Materials and Methods

2.1 Chemicals and reagents

Unless stated otherwise all chemicals used were obtained from AppliChem (Darmstadt, Germany), Sigma Aldrich (Steinheim, Germany), or Carl Roth (Karlsruhe, Germany) and were of the highest purity available. Custom synthesized oligonucleotides were purchased by Eurofins Genomics GmbH (Ebersberg, Germany). Restriction enzymes, ligases, exonucleases, dNTPs and phusion polymerase were provided by New England Biolabs (Ipswich, Massachusetts, USA) and Fermentas/Thermo Fisher Scientific (Waltham, MA, USA).

2.2 Cultivation of strains

All plasmids and bacterial strains used in this study are listed in Table 2-1 and Table 2-2. *Escherichia coli* DH5α was used for cloning purposes and plasmid storage. *E. coli* cultures were started from cryo stocks, which were transferred on LB agar (Bertani, 1951). A single colony from such a plate was used to inoculate 5 mL of LB liquid culture containing the respective antibiotics, where applicable. Cells were incubated at 37°C. *E. coli* strains were stored at -80°C in 15% glycerol.

Table 2-1: Plasmids used in this study

Plasmids	Description	ABs	Reference
pBluescript II SK(+)	Backbone for integration vector	Amp	(Agilent technologies)
pSEVA234	Source for lac^{IQ}, P_{trc}, *neo*	Km	(Standard European Vector Architecture platform)
pEX-K4-adh	source for secondary alcohol dehydrogenase from *C. beijerinkii*	Km	(this study, Eurofins genomics)
pBS_*slr0168*::*trc*	pBluescript II SK(+) containing homologous regions for integration into slr0168 as well as lac^{IQ}, P_{trc}, *neo*	Km, Amp	(this study)
pBS_*slr0168*::*trc*:PG	pBluescript II SK(+) containing homologous regions for integration into slr0168 as well as lac^{IQ}, P_{trc}, neo, *mgsA, yqhD, adh*	Km, Amp	(this study)
pSEVA251	Backbone for replicative vector; broad host range vector with RSF1010 origin of replication	Km	(Standard European Vector Architecture platform)
pRSF_*trc*:PG	pSEVA251 containing lac^{IQ}, P_{trc}, neo, *mgsA, yqhD, adh*	Km	(this study)
pBR322	Backbone for integration*; E.coli* cloning vector with pMB1 origin of replication	Amp, Tc	(New England Biolabs, Ipswich, Massachusetts, USA)
pBR322_NS3::*trc*:PG	pBR322 containing homologous regions for integration into NS3 as well as lac^{IQ}, P_{trc}, neo, *mgsA, yqhD, adh*	Amp, Tc, Km	(this study)
pBR322_*glgC*::*aadA*	pBR322 containing homologous regions for replacement of *glgC* with a Sm resistance gene *aadA*	Amp, Tc, Sm	(this study)

The cyanobacterial strain *Synechocystis* sp. PCC 6803 (Stanier et al., 1971) was obtained from the Pasteur Culture Collection of Cyanobacteria (PCC, Paris, France). The *Synechocystis*ST wild-type, *ΔphaA,* and Δ*glgC* strains were generously supplied by the Hellingwerf lab (Van der Woude et al., 2014). Either BG11 medium (Stanier et al., 1971) or YBG11 medium (Shcolnick et al., 2007) was used for cultivation of *Synechocystis.* Agar plates containing the respective antibiotics were inoculated from a cryo stock and cultivated for 10 days under 25 µmol m^{-2} s^{-1} photosynthetically active radiation, ambient CO_2, 30°C, and 75% humidity in a polyklima incubator (Polyklima, Freising, Germany).

Table 2-2: Strains used in this study

Strains	Description	ABs	Reference
Synechocystis sp. PCC 6803	Wild-type strain	-	(Pasteur Culture Collection of Cyanobacteria)
SynechocystisST 6803	Stanford wild-type strain	-	(Van der Woude et al., 2014)
Synechococcus elongatus PCC 7942	Wild-type strain	-	(Pasteur Culture Collection of Cyanobacteria)
Synechococcus elongatus UTEX 2973	Wild-type strain	-	(UTEX algae culture collection)
Synechocystis sp. PCC 6803 PG	*lacIQ*, P_{trc}, *mgsA, yqhD, adh* integrated into *slr0168*	Km	(this study)
Synechocystis sp. PCC 6803 Δ*glgC*	Gene knockout of *slr1176/glgC* by replacement through Sm resistance gene (full segregation could not be achieved)	Sm	(this study)
Synechocystis sp. PCC 6803 Δ*glgC* PG	*lacIQ*, P_{trc}, *mgsA, yqhD, adh* integrated into *slr0168*; gene knockout of *slr1176/glgC* by replacement through Sm resistance gene (full segregation could not be achieved)	Km, Sm	(this study)
SynechocystisST 6803 Δ*glgC*	Stanford strain with gene knockout of *slr1176/glgC* by disruption through Cm resistance gene	Cm	(Van der Woude et al., 2014)
SynechocystisST 6803 Δ*glgC* PG	Stanford strain with *lacIQ*, P_{trc}, *mgsA, yqhD, adh* integrated into *slr0168*; gene knockout of *slr1176/glgC* by disruption through Cm resistance gene	Km, Cm	(this study)
SynechocystisST 6803 Δ*phaA*	Stanford strain with gene knockout of *slr1993/phaA* by disruption through Cm resistance gene	Cm	(Van der Woude et al., 2014)
SynechocystisST 6803 Δ*phaA* PG	Stanford strain with *lacIQ*, P_{trc}, *mgsA, yqhD, adh* integrated into *slr0168*; gene knockout of *slr1993/phaA* by disruption through Cm resistance gene	Km, Cm	(this study)
Synechococcus elongatus PCC 7942 PG	*lacIQ*, P_{trc}, *mgsA, yqhD, adh* integrated into NS3	Km	(this study)
Synechococcus elongatus UTEX 2973 PG	*lacIQ*, P_{trc}, *mgsA, yqhD, adh* integrated into NS3	Km	(this study)
Escherichia coli DH5α	Cloning strain	-	(Hanahan 1983)

Single colonies were transferred to fresh agar plates and spread to obtain enough biomass to inoculate 50 mL of YBG11 containing 50 mM HEPES buffer. Liquid *Synechocystis* cultures were grown in 250 ml baffled shaking flasks under increasing light intensity, 2% CO_2, 30°C, 150 rpm, and 75% humidity in an INFORS Multitron photosynthesis plus incubator (INFORS, Bottmingen, Switzerland), equipped with light-emitting diodes (spectrum see chapter 3.1, Figure 3-3). Cultures were inoculated to an OD_{750nm} of 0.2 for the main experiments. For long-term storage, the strains were frozen in YBG11 medium containing 8% dimethyl sulfoxide (DMSO) at -80°C.

2.3 Cultivation during $^{13}CO_2$-labeling experiments

For the aeration with $^{13}CO_2$ enriched air, cells were cultivated in 250 mL shaking flasks equipped with GL45 screw caps having three GL14 ports each. Two ports of each shaking flask were used for the aeration of the headspace and therefore connected by Tygon tubing (Tygon-R3607, ID 2.06 mm, Ismatec). One port was equipped with a septum and a 60 mm long hypodermic needle to enable gas tight sampling of the culture (Figure 2-1). The aeration was provided by three individual mass flow controllers, one for synthetic air (without CO_2), one for $^{n}CO_2$, and one for $^{13}CO_2$.

The gas stream was passed through a 0.2 µm sterile filter before entering the headspace of the cultures and before leaving the last cultivation vessel. The aeration was set to 25 mL min^{-1}. The gas mixture contained either 2% labeled or unlabeled CO_2. Due to the pressure loss, a maximum

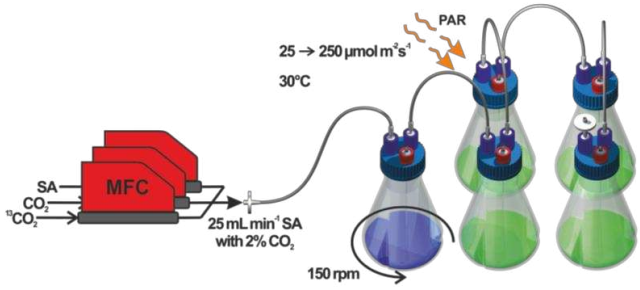

Figure 2-1: Cultivation setup during $^{13}CO_2$-labeling experiments

Experiments were carried out in serially connected 250 mL baffled shaking flasks with a culture volume of 50 mL under increasing light intensity (25 – 200 µmol m^{-2} s^{-1}), at 30°C, and 150 rpm. In this setup, the gas exchange did not take place via the incubator, but 25 mL min^{-1} synthetic air enriched with 2% either labeled or unlabeled CO_2 was supplied by three thermal mass flow controllers (MFCs). The shaking flasks were connected with Tygon tubing. Sampling took place with a septum and a hypodermic needle. After passing a sterile filter the air was directed through the headspace of 5 serially connected shaking flasks. The first shaking flask humidified the air stream. The remaining flasks were used for the cultivation of 4 biological replicates.

number of 5 flasks could be serially connected. The first shaking flask was filled with medium and used to humidify the air stream. This prevented evaporation from the 4 following cultivation flasks. With the exception of the aeration, cultivation took place as described before.

2.4 Bioreactor cultivation

The bioreactor experiments took place in 2 L flat-panel airlift photobioreactors (FPBR, INFORS Labfors 5 LUX, 20 mm deep culture vessel) and in 3 L stirred tank photobioreactors (STPBR, INFORS Labfors 5 LUX). Both reactor systems were equipped with LED arrays (spectrum see Figure 3-3) to provide PAR. Additionally, Hamilton pO_2 and pH probes and BlueSens BlueInOne off-gas analytics enabled the online measurement of the pH, dissolved oxygen, and CO_2 and O_2 concentrations in the off-gas. Aeration with either pressurized air (PA) or synthetic air (SA) enriched with 2% CO_2 was provided by respective thermal mass flow controllers (MFC, red-y, Vögtlin instruments) (Figure 3-19).

After assembly, autoclaving, and equilibration of the bioreactors, 2L YBG11 medium was inoculated to an OD_{750} of 0.2. Cultures were grown under increasing light intensity (25 - 250 µmol m^{-2} s^{-1}), at 30°C, 2% CO_2, and with 1 L min^{-1} (0.5 vvm) aeration.

For continuous cultivation, the system was equipped with two additional peristaltic pumps (IPC 4 peristaltic pump, Ismatec). The first pump provided fresh medium to the reactor, while simultaneously the second one kept the liquid level constant.

2.5 Biofilm cultivation

Cultivation of biofilms for the confocal laser scanning microscopy (CLSM) investigation took place in custom-made setups consisting of a medium reservoir (Figure 2-2, A), a multichannel peristaltic pump (Figure 2-2, B, IPC 4 peristaltic pump, Ismatec), a bubble trap (Figure 2-2, C), different biofilm reactors (Figure 2-2, E), and reservoirs collecting the waste (Figure 2-2, F). The custom-made flow-through reactors and the bubble trap were designed with Autodesk Inventor (Autodesk Inc., San Rafael, CA, US). Polylactic acid (PLA) prototypes were produced by fused deposition modeling (FDM) on a 3D printer (Leapfrog Creatr, Alphen aan den Rijn, Netherlands). Final parts were produced by selective laser sintering (SLS) of polyamide (SLS PA 12) or stainless steel (SLM 1.4542) by Blue Productions (Blue Production GmbH & Co. KG, Paderborn, Germany). The

components were serially connected by Tygon (Tygon-R3607, ID 2.06 mm, Ismatec, Wertheim-Mondfeld, Germany), PTFE (ID 1.6, OD 3.2 mm), and silicon tubing (ID 2.0, OD 4.0 mm).

In case of segmented flow, additional tubing was connected after the bubble trap and in front of the reactor via a T-connector (Figure 2-2 E.1, barbed, PP, 2.5 mm, T-shaped, Ismatec, Wertheim-Mondfeld, Germany) and sterile filter to introduce air segments. The sterile connection of the tubings to the medium and waste reservoirs was realized with GL45 screw caps with GL14 ports equipped with hose connections for 3 mm tubing and 0.2 µm pressure compensation filters (Figure 2-2, A.1, Duran Group, DWK Life Sciences, Mainz, Germany). PTFE tubing was used for the hose connectors, which was then connected to silicon tubing and finally via barbed connectors to the Tygon tubing (Figure 2-2, A.1). The inline bubble trap added after the peristaltic pump ensured that no unwanted air bubble could enter the reactor (Figure 2-2, C.1).

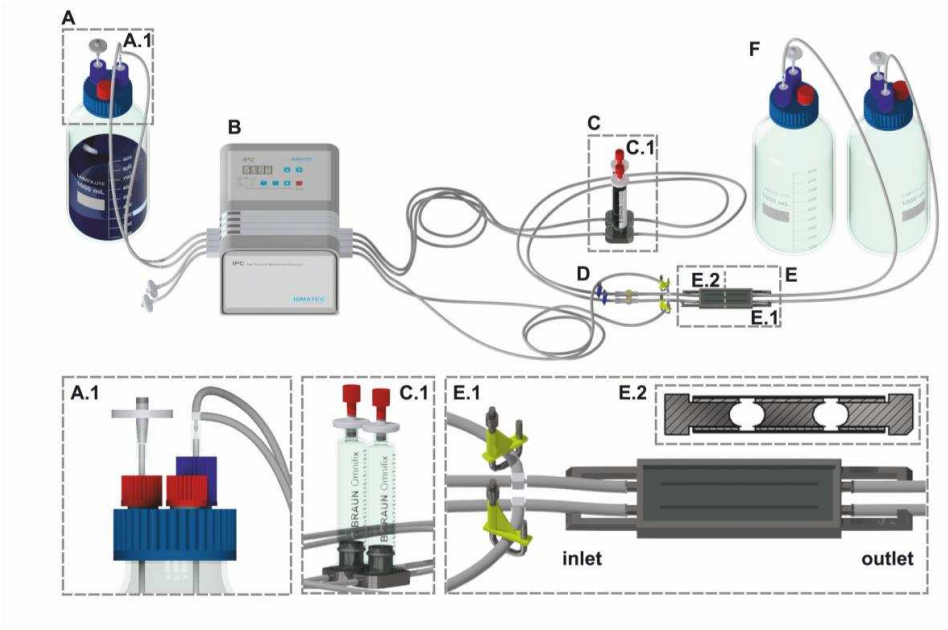

Figure 2-2: CLSM flow cell assembly

3-dimensional view of the cultivation system developed for the investigation of biofilms using CLSM. The figure shows the medium reservoir (A), the multichannel peristaltic pump (B, IPC 4 peristaltic pump, Ismatec), the bubble trap (C), the inline injection ports (D), the flow cell (E), and the waste reservoirs (F) with the respective tubing. Panels A.1, C.1, and E.1 are enlarged views of the screw cap connections, the bubble trap, and the flow cell, respectively. Panel E.2 shows a cross-section of the flow cell as indicated in the overview.

Finally, the different development stages of the flow-through CLSM reactor (Figure 2-2, E.1) were connected inline after the bubble trap. The components were either autoclaved before the assembly, or the system was chemically sterilized by a 0.5% sodium hypochlorite solution. Chemical sterilization was only applied in case that non-autoclavable reactor designs were tested. Afterward, the system was flushed with YBG11 and adjusted to 30°C and 55 µE m^{-2} s^{-1}. If not stated otherwise, the biofilm flow cells were inoculated with 800 µl of preculture with an OD_{750} of 1.0. Cell attachment occurred in 24 h without flow. Subsequently, the medium flow was started with 50 µl min^{-1}. To establish segmented flow, air segments with 50 µl min^{-1} were introduced after initial biofilm growth.

2.6 Construction of the 1,2-propanediol pathway

The genes *mgsA, yqhD*, and *adh*, enabling the production of 1,2-propanediol from DHAP, were integrated into the silent side *slr0168* (Williams, 1988) of *Synechocystis* by double homologous recombination. Therefore, the homologous regions for recombination were amplified from genomic DNA applying primers homI_fwd, homI_rev, homII_fwd, and homII_rev. The primers used for PCR amplification are listed in Table 2-3. Genomic DNA was isolated using the peqGOLD Bacterial DNA Mini Kit (VWR Peqlab, Darmstadt, Germany) upon cell disruption using a bead mill (0.2 µm glass beads, 8,000 rpm, 3 cycles of 30 seconds each).

The two derived PCR products were subsequently cloned into the vector pBluescriptII SK(+) (Agilent Technologies, Santa Clara, CA, USA) by Gibson assembly (Gibson et al., 2009) using restriction sites for KpnI, XhoI, SacI, and SacII, respectively. Digestion of plasmid DNA was carried out at 37°C for 16 h. The *trc* promotor system was amplified from pSEVA234 (SEVA collection, Centro Nacional de Biotecnología, Madrid, Spain) using *lacIQtrc*_fwd and *lacIQtrc*_rev and inserted between the two homologous regions using restriction sides XhoI and SacII, resulting in the vector pBS_slr0168::*trc*.

In the following, the genes *mgsA* and *yqhD* were amplified using *E.coli* MG1655 genomic DNA and primers *mgsA*_fwd, *mgsA*_rev, *yqhD*_fwd, and *yqhD*_rev (Table 2-3). The codon-optimized *adh* gene of *Clostridium beijerinkii* (Yan et al., 2009) was synthesized (Eurofins Genomics GmbH, Ebersberg, Germany) and amplified from the obtained vector pEX-K4_*adh* using CB*sadh*_fwd and CB*sadh*_rev.

Table 2-3: Oligonucleotides used in this study

Primer	Sequence		
	5`Extension	RBS	Binding Region
homI_fwd	CTATAGGGCGAATTGGGTACC	CCTTTGACAACAATGTGGCCTG	
homI_rev	GCTTATCGATACCGTCGACCTCGAG	TCCATATAAATCCCCGCCACTG	
homII_fwd	TCTAGAGCGGCCGCCACCGCGG	GACCAAGCCCAATTTCGTTTG	
homII_rev	CTAAAGGGAACAAAAGCTGGAGCTC	CCGCTAAACCCACCTCTTGC	
*lacIQtrc*_fwd	TGGCGGGGATTTATATGGACTCGAG	TCTAGGGCGGCGGATTTG	
*lacIQtrc*_rev	ACGAAATTGGGCTTGGTCCCGCGG	CAGCGGAAAAGGACAACGC	
*mgsA*_fwd	TATACGAAGCCGCCCGCTAAA	TAGTGGAGGTGTTACCATGGAACTGACGACTCGCAC	
*mgsA*_rev	CCCAGTCACGACGCGGCCGC	TTACTTCAGACGGTCCGCG	
*yqhD*_fwd	GCGGTTGTTATCCTGTAA	TAGTGGAGGTGTTACCATGAACAACTTTAATCTGCACACCCC	
*yqhD*_rev		TTAGCGGGCGGCTTCGTATATAC	
CB*sadh*_fwd	ACACCCTAGGCCGCGGCCGC	TAGTGGAGGTGTTACCATGAAAGGGTTTGCCATGTTAG	
CB*sadh*_rev		TTACAGGATAACAACCGCC	
*rnpB*_fwd		GAGTTAGGGAGGGAGTTGCGG	
*rnpB*_rev		TAATACGACTCACTATAGGGGCACTGTCCTCACGCTCGC	
*glgC*_cut1_fwd	ATCACGAGGCCCTTTCGTCTTCAAGAATTC	AATTCCGGTGAACCGTCG	
*glgC*_cut1_rev		TTCGAAGTCAAGTTTAGAACCG	
*glgC*_cut2_fwd	GCGAGATCACCAAGGTAGTCGGCAAATAAG	GGCCAGTTTCTTTCCTCG	
*glgC*_cut2_rev	TCGATGATAAGCTGTCAAACATGAGAATTC	TTTCTGCCCCTTGTCTGC	
Sm_fwd	CCTCGGTTCTAAACTTGACTTCGAAC	TTGGACTCCTGTTGATAGATCC	
Sm_rev		CTTATTTGCCGACTACCTTGGTG	
PG_fwd	CTCGACTTGACCAGCTGCTTAGCACTCTAG	CCAATCAAAATAACAGTGGC	
PG_rev	GGTTCGCATCGTCTCAGCCAGCTCATTCTT	ACCGCGGTCCAATTAATT	

The three derived fragments were combined by overhang extension PCR and cloned into the plasmid pBS_*slr0168*::*trc* using the Gibson assembly protocol and the restriction enzyme NotI. Fragments and PCR products were identified and selected by agarose gel electrophoresis and purified using a NucleoSpin Gel and PCR Clean-up kit (Macherey-Nagel, Düren, Germany). Gibson assembly was carried out at 50°C for 60 min using a Mastercycler pro PCR System (Eppendorf, Hamburg, Germany). Competent *E. coli* DH5α cells were transformed with the assembled DNA fragments by electroporation. Plasmids were isolated from LB overnight cultures using a peqGOLD Plasmid Miniprep Kit (VWR Peqlab, Darmstadt, Germany) and sequenced by Eurofins (Eurofins Genomics GmbH, Ebersberg, Germany).

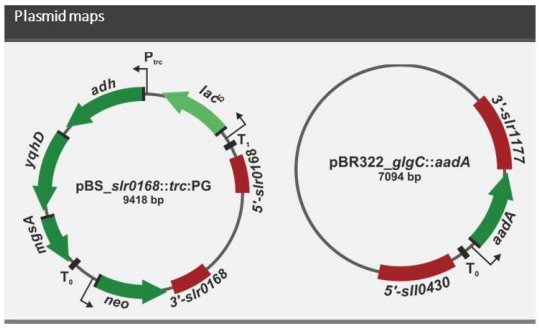

Figure 2-3: Plasmid maps

Plasmid maps of the applied plasmid for the integration of the 1,2-propanediol operon into the silent side *slr0168* of the *Synechocystis* chromosome (pBS_*slr0168*::*trc*:PG) and of the plasmid created for the knockout of the glucose-1-phosphate adenylyltransferase (Δ*glgC*) by replacement with *aadA* (streptomycin adenylyltransferase, pBR322_*glgC*::*aadA*). The sequences for homologous recombination are represented in red. A black arrow indicates the *trc* promotor. Genes are represented by green arrows, while the ribosomal binding sides (RBS) and terminators are indicated by a black bar.

The resulting vector pBS_*slr0168*::*trc*:PG (Figure 2-3) was used to transform the strains *Synechocystis* and *Synechocystis* Δ*glgC* creating the recombinant strains *Synechocystis* PG and *Synechocystis* Δ*glgC* PG (Figure 3-2). Complete segregation of the mutant allele in the created strains was reached by continuous cultivation on solid medium with increasing antibiotic concentrations and was verified by PCR with isolated genomic DNA as a template.

2.7 Construction of the *glgC* knockout in *Synechocystis*

The *glgC* gene was replaced by *aadA,* a gene establishing streptomycin resistance. Homologous regions for recombination (~850 bp) were amplified from genomic DNA applying primers *glgC*_cut1_fwd, *glgC*_cut1_rev, *glgC*_cut2_fwd, and *glgC*_cut2_rev (Table 2-3). The *aadA* gene was amplified from pSEVA451 using the primers Sm_fwd and Sm_rev. All three PCR products were subsequently cloned into pBR322 via three fragment Gibson assembly (Gibson et al., 2009) using the restriction site for EcoRI. The resulting vector pBR322_*glgC*::*aadA* was used to transform the strains *Synechocystis* and *Synechocystis* PG creating the recombinant strains *Synechocystis* Δ*glgC* and *Synechocystis* Δ*glgC* PG. Complete segregation of the mutant allele in the created strains was reached as described before.

2.8 Growth determination and light quantification

Planktonic cell growth was quantified by turbidity (OD_{750}, Libra S11, Biochrom Ltd, Cambridge, UK) and coulter counter (Multisizer 3, 20 µm aperture, Beckman Coulter, Brea, California, United States) measurements according to standard procedures. For the determination of cell dry weight (CDW), culture samples were centrifuged and dried at 60°C. Photosynthetically active

radiation (PAR) was determined with a MQS-B mini quantum sensor coupled to an ULM-500 light meter (Heinz Walz GmbH, Effeltrich, Germany).

2.9 Determination of glycogen and polyhydroxybutyrate content

For the determination of the concentration of storage compounds, a sample of 2 mL of the respective culture was centrifuged (17,000 × g, 10 min, 4°C). The pellet was washed once in ultraclean water and stored at -80°C. Isolation of glycogen was carried out according to a protocol modified from Gründel et al. (Gründel et al., 2012). Briefly, the cell pellet was resuspended in 500 µL of 30%$_{w/v}$ KOH in a 2 mL Eppendorf cup and afterwards incubated at 95°C, 600 rpm, for 2 h in a thermoshaker. The glycogen was precipitated by the addition of 1.5 mL ice-cold ethanol and subsequent incubation at -20°C for >4 h. Glycogen was received by centrifugation (17,000 × g, 10 min, 4°C), washed once with 75% ethanol and once with 98% ethanol. The remaining ethanol was evaporated in a thermoshaker at 65°C. The glycogen amount was determined either with a fluorimetric glycogen assay (glycogen assay kit, Cayman chemical, item no. 7000480) according to the distributors' protocol or by digestion with amyloglucosidase isolated from A*spergillus niger* and subsequent HPLC analysis (Aminex HPX-87H column (300 × 7.8 mm, Bio-Rad Laboratories GmbH, Hercules, California, USA), 5mM H_2SO_4, 0.8 mL min^{-1}, 65°C, refraction index detector). Commercially available glycogen from bovine liver (Sigma Aldrich, G0885-1G) was handled accordingly and used as standard.

Polyhydroxybutyrate (PHB) was determined as described previously (Taroncher-Oldenburg et al., 2000). The cell pellet was dried in a thermoshaker (95°C, 6 h), resuspended in 100 µL of concentrated sulfuric acid, and boiled at 95°C for 2 h in a thermoshaker. After dilution with 400 µL ultraclean water and centrifugation (17,000 × g, 10 min, 4°C), the supernatant was analyzed using HPLC (Thermo Fisher Scientific, Waltham, MA, USA), equipped with an Aminex HPX-87H column (300 × 7.8 mm, Bio-Rad Laboratories GmbH, Hercules, California, USA) and UV detector. Commercially available PHB (Sigma Aldrich, 363502) was used as a standard compound and handled accordingly.

2.10 Determination of 1,2-propanediol, acetol, methylglyoxal, nitrate, and phosphate

The supernatant of the Sy*nechocystis* cultures was analyzed with a Dionex Ultimate 3000 high-pressure liquid chromatography system (Thermo Fisher Scientific, Waltham, MA, USA) equipped with a refraction index, an UV detector and an Aminex HPX-87H column (300 x 7.8 mm, Bio-Rad Laboratories GmbH, Hercules, California, USA). The flow rate was set to 0.8 mL min^{-1} with 5 mM sulfuric acid as the eluent and a column temperature of 65°C. Standard curves for all compounds were prepared to quantify the product concentrations in the supernatant of the cultures.

2.11 GC-MS Analysis

For the verification of 1,2-propanediol production and the quantification of incorporated ^{13}C atoms into 1,2-propanediol, 50 microliters of culture supernatant were dried at 80°C. The remaining compounds were resuspended in 100 µL trifluoroacetic acid (TFA) containing 1% pyridine and derivatized with 20 µL of N-methyl-N-tert-butyldimethylsilyl-trifluoroacetamide (MBDSTFA, Macherey-Nagel, Düren, Germany). For the quantification of ^{13}C incorporation into the intracellular glycogen pool, glycogen was isolated and digested as described in the previous section. After the digestion, 40 µL were dried at 80°C, and resuspended in 100 µL TFA containing 1% pyridine. Derivatization was carried out with 20 µL of N,O-bis-trimethylsilyl-trifluoroacetamide (BSTFA) with 1% of trimethylchlorosilane (TMCS, silyl-991, Macherey-Nagel, Düren, Germany).

1 µL of the obtained sample was injected and separated on a Trace 1310 GC equipped with a TG-5MS column (40 m). 1,2-propanediol was separated with a temperature profile starting with 80°C for 1 min, followed by a ramp to 200°C with 15°C min^{-1} and then to 150°C with 25°C min^{-1}. At the end, the column was kept at 250°C for 1 min. For the separation of glucose, the column temperature was kept at 50°C for 1 min and afterwards ramped to 250°C with 15°C min^{-1}. Finally, the temperature was kept at 250°C for 4 min. For both methods, the nitrogen flow rate was set to 1.5 mL min^{-1}. Following the separation, samples were analyzed on an ISQ LT MS (Thermo Fisher Scientific, Waltham, MA, USA). The MS was set up for a full scan with a range from 50- 350 m/z in case of 1,2-propanediol and from 50-800 m/z for glucose. The obtained spectra were compared to the derivatized 1,2-propanediol (min. 99,5%, Bernd Kraft GmbH, Duisburg, Germany) and hydrolyzed glycogen standards for compound identification.

Quantification of mass isotopomer distributions for the MBDSTFA derivatized 1,2-propanediol, and the BSTFA derivatized glucose was performed in selective ion monitoring mode for the ion clusters m/z 247 to 250 and 360 to 368, respectively. These ion clusters correspond to fragment ions which are formed by loss of a tertbutyl group or trimethylsilyl groups from the respective derivatization residues and thus include the complete carbon skeleton of 1,2-propanediol or glucose. Samples were previously measured in full scan mode to exclude interference of analyzed products with impurities. The results were corrected for the natural isotopic distribution of the non-backbone carbon atoms and the non-carbon atoms applying the MATLAB (MathWorks, Natick, MA, US) function corrMatGen (Quek et al., 2009).

2.12 Mass spectrometric detection and quantification of proteins

Protein synthesis from the recombinant pathway genes was analyzed from 2 mL samples containing 10^8 *Synechocystis* PG cells per mL. Samples were harvested by centrifugation, lysed by bead beating, digested with trypsin and derivatized with iodoacetamide, all as described previously (Schipp et al., 2013). Samples were subsequently analyzed by nano-liquid chromatography linked to an Orbitrap mass spectrometer (nLC–MS/MS) on an Orbitrap Fusion instrument (Thermo Fisher Scientific, Waltham, MA, USA) equipped with a nanoUPLC system (nanoAcquity, Waters) as reported before (Marco-Urrea et al., 2011). Peptide identification was based on the protein sequences derived from *Synechocystis* PCC6803 genome (accession number NC_000911.1) and the sequences of *mgsA* (WP_000424181.1), *yqhD* (NP_417484.1) and *adh* (WP_077844196.1). All calculations were performed with ProteomeDiscoverer Version 2.2 (Thermo Fisher Scientific, Waltham, MA, USA) with SequestHT as the search engine using precursor and fragment mass tolerances of 3 ppm and 0.6 Da, respectively. The peptide identification threshold was set at a false discovery rate (FDR) of 0.01 based on the q-values comparing hits to target and decoy databases. The 'Minora Feature Detector' node, the 'Feature Mapper' node and the 'Precursor Ions Quantifier' node implemented in ProteomeDiscoverer V2.2 was used for label-free quantification on the basis of the intensities of precursor mass spectrometric traces and using the GAP-DH from *Staphylococcus aureus* as an internal standard. Relative abundance ranks of proteins were computed in Microsoft Excel on the basis of the label-free quantification output.

2.13 Northern Blot

For Northern Blot analysis, 10-25 mL of culture were filtrated through a Supor-800 Filter (Grid, 0.8 µm, 47 mm, Pall Life Sciences, Michigan, USA). Filter and retained biomass were dissolved in 1.6 mL of PGTX solution (Pinto et al., 2009) and frozen in liquid nitrogen. Samples were then thawed and incubated at 95°C for 5 minutes. Then, 200 µL of pre-cooled 1-bromo-3-chloropropane (BCP) was added to the samples. Phases were separated by centrifugation (4,700 × g, 15 min, 4°C) and the aqueous phase was again extracted with BCP. RNA was precipitated overnight (-20°C) by addition of isopropanol to the aqueous phase. After centrifugation, the RNA pellet was washed with 75% pre-cooled ethanol and dried at room temperature. 3 µg of total RNA were separated by electrophoresis on 1.3% denaturing agarose gels, blotted onto Roti-Nylon plus (Carl Roth, Karlsruhe, Germany) membranes and hybridized as described (Dienst et al., 2008). Hybridization probes were generated either by *in vitro* transcription of PCR fragments from the T7 promotor in the presence of [α-^{32}P]UTP using a T7 polymerase Maxiscript kit (Ambion, Thermo Fisher Scientific, Waltham, MA, USA) for *rnpB* or by labeling DNA fragments with [α-^{32}P]CTP using the Rediprime II DNA labeling system (GE Healthcare Life Sciences, Chicago, Illinois, US). Signals were detected and analyzed on a PhosphorImager (Typhoon FLA 9500, GE Healthcare Life Sciences). The oligonucleotides used for PCR amplification are listed in Table 2-3.

2.14 Confocal laser scanning microscopy and respective data analysis

Biofilm development on glass surfaces was monitored *in situ* using confocal laser-scanning microscopy (CLSM). Therefore, two different laser scanning microscope (LSM) systems were applied, a Zeiss LSM 5 Pascal and a Zeiss LSM 710 NLO (Carl Zeiss, Jena, Germany).

Autofluorescence of the cyanobacterial cells was excited with a laser wavelength of 488 nm and with either 543 nm or 633 nm. Thereby, taking advantage of the natural autofluorescence of chlorophyll and the phycobilins phycocyanin, allophycocyanin and allophycocyanin-B (Mariné et al., 2004; Vermaas et al., 2008). For photosynthetically nonactive cells, the autofluorescence of carotenoids was detected as described earlier (Schulze et al., 2011; Vermaas et al., 2008). Three dimensional (3D) biofilm image reconstructions were performed with IMARIS (Bitplane AG, Zürich, Switzerland).

3 Results

3.1 Catalyst development

Building on the study of Li and coworker, who enabled photoautotrophic 1,2-propanediol production in *Synechococcus* (Li and Liao, 2013), a three-step heterologous pathway for the synthesis of 1,2-propanediol was created. For the production of 1,2-propanediol, DHAP from the central carbon metabolism is converted into methylglyoxal by a methylglyoxal synthase in a first reaction step (Hopper and Cooper, 1971). Subsequently, methylglyoxal is reduced to acetol and then to 1,2-propanediol utilizing an aldehyde reductase and a secondary alcohol dehydrogenase, respectively. During the reduction of methylglyoxal to 1,2-propanediol, two reduced nicotinamide adenine dinucleotide phosphates (NADPH) are oxidized (Figure 3-1).

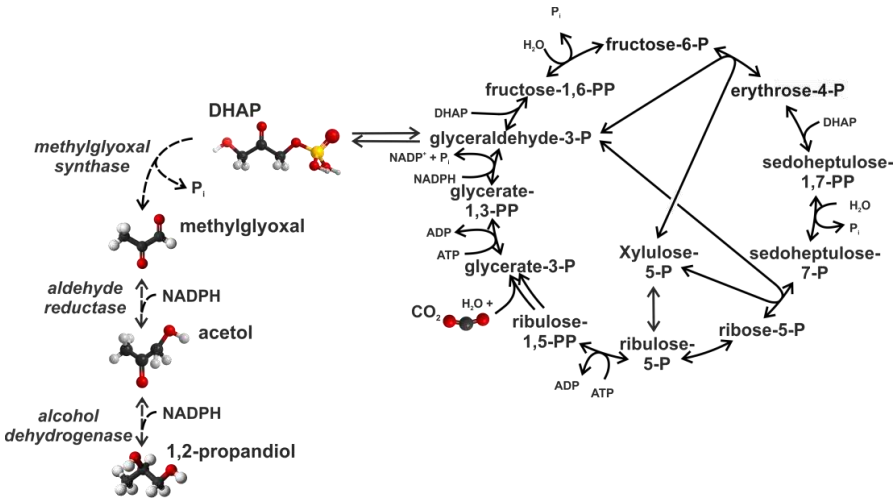

Figure 3-1: 1,2-propanediol pathway coupled to the Calvin cycle

Methylglyoxal synthase (MgsA, derived from *E.coli*) converts the precursor dihydroxyacetone phosphate (DHAP) derived from the Calvin cycle into methylglyoxal. Methylglyoxal is reduced to acetol by an aldehyde reductase (YqhD, derived from *E.coli*). Acetol is then further reduced to the final product 1,2-propanediol by a secondary alcohol dehydrogenase (Adh, derived from *Clostridium beijerinkii*). Thereby two NADPH are consumed.

For the implementation of the 1,2-propanediol pathway, the genes *mgsA* (methylglyoxal synthase) and *yqhD* (aldehyde reductase) derived from *E.coli* and *adh* (secondary alcohol dehydrogenase) obtained from *Clostridium beijerinkii* were amplified and organized into one operon controlled by a *trc* promotor (Figure 3-2). Promotors that are well characterized and often applied in heterotrophic lab strains lose much of their functionality if applied in cyanobacteria. Nevertheless, *lac* derived promotors were regularly applied for heterologous gene expression in *Synechocystis* and *Synechococcus* (Table 1-1). Thereof, the most frequently applied orthogonal

promotor is P_{trc} (Wang et al., 2012). While the achieved expression level is high, there is significant gene expression also in the absence of an inducer (Yu et al., 2013).

The broad host range plasmid RSF1010 and its origin of replication are often used if replication of the plasmid is wanted (Wang et al., 2012), whereas for recombination any high copy and narrow host range *E. coli* vector can be used. Both strategies, genome integration and expression from a replicating vector, have advantages and disadvantages. While the transformation with a replicative vector is efficient it was also reported that in some cases it was genetically less stable (Yu et al., 2013). In addition, it requires the continuing presence of a selection agent. In contrast, the chromosomal integration is time consuming due to the polyploidy of cyanobacterial genomes. However, once the pathway is integrated into all genome copies, it is genetically stable and does not require a selection agent. Also, due to several genome copies, the expression level is enhanced to a level comparable to that of medium copy number plasmids.

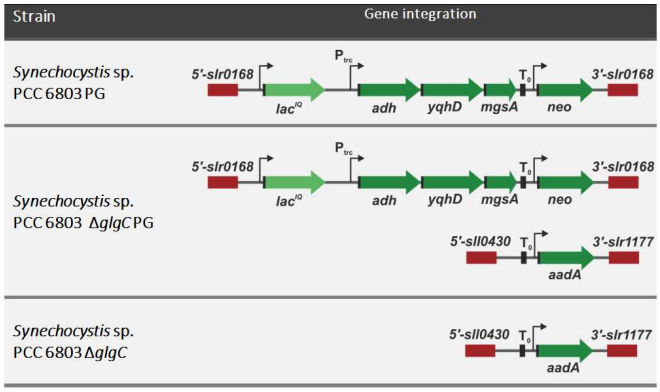

Figure 3-2: Assembly and integration of the 1,2-propanediol pathway and attempted deletion of the *glgC* (*slr1176*) gene

Schematic representation of the 1,2-propanediol operon integrated into the silent side *slr0168* of the *Synechocystis* chromosome in combination with the attempted knockout of the glucose-1-phosphate adenylyltransferase (Δ*glgC*) by replacement with *aadA* (streptomycin adenylyltransferase gene). The sequences for homologous recombination are represented in red. A black arrow indicates the *trc* promotor. Genes are represented by green arrows, while the ribosomal binding sides (RBS) and terminators are indicated by a black bar.

For chromosomal integration, the operon was additionally flanked by homologous regions for the recombination into the silent side *slr0168* (pBS_*slr0168*::*trc*:PG, Figure 2-3) of *Synechocystis.* The pathway was introduced into *Synechocystis* creating the strain *Synechocystis* PG. The integration of the pathway into the genome is visualized in Figure 3-2. DNA sequencing of isolated plasmid DNA and PCR products obtained from isolated genomic DNA confirmed sequence identity. The final plasmid used for integration and gene expression is shown in Figure 2-3.

3.2 Whole cell catalyst characterization

In the following experiments, the created PMCFs were investigated concerning their growth behavior, recombinant gene expression, and their capability to produce 1,2-propanediol. Characterization of the biocatalysts was performed in Erlenmeyer flasks. While this cultivation system is routinely applied for the cultivation of heterotrophic lab strains, it is not as well understood for growing photoautotrophic microorganisms. Therefore, standard cultivation procedures had to be established before the strains could be investigated.

Standard cultivation procedures

Photosynthetic active radiation. While incubators can be readily equipped with any light source to enable photoautotrophic growth, reproducibility of the experiments requires a consistent light composition and a uniform light distribution. Different light sources provide various light spectra. For example, the wavelengths emitted by white light fluorescent tubes and by white light emitting diodes (LEDs) are profoundly different (Figure 3-3). Phototrophic organisms showed different physiological reactions when exposed to different parts of the spectrum. Comparable results can only be achieved if the same light spectrum is provided for each experiment. LEDs were selected as the most suitable light source because their spectrum is similar to the spectrum of sunlight. With the ultimate goal to produce value-added compounds from sunlight and not artificial light, it is logical to choose a light source with a comparable spectrum.

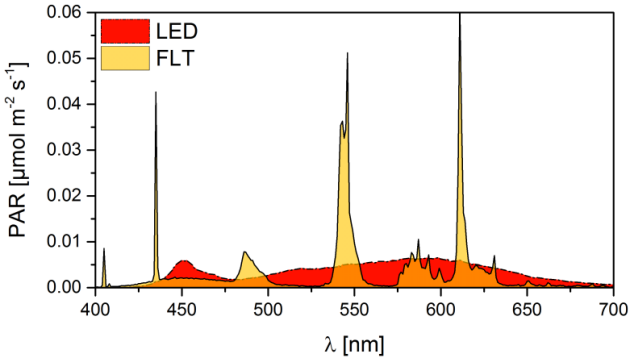

Figure 3-3: Spectrum provided by different light sources

Spectrum of fluorescent light tubes (in yellow) in comparison to light emitting diodes (LED, in red). Spectra are normalized to an irradiation intensity of 1 µmol m^{-2} s^{-1}.

Also, the uniform distribution of light inside the incubator is not easily achieved. Especially at the outer edges of the incubation platform, significant losses in light intensity can be detected (Figure 3-4). This drop in light intensity has a negative impact on growth and thereby influences the reproducibility of the experiments. This became especially evident at low light intensities. Exper-

iments were therefore restricted to the 8 central positions on the baseplate of the incubator (Figure 3-4, (X3,Y2)-(X6,Y3)). Furthermore, the working volume within the shaking flasks had to be restricted to prevent light or CO_2 limitation. Culture volume cannot exceed 20% of the shaking flasks volume without impacting growth. To exclude shadows caused by the metal clamps and to reduce abrasion to the glass, the shaking flasks were attached to sticky plates (INFORS, Bottmingen, Switzerland).

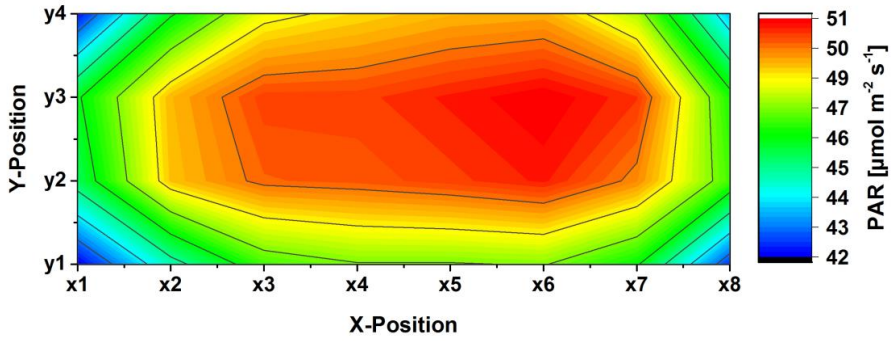

Figure 3-4: PAR measured on the baseplate of the incubator

PAR measured on the baseplate of the INFORS Multitron photosynthesis plus incubator for each of the 4x8 positions were 250 mL shaking flasks can be placed (Setpoint 50 µmol m^{-2} s^{-1}).

Dissolved inorganic carbon. The other major variable influencing the quality of the shaking flask experiments was the mass transfer of CO_2 to and from the shaking flask cultures. Mixing of the shaking flask cultures was limited by the shear forces affecting the cells. With baffled flasks, the shaking frequency was limited to maximal 150 rpm. At frequencies exceeding 150 rpm, a negative impact on growth was observed (data not shown). Therefore, 150 rpm was the standard shaking frequency for all subsequent cultivations. Additionally, the kind of sterile closure which was applied was apparently critical for reproducible cultivation. Standard aluminum caps did cause deviations during cultivation and led to a higher risk of contamination. Also, experiments with membrane type sterile closures used in cell culture did not improve results. Finally, commercially available wrapped paper plugs proved to be optimal. They resulted in a high reproducibility of growth and did successfully prevent contaminations.

Despite the paper plugs, the CO_2 supply was limiting growth at higher cell densities, and CO_2 availability had to be increased either by addition of sodium bicarbonate to the medium or by an increased partial pressure of CO_2 within the incubator. The repeated addition of sodium bicar-

bonate to the culture caused a repeated fed-batch type of cultivation and diluted the culture. Therefore, and for the ease of handling, CO_2 was supplied via the gas phase by 2% CO_2 enriched air. Likewise, due to the mass transfer resistance, the culture volume inside the 250 mL Erlenmeyer flasks was limited to maximal 50 mL (20%) to prevent carbon dioxide limitation.

Water evaporation. Finally, cultivation times >21 days required an elevated humidity inside the incubator to reduce evaporation. As a compromise between evaporation and water condensation within the incubator, the humidity was adjusted to 75%. With an established reproducible cultivation routine in Erlenmeyer flasks, experiments for the characterization of the constructed biocatalyst were conducted.

Growth of *Synechocystis* PG is unaffected by recombinant gene expression

To elucidate how the recombinant genes influenced the physiology of the 1,2-propanediol producing strain *Synechocystis* PG, initial shaking flask experiments have been conducted.

Growth phases of photoautotrophic strains differ from those observed with heterotrophic strains. According to Schuurmans et al. and based on the measurement of optical density, the growth phases can be distinguished into the *lag*-phase, an exponential growth phase, a linear growth phase, and a late growth phase (Schuurmans et al., 2017). A schematic representation of a photoautotrophic growth curve is given in Figure 3-5. The development of the optical density (OD) and the cell concentration is shown exemplarily over the time course of a batch cultivation.

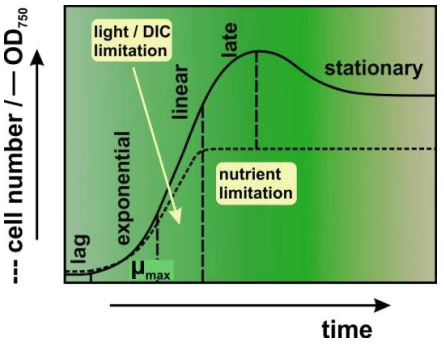

Figure 3-5: Schematic representation of an exemplary growth curve of a photoautotrophic microorganism

Schematic growth curve of a photoautotrophic strain divided into growth phases based on OD and cell concentration. Growth can be divided into a lag phase, an exponential phase with maximal growth rate, a linear growth phase caused by either light or CO_2 limitation, followed by a late growth phase without cell division but with an ongoing accumulation of storage compounds and a stationary phase.

While the *lag* and exponential phase are also observed with heterotrophic growing cultures, the linear, late and stationary phases are connected to the photoautotrophic growth. At a specific cell density, the availability of PAR is decreased by self-shading of the culture leading to an energy limitation (Sutherland et al., 1979). As a result, the linear phase resembles a linear fed-batch experiment where light is supplied with a constant rate and limits growth. If insufficient DIC is

supplied, also a carbon limitation can be the cause of the linear growth phase. Later on, a nutrient that is neither the carbon nor the energy source becomes limiting. This is reflected by a decreasing slope of the OD curve. Based on the still increasing biomass, this phase is characterized as late growth phase. Finally, in the stationary phase, not the absence of a carbon and energy source limits growth, but another nutrient limitation. This limitation prevents the production and replacement of the photopigments, which in the end causes bleaching of the culture and finally, when the remaining storage compounds are depleted, cell lysis (Figure 3-5).

The detection of growth via measurement of the optical density at 750 nm (OD_{750}) is only accurate if the optical relevant properties of the cells remain unchanged during the cultivation. Cell size, cell shape, and cell content influence the OD measurement. This becomes apparent during the late and stationary growth phase where in comparison to the OD signal the cell number remains constant. Some evidence was found, that the accumulation of intracellular storage compounds causes the observed increase in OD during the late growth phase. This will be discussed in detail later on (chapter 3.4).

Based on the introduced growth phases, the growth of both the *Synechocystis* wild-type and the recombinant strain were characterized. *Synechocystis* PG was more sensitive to high light intensities. Especially, during the initial growth phase, growth ceased and cells lysed when the light intensity was higher than 25 µmol m^{-2} s^{-1}. Therefore, a light ramp had to be implemented which increased with the growth of the culture (Figure 3-6, PAR). This light ramp became part of the standard cultivation procedure and was implemented in all following experiments. *Synechocystis* PG and the wild-type showed no significant differences in growth during the exponential, linear, and late growth phase (Figure 3-6).

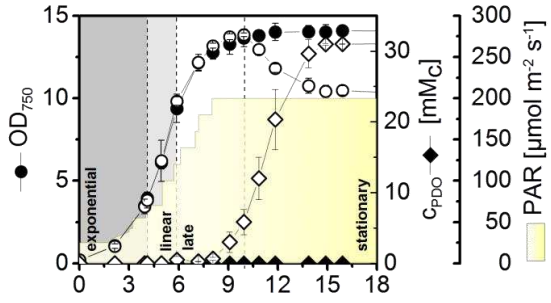

Figure 3-6: Growth and 1,2-propanediol production of *Synechocystis* PG in comparison to the wild-type

Growth and 1,2-propanediol production of *Synechocystis* PG (white symbols) in comparison to the wild-type (black symbols). Experiments were carried out in 250 mL baffled shaking flasks with a culture volume of 50 mL under increasing PAR (25 – 200 µmol m^{-2} s^{-1}), at 2% CO_2, 30°C, 150 rpm, and 75% humidity in an INFORS Multitron photosynthesis plus incubator. Mean values and standard deviation of 3 biological replicates are shown.

However, while for the wild-type strain a stable OD_{750} value was observed during the stationary phase, the OD_{750} of the PG strain decreased from 14 to 10 within 5 days. Applying a light regime

starting with 25 µmol m^{-2} s^{-1} and increasing up to 200 µmol $m^{-2}s^{-1}$ over cultivation time (Figure 3-6, PAR) and elevated CO_2 concentrations (2%), enabled an exponential growth phase up to an OD_{750} of 4 with a growth rate of 0.032 h^{-1}. After that, the culture grew linear up to an OD_{750} of 14 until growth ceased completely. The expression of the heterologous genes did not impair growth of the recombinant strain.

1,2-propanediol formation mainly in the stationary phase

Functionality and productivity of the heterologous pathway were investigated in shaking flask experiments. 1,2-propanediol was detected in the supernatant of the culture only during the late and stationary growth phase of the recombinant strain (Figure 3-6). Induction of the *trc* promotor with isopropyl β-D-1-thiogalactopyranoside (IPTG) did not lead to an increased product formation rate, indicating leaky expression. With an optimized growth protocol applying an elevated CO_2 concentration of 2% and increasing light intensity up to 200 µmol m^{-2} s^{-1}, a final titer of 12 mM (900 mg L^{-1}, 36 $mmol_C$ L^{-1}) 1,2-propanediol was achieved, with a peak volumetric production rate of 2.8 mM day^{-1}, representing a maximal specific activity of 55 µmol h^{-1} g_{CDW}^{-1}. Only minor amounts of acetol (<1 mM) and no methylglyoxal were detected. The production of 1,2-propanediol was verified by gas chromatography-mass spectrometry (GC-MS).

Finally, the stability of the pathway integration was evaluated by repeated cultivation on agar plates and in liquid culture without selection pressure (Data not shown). No indication for gene instability was observed. Experiments with increasing 1,2-propanediol concentrations in the culture showed no indication for product toxicity, product inhibition or product degradation by the catalyst (Appendix, Figure 7-1).

Transcript accumulation during the growth phase of *Synechocystis* PG

Next to the regulation of the carbon flux towards DHAP, the expression of the genes encoding for the 1,2-propanediol synthesis pathway is essential for activity. As no product could be detected before day 8 (Figure 3-6), the expression of the operon encoding the respective production pathway was investigated, especially in the non-productive phase.

Thus, a cultivation experiment under optimized conditions was performed, and next to biomass and product formation, also the transcripts of *mgsA, yqhD*, and *adh* (by northern blotting) and the corresponding proteins (by mass spectroscopy) have been investigated. Accumulation of product was detected starting from day 8 when the culture enters the late growth phase (Figure

3-7, A). The production rate increased slightly with biomass, with a rather constant specific activity of approximately 1.8 µmol g_{CDW}^{-1} h^{-1} (14 fmol $cell^{-1}$ h^{-1}) until day 12.

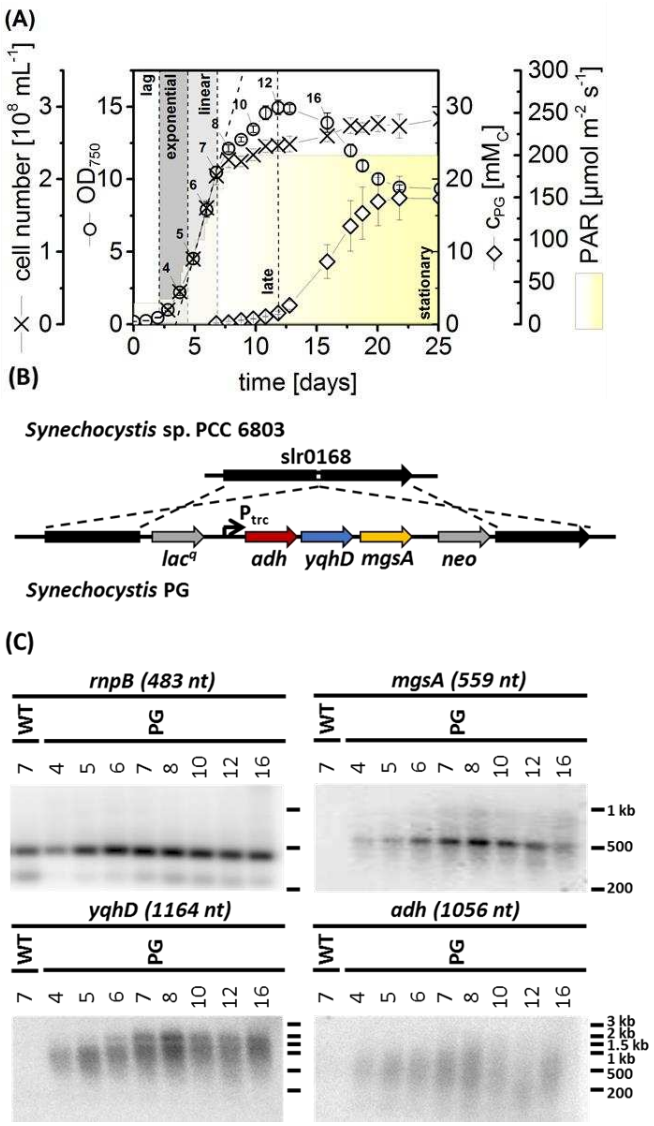

Figure 3-7: Transcript accumulation of the genes of the production cassette

(A) Growth and 1,2-propanediol production of *Synechocystis* PG. Note that the growth curves have not been corrected for the evaporation of the aqueous phase during the long cultivation times.

(B) Scheme of the recombination cassette for the construction of *Synechocystis* PG. RBS were placed in front of each individual gene, but are not indicated here.

(C) Northern Blot showing the transcript of the PG operon, using probes against the individual pathway mRNAs *adh*, *yqhD*, and *mgsA* during cultivation. DNA hybridization probes covered the complete coding region of the respective genes. Timepoint of sampling is indicated in days. RNA quality and equal loading were checked using the housekeeping *rnpB* gene. Wild-type RNA was used as a negative control.

Starting with day 12 and the transition from late growth to the stationary phase, a significant increase in 1,2-propanediol production was observed, with specific activities which were almost 10× higher (16.5 µmol h^{-1} g_{CDW}^{-1}, 130 fmol h^{-1} $cell^{-1}$) in comparison to the late growth phase. The corresponding Northern Blot is shown in Figure 3-7, C. Hybridization with the housekeeping gene *rnpB* verified the overall quality of RNA isolation. The length of the operon was expected to be 2779 bp with *adh* being 1057 bp, *yqhD* 1164 bp, and *mgsA* 559 bp long. However, the predicted

full-length polycistronic mRNA was not detected by Northern Blot analysis. The bands derived from hybridization with the *adh* and *yqhD* probes are of varying size, ranging from 200 to 2000 nt indicating an unstable full-length transcript. The hybridization with the *mgsA* probe resulted in a distinct band of approximately 550 nt suggesting stabilization of the 3`end of the transcript due to the addition of a terminator sequence at the end of the operon (Figure 3-2, page 39). The other transcripts became more stable until day 8 of cultivation, which coincides well with the accumulation of the product. As neither methylglyoxal nor acetol accumulated in the culture, it can be assumed, that although stable full-length mRNA could not be detected, diverging stability of the transcript was not limiting for production.

In addition to the Northern Blot analysis, samples for shotgun proteomics were taken after days 3.8, 5.9, 8.0, and 10.9 with the wild-type strain serving as negative control. Two biological replicates were analyzed. While it was not possible to detect MgsA, the other two proteins of the pathway (YqhD and Adh) have been detected at all time points (Appendix, Table 7-1).

In conclusion, transcript of *mgsA* could be detected during the cultivation, while the presence of MgsA itself could not be verified. The opposite is true for the remaining part of the pathway. While Northern Blotting could not verify the transcript of *yqhD* and *adh*, the respective proteins could be detected. Without evidence for the presence of MgsA, an influence on the activity of the pathway on the translational level cannot be excluded.

Identification of growth-limiting factors

To increase cell density and thereby the final product concentration, experiments with increased nutrient availability were performed. Therefore, *Synechocystis* PG was grown in 2x concentrated YBG11 medium, but elsewise under the same cultivation conditions as described before (Figure 3-8). No differences during the exponential growth phase in comparison to the control culture grown on normal YBG11 could be observed. The increased amount of nutrients in the 2x YBG11 resulted in a prolonged linear growth phase. However, the maximal observed OD of 22.4 is only 1.6x higher in comparison to the 13.9 observed with the control, indicating light or CO_2 limitation.

In contrast to the maximal OD, the final 1,2-propanediol concentration is lowered despite the increased biomass concentration. Whereas the control strain produced 10.2 mM 1,2-propanediol, only 4.6 mM were produced by the strain growing in 2x YBG11 medium. The reduced titer of 1,2-

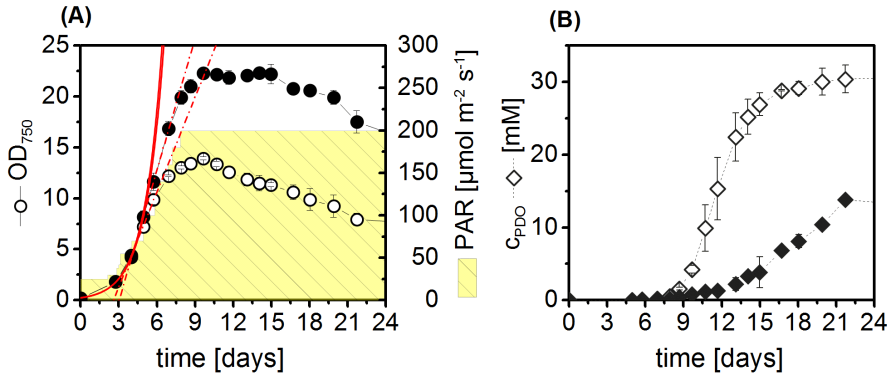

Figure 3-8: Growth and 1,2-propanediol production with increased nutrient availability

(A) Growth (OD_{750}) of *Synechocystis* PG cultures in YBG11 (white symbols) and doubled concentrated (black symbols) YBG11 medium. **(B)** 1,2-propanediol concentrations during cultivation. Mean values and standard deviation of 4 biological replicates are shown.

propanediol despite the increase in biomass together with the observation that product formation occurs only during the transition to and within the stationary phase raised the question how the activity of the recombinant pathway is related to the limitation of cell growth.

A special focus was placed on the identification of limiting factors responsible for the growth arrest. As 2x BG11 medium enabled higher biomass formation, one component of the growth medium YBG11 became limiting during standard cultivation. YBG11 contains 17.5 mM sodium nitrate and 0.175 mM dipotassium hydrogen phosphate as nitrogen and phosphate source, respectively. HPLC analysis of the supernatant of *Synechocystis* and *Synechocystis* PG cultures during cultivation revealed that when the cultures enter the stationary phase, nitrate is still present in the supernatant (data not shown). In contrast, phosphate could not be detected in the culture supernatant after the early growth phase (initial 5 days) of the culture (YBG11, Figure 3-9, B). Cultures of *Synechocystis* PG were therefore grown in YBG11 medium containing different amounts of dipotassium hydrogen phosphate (0, 25, 50, 75, 100, 150, and 200% of the phosphate amount initially present in YBG11) (Figure 3-9). Final biomass titers correlated linearly between 0 and 100% of added phosphate (Figure 3-9, C). A further increase in phosphate availability only had a slight effect on biomass titers. The maximum OD value reached was 16 at 150%, and 200% added phosphate. This indicates that another component of the medium became limiting at that time point.

The phosphate concentration heavily influenced product formation. Significant amounts of the product could only be detected for cultures grown in media containing 100% phosphate or more

(Figure 3-9, B). The maximum product amount of 9 mM (685 mg L^{-1}, 27 $mmol_C$ L^{-1}) 1,2-propanediol was measured for medium supplied with 100% phosphate (Figure 3-9, C). At concentrations exceeding 100% phosphate, the productivity for 1,2-propanediol formation decreased significantly, indicating an inhibitory effect on the respective enzymes. This provided evidence that the presence of phosphate strongly influenced growth and productivity of *Synechocystis* in YBG11. A phosphate limitation is likely to initiate the entrance of the cells into the stationary phase under the conditions applied. Although relieving this limitation leads to higher biomass titers, it concomitantly results in significantly lower 1,2-propanediol titers. Apart from nitrogen, phosphate, CO_2, and light, no other compound has been evaluated for possible growth limitation in this study.

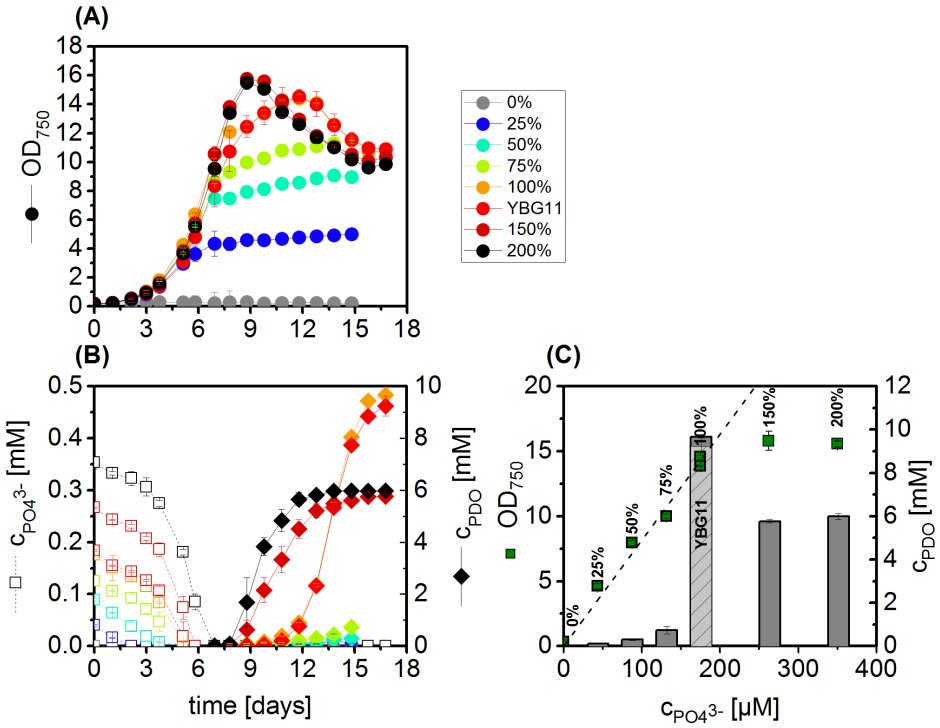

Figure 3-9: Influence of phosphate availability on growth and 1,2-propanediol production

(A) Growth (OD_{750}) of *Synechocystis* PG cultures in YBG11 medium containing different phosphate concentrations relative to the standard phosphate content (0.175 mM) of YBG11 medium (0, 25, 50, 75, 100, 150, 200%, increasing gray scale of symbols corresponding to increasing phosphate concentration) Note that the growth curves have not been corrected for the evaporation of the aqueous phase (0.2 mL day^{-1}) during the long cultivation times. **(B)** Phosphate and 1,2-propanediol concentrations during cultivation **(D)** Correlation of maximal OD_{750} value to supplied phosphate concentrations and maximal 1,2-propanediol titers. Mean values and standard deviation of 2 biological replicates are shown.

To conclude, the final product titer cannot merely be improved by increasing the amount of pre-dissolved nutrients. A deeper understanding of the interconnection between nutrients, PAR, DIC, and the performance of the biocatalyst is necessary to develop rational process and reaction engineering strategies leading to enhanced product titers.

3.3 Influence of the key substrates light and carbon dioxide on growth and productivity of *Synechocystis* PG

Nutrient supply and feeding strategy can have a considerable influence on the effectivity of microbial fermentation processes. Precursor and energy for the synthetic 1,2-propanediol pathway have to be provided by the host cell. In contrast to heterotrophic cultivations, both, carbon and energy, are not previously solubilized in the aqueous phase. In a standard heterotrophic cultivation carbon and energy are derived from the same soluble organic substance, which is heterogeneously distributed within the liquid phase. The energy source of photoautotrophic growing bacteria is light, which has to be provided in sufficient amounts to allow growth. Light differs in its characteristics from other substrates. It cannot be supplied in the medium or via aeration. Mass transport hindrance is of no importance with light as substrate. A light source with a characteristic spectrum generates photosynthetic active radiation (PAR). Its overall intensity of PAR alone can not sufficiently describe the light. The energy source light needs to be characterized by the contained wavelengths and their intensity distribution. With increasing cell concentration, the light is absorbed and thereby diminished already in the outer layers of the culture and no homogeneous light distribution within the culture can be achieved. The carbon source utilized by *Synechocystis* PG is CO_2, which has to be supplied via the gas phase to the culture. In the following, the influence of these substrates on growth and propanediol production is investigated.

Influence of different light intensities on the growth phases of *Synechocystis* PG

The different growth phases of a phototrophic batch culture can be distinguished into *lag*, exponential, linear, late, and stationary phase as already described exemplarily in chapter 3.2. Out of these, only the exponential and linear growth phases were influenced by the light intensity in these experiments. During the exponential growth phase, a consistent growth rate of 0.039±0.001 h^{-1} (Figure 3-10, Table 3-1) was observed, independently of the provided light intensity. However, the available light intensity determined the transition point from exponential to linear growth and thereby the length of the exponential phase. In the following linear growth phase, the growth rate was rising with increasing light intensity (Table 3-1).

Light intensities of 50 µmol m^{-2} s^{-1} and below did not provide enough energy for the cells to grow exponentially to an optical density higher than 3 and thereby caused a prolonged linear growth

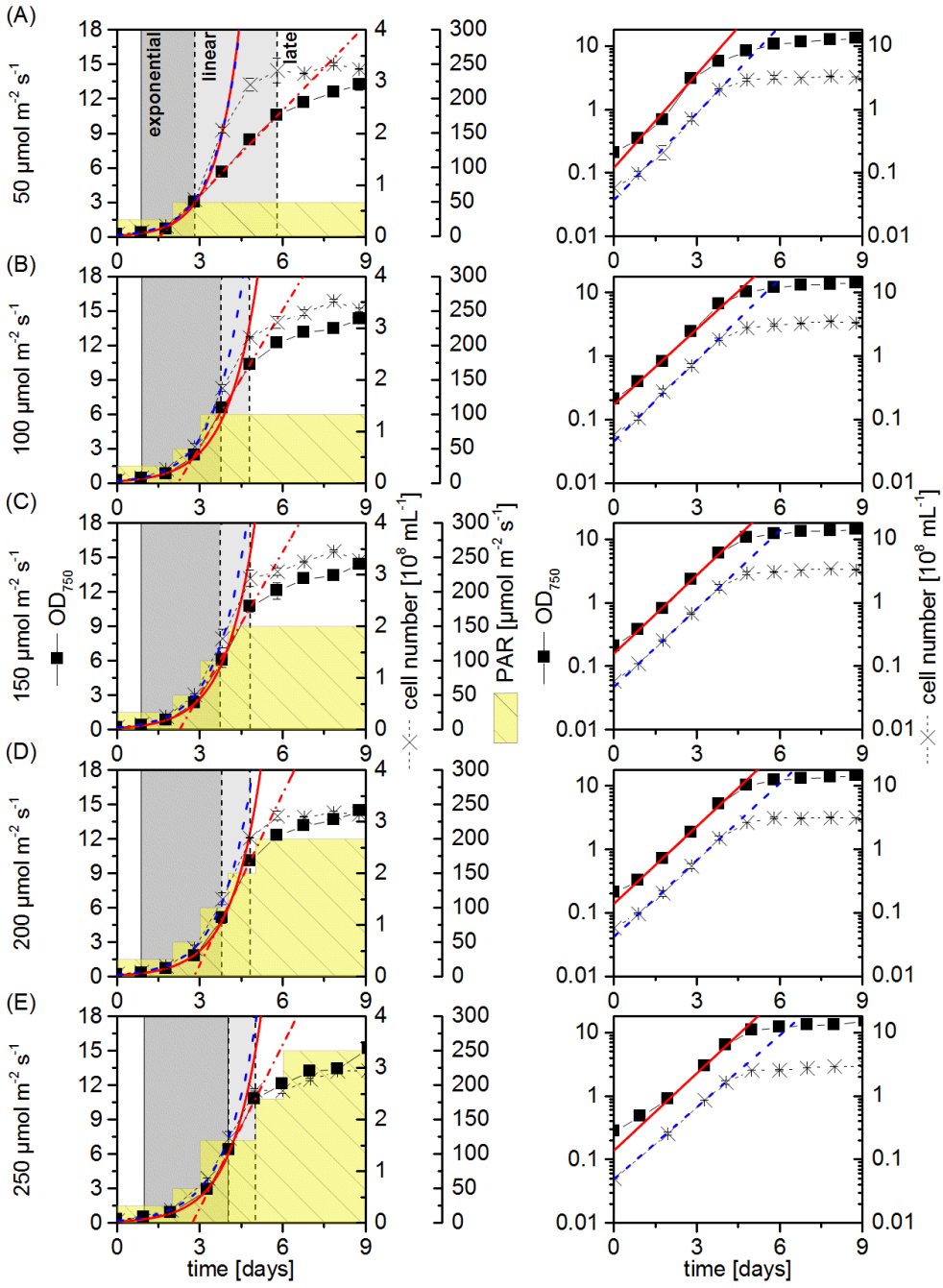

Figure 3-10: Influence of different light intensities on the growth of *Synechocystis* PG

Optical density and cell concentration on a linear (**left column**) and logarithmic scale (**right column**) measured during shaking flask cultivations with *Synechocystis* PG. The light intensity is increased stepwise during cultivation. The final light intensities supplied were 50, 100, 150, 200, and 250 µmol m^{-2} s^{-1}, increasing from the top to the bottom row. Cultivation took place at 30°C, 150 rpm, 75% humidity, and under 2% CO_2 enriched atmosphere (growth rates and main data points summarized in Table 3-1).

Table 3-1: Maximal exponential and linear growth rates determined for different final light intensities under 2% CO_2

PAR [µmol m^{-2} s^{-1}]	µ [h^{-1}, ±0.001]	r_L [h^{-1}, ±0.004]	$OD_{750,max}$ [/, ±0.25]	$\mu_{cell\ \#}$ [h^{-1}, ±0.002]	$\#_{cell,max}$ [10^8 mL^{-1}, ±0.2]
50	0.047	0.10	14.8	0.044	3.8
100	0.038	0.17	15.1	0.041	3.9
150	0.040	0.18	14.9	0.039	3.8
200	0.039	0.21	15.5	0.039	3.6
250	0.039	0.20	15.2	0.036	3.3

Data derived from Figure 3-10 and Figure 3-11.

phase (Figure 3-10, A). The stronger energy limitation due to the lower light intensity led to a low linear growth rate of 0.10 h^{-1} (Table 3-1). Intensities of PAR of 100 µmol m^{-2} s^{-1} and above allowed for an exponential growth up to an optical density of approximately 6. The corresponding linear growth rates were increasing from 0.1 to 0.2 when the light intensity increased from 50 to 200 µmol m^{-2} s^{-1}. An even higher light intensity of 250 µmol m^{-2} s^{-1} did not increase the linear growth rate any further. The analysis of the exponential growth rate based on the cell concentration during the exponential phase resulted in similar growth rates (Table 3-1). The transition of the linear to the late growth phase was independent of the light intensity, as was the maximal reached optical density. In contrast to that, the final cell concentration was slightly decreasing by 5-15% at high light intensities (200 vs. 250 µmol $^{-2}$ s^{-1}, Table 3-1). A more precise assessment of the growth rates and phases would demand an experiment with a higher sample frequency, which is difficult to realize in a 50 mL shaking flask scale. However, the differences in the linear growth rates caused by the increased light intensity hardly influenced the process time and the space-time yield. Therefore, they are of minor importance for process development.

Influence of increasing PAR on the glycogen and propanediol production in *Synechocystis* PG

While the impact of the available light intensity on the growth and thereby the process duration was of minor importance, a significant effect of this parameter was seen on the propanediol production. Thus, the propanediol and glycogen concentrations have been determined for the cultivations shown in Figure 3-10. The maximal produced glycogen concentration was increasing from 18.5 to 27.5±1.0 mM_C with increasing final light intensities (Table 3-2).

Table 3-2: Maximal Glycogen and propanediol concentrations, as well as production and turnover rates measured at different final light intensities

PAR [µmol m^{-2} s^{-1}]	$c_{PDO,max}$ [mM_C, ±0.8]	$r_{PDO,max}$ [mM_C d^{-1}, ±1.6]	$c_{Gly,max}$ [mM_C, ±1.0]	$r_{Gly,max}$ [mM_C d^{-1}, ±2.0]
50	19.3	3.0	18.5	-4.1
100	21.1	3.2	22.6	-4.9
150	21.5	3.2	23.3	-4.4
200	28.4	5.4	26.4	-6.4
250	30.4	8.3	27.5	-7.2

Data derived from Figure 3-11.

The initiation of glycogen turnover was congruent with the beginning of the stationary phase. Based on the measured concentrations, the maximal glycogen degradation rate was determined (Table 3-2, Figure 3-11). The rate of glycogen turnover was increasing from 4.1 mM_C d^{-1} at 50 µmol m^{-2} s^{-1} to 7.2±2.0 mM_C d^{-1} at 250 µmol m^{-2} s^{-1}.

The same trend was observed for propanediol. Final propanediol concentrations were increasing from 19.3 to 30.4±0.8 mM_C with increasing final light intensities, while the 1,2-propanediol production rate rose from 3.0 to 8.3±1.6 mM_C d^{-1} when the final light intensity increased from 50 to 250 µmol m^{-2} s^{-1}. The highest increase in concentrations and rates was observed when the threshold of 200 µmol m^{-2} s^{-1} was exceeded. Especially for the propanediol production, only a minor increase in concentration and rate was observed when the light intensity increased from 50 to 150 µmol m^{-2} s^{-1}. Only after the light intensity was increased further to 200 µmol m^{-2} s^{-1}, an increase of 33% could be achieved.

Experiments with higher light intensities of 300 µmol m^{-2} s^{-1} and more would be interesting, but could not be tested due to technical limitations of the incubator system, which is not capable of providing light intensities above 270 µmol m^{-2} s^{-1}. Photobioreactor experiments with higher light intensities up to 400 µmol m^{-2} s^{-1} revealed that *Synechocystis* PG is not capable of utilizing further increased PAR (data not shown).

In conclusion, light intensities of 200 - 250 µmol m^{-2} s^{-1} should be applied for maximal productivity as the increased light intensity had a positive impact on the propanediol titer and rate. With the increased rate, the final titer could be achieved within 14 days, whereas it takes up to 5 days longer with light intensities below 200 µmol m^{-2} s^{-1}.

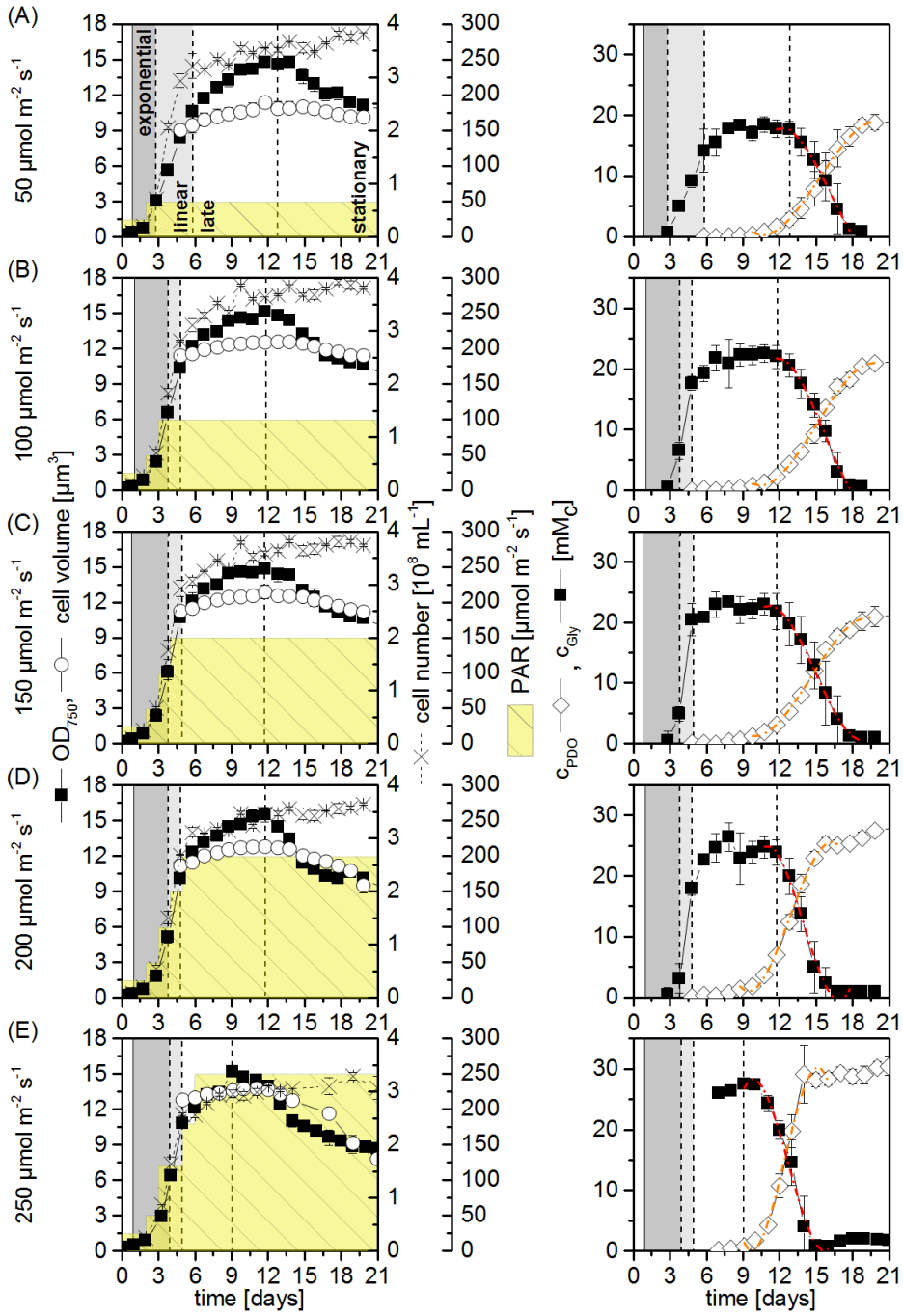

Figure 3-11: Influence of different light intensities on the glycogen and propanediol formation of *Synechocystis* PG

Optical density and cell concentration as well as the cellular volume (**left column**, classification of growth phases see Figure 3-10) and propanediol and glycogen concentrations in mM_C (**right column**) measured during shaking flask cultivations with *Synechocystis* PG. The light intensity was increased stepwise during cultivation. The final light intensities supplied were 50, 100, 150, 200, and 250 µmol m^{-2} s^{-1}, increasing from the top to the bottom row. Cultivation took place at 30°C, 150 rpm, 75% humidity, and under 2% CO_2 enriched atmosphere (main data points summarized in Table 3-2).

Influence of CO_2 availability on the growth phases of *Synechocystis* PG

Carbon dioxide is the sole carbon source for growth of the PMCF as well as for the production of 1,2-propanediol. Therefore, the impact of a carbon dioxide limitation on *Synechocystis* PG was investigated. Cultures were incubated under a light regime that allowed for exponential growth up to an optical density of above 6 (Figure 3-13), as could be seen in previous experiments. Under these conditions, the influence of ambient (0.04%), 2%, and 5% carbon dioxide in the atmosphere of the incubator (Figure 3-13, A-C) was investigated.

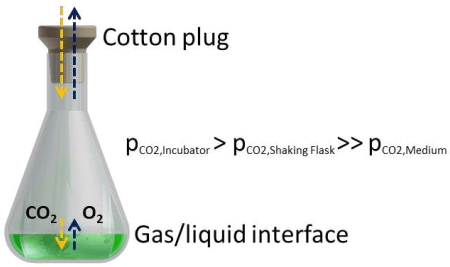

Figure 3-12: Schematic drawing of CO_2 mass transfer into a shaking flask

Diffusion of carbon dioxide from the CO_2 enriched atmosphere of an incubator via a sterile closure into baffled shaking flasks and the culture.

The equilibrium concentration of dissolved CO_2 in solution depends on the partial pressure of CO_2 in the surrounding gas phase. The ratio of both partial pressures, in the headspace and the solution, is given by the Henry coefficient for CO_2 (Equation (1)). It is also influenced by the salt concentration in the medium. In the case of BG11 the influence is limited due to the low salt concentration. The Henry coefficient for CO_2 (H_{CO2}^{cp}) was determined to 3.4×10^{-4} mol m^{-3} Pa^{-1} at 25°C (Sander, 2015). The van't Hoff equation gives the temperature dependency of the Henry coefficient (Equation (2)).

(1) $$c_{CO2} = H_{CO2}^{cp} \times p_{CO2}$$

(2) $$\frac{d(lnH)}{d(1/T)} = \frac{-\Delta H_{sol}}{R} \rightarrow H(T) = H^0 \times exp\left(\frac{-\Delta H_{sol}}{R} \times \left(\frac{1}{T} - \frac{1}{T^0}\right)\right)$$

The solubility of carbon dioxide decreases with higher temperatures. The Henry coefficient at 30°C is calculated to 2.98×10^{-4} mol m^{-3} Pa^{-1}. Carbon dioxide is part of the carbonate equilibrium (Equations (3) to (5)), it reacts with water to form carbonic acid, which is dissipating into bicarbonate rapidly, which can further react to carbonate. Both equilibrium constants (K_1 and K_2, Equations (6),(7)) were measured for water at different temperatures and salinities (Millero et al., 2006). The salinity of BG11 medium is approximately 1.7 g_{salts} $kg_{solution}^{-1}$ (Equation (8)), and all

experiments were carried out at 30°C. The corresponding equilibrium constants are 6.15 (pK_1) and 9.74 (pK_2).

(3) $$CO_2 \leftrightarrow CO_{2,aq}$$

(4) $$CO_{2,aq} + H_2O \leftrightarrow H_2CO_3 \leftrightarrow HCO_3^- + H^+$$

(5) $$HCO_3^- \leftrightarrow CO_3^{2-} + H^+$$

(6) $$K_1 = \frac{[HCO_3^-][H^+]}{[CO_{2,aq}]}$$

(7) $$K_2 = \frac{[CO_3^{2-}][H^+]}{[HCO_3^-]}$$

(8) $$S = \frac{m_{salt}}{m_{solution}} \times 1000$$

(9) $$pH = -\log[H^+]$$

At neutral pH in YBG11 medium (pH 7.2), the amount of carbonic acid is below 1% of the total dissolved inorganic carbon (DIC) and can be neglected. The soluble CO_2 concentrations at partial pressures of 0.04%, 2%, and 5% and a stable pH of 7.2 were calculated. In an insufficiently buffered system, the pH will decrease with increasing partial pressure of CO_2, which again will influence the carbonate equilibrium. The corresponding concentrations of DIC are given in Table 3-3. The DIC concentration increases from 0.15 mM at ambient conditions to 7.3 mM at 2%, and to 18.3 mM at 5% CO_2 in the surrounding atmosphere. It was shown that an increased DIC concentration is beneficial for *Synechocystis* growth.

Table 3-3: DIC in the BG11 medium at 30°C, pH 7.2, and at different partial pressures

p_{CO_2} [%]	c_{CO_2} [mM]	$c_{HCO_3^-}$ [mM]	$c_{CO_3^{2-}}$ [mM]	c_{DIC} [mM]
0.04	0.012	0.134	0.000	0.146
2.0	0.596	6.687	0.019	7.302
5.0	1.490	16.717	0.048	18.255

Data calculated based on equations (1)-(9).

Neglecting the mass transport resistance caused by the wrapped paper plug sealing the shaking flask, the mass transfer of CO_2 from the atmosphere into the aqueous phase were it enters the cells is defined by the diffusion coefficient for CO_2, the surface area of the liquid phase and the partial pressure difference of carbon dioxide in solution and in the headspace of the shaking flask. A carbon dioxide limitation occurs when the concentration of dissolved inorganic carbon

decreases to zero because the cells are taking up bicarbonate and CO_2 faster than it can be provided by the mass transfer from the gas phase. Assuming a thin layer diffusion process, the mass transfer from the gas phase can be described by Fick's first law (Equation (10)).

(10) $$J_{CO2} = k_L A \times \Delta c_{CO2}$$

The driving force for the diffusion of CO_2 into the aqueous phase is the concentration gradient that is increasing with increasing partial pressure in the gas phase. The volumetric gas transfer coefficient k_La represents the diffusion coefficient, the layer thickness and the specific interface area, which is often hard to determine. The k_La value for shaking flask experiments can, for example, be calculated from the reaction rate of a carbon dioxide limited reaction. In case of a carbon dioxide limited microbial growth, the incorporation rate of carbon into biomass should reflect the maximal CO_2 mass transfer over the gas/liquid interface.

With 0.04% CO_2 in the incubator atmosphere, the driving force given by the difference in the CO_2 partial pressure is low. Therefore, a substantial and early carbon limitation was to be expected. Exponential growth with a growth rate of 0.032±0.002 h^{-1} could be observed for 3 days up to an optical density of 2.2 (Figure 3-13, A). Afterwards, only linear growth with a rate of 0.03±0.002 h^{-1} was be measured. In comparison to the light limitation discussed in the previous paragraph, there was a difference in the slope of the exponential curve and the linear fit at the intersection. Whereas the light is directly taken up by the photosystems, the CO_2 needs to be transferred to the aqueous phase before, where a chemical equilibrium between carbon dioxide, bicarbonate, and carbonic acid is established. Therefore, dissolved inorganic carbon is "stored" in the aqueous phase. When the culture reaches a biomass concentration where more DIC is taken up than can be provided from the gas phase, there is a short phase were a higher carbon uptake is possible until the DIC amount in the aqueous phase is depleted. Afterwards, the culture grows at a lower rate, which is controlled by the maximal possible CO_2 mass transfer. Precisely this behavior can be observed in Figure 3-13, panel A, where the culture is grown with only 0.04% carbon dioxide. The exponential growth and the linear growth phase under 0.04% carbon dioxide were independent of the supplied light energy. Even at 50 µmol m^{-2} s^{-1}, the carbon limitation was dominating growth. The same is true for 100, 150, and 200 µmol m^{-2} s^{-1} (Appendix, Figure 7-2). In comparison, no carbon limitation was observed at 2% and 5% carbon dioxide.

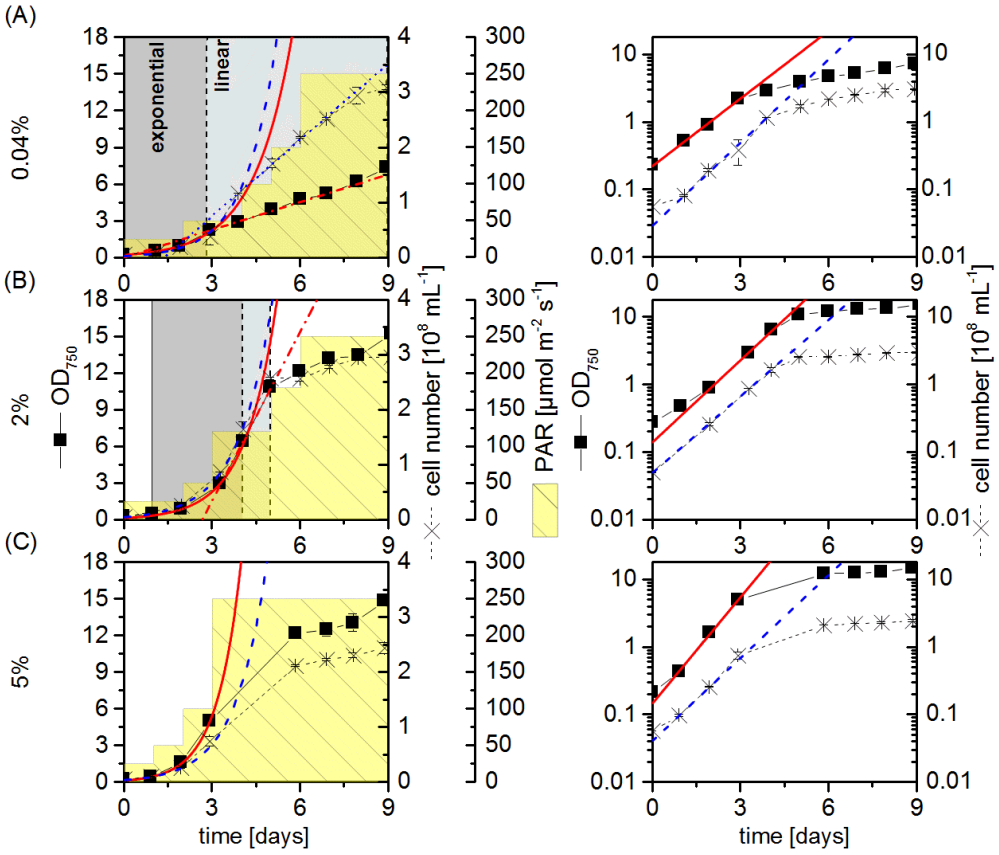

Figure 3-13: Influence of different CO_2 concentrations in the incubator on the growth of *Synechocystis* PG

Optical density and cell concentration on a linear (**left column**) and logarithmic scale (**right column**) measured during shaking flask cultivations with *Synechocystis* PG, as well as the supplied light intensity at each time point during cultivation. The light intensity was increased stepwise during cultivation from 25 to 250 µmol m^{-2} s^{-1}. Cultures were grown under different CO_2 concentrations, increasing from 0.04% to 2% and 5% from the top to the bottom row (growth rates and main data points summarized in Table 3-4).

The exponential growth rates based on OD measurements observed during the cultivations under ambient conditions, 2% and 5% CO_2 were increasing with increasing partial pressure. Surprisingly, the rate of cell division was not influenced. The optical density reflects not only particle number but also particle size, shape, density, pigmentation and surface properties and is therefore also a measure of the increase in biovolume. In this work, the optical density was measured at a wavelength of 750 nm to exclude the influence of chlorophyll and the antenna pigments. Microscopic analysis revealed that the cell shape is not altered (data not shown). Therefore, the difference in readout of the optical density measurement in comparison to the cell concentration is caused by either an increase in cell size or in an accumulation of insoluble intracellular substances that cause increased light scattering.

Table 3-4: Maximal exponential and linear growth rates determined for different CO_2 concentrations at a final light intensity of 250 µmol m^{-2} s^{-1}

CO_2 [%]	µ [h^{-1}, ±0.002]	r_L [h^{-1}, ±0.002]	$\mu_{cell\ \#}$ [h^{-1}, ±0.002]	$OD_{750,max}$ [/, ±1.0]
0.04 (ambient)	0.032	0.03	0.039	8.6
2.0	0.039	0.20	0.036	15.2
5.0	0.050	/	0.039	14.8

Data derived from Figure 3-13.

The cell size indeed increased with increasing partial pressure from 9 to 14 and finally to 21±0.6 µm^3 under 5% CO_2 (Figure 3-14). This reflects the influence of the available DIC concentration on the accumulation of storage compounds, which will be further discussed in the following section.

Influence of increasing CO_2 availability on the glycogen and propanediol production of *Synechocystis* PG

The difference in CO_2 availability is not only reflected in the growth of *Synechocystis* PG but is also influencing both glycogen and propanediol production. The glycogen content of 27.5 mM_C at 2% CO_2 decreased significantly to 9.1 mM_C at 0.04% and increased to 37.3 mM_C at 5% CO_2. Simultaneously, an increase in cell size was detected, as described above. Regarding 1,2-propanediol production, the emerging picture was not so clear. The final titer was increased by 43% from 21.2 to 30.4 mM_C (Table 3-5) when the air was enriched with 2% CO_2. Surprisingly, at 5% CO_2, only 14.3 mM_C propanediol was produced, corresponding to 2.0 mM_C d^{-1}. This was even below the values achieved with 0.04%. At 5% CO_2, the propanediol production ceased before the glycogen pool was completely consumed. For the cultures grown at 0.04% CO_2, a decline in cell concentration was observed for all light intensities (Figure 3-14, A and Appendix, Figure 7-2) as soon as the glycogen pool was depleted, which was not seen at 2 and 5% CO_2.

In conclusion, an ambient CO_2 concentration of 0.04% limited the growth and production of the biocatalyst, while a partial pressure of 5% increased the glycogen titer but did not improve productivity. A CO_2 concentration of 2% seemed to be sufficient to sustain growth and 1,2-propanediol production.

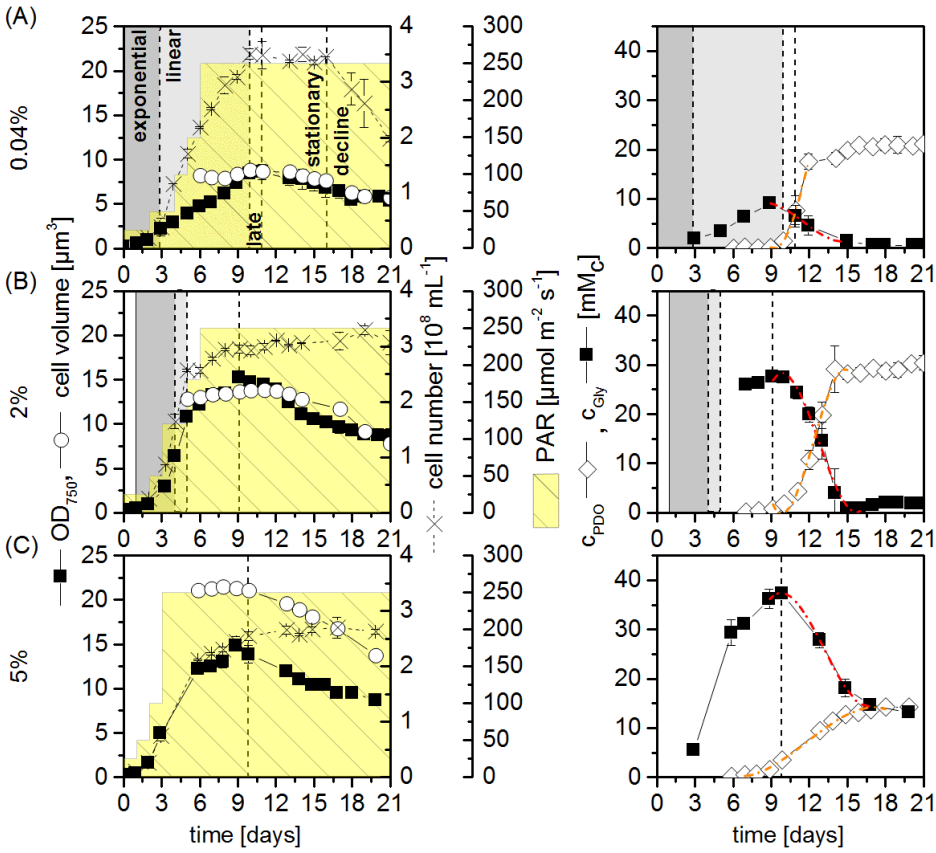

Figure 3-14: Influence of different CO_2 concentrations in the incubator on the glycogen and propanediol formation of *Synechocystis* PG

Optical density and cell concentration as well as the cell volume (**left column**, classification of growth phases see Figure 3-13) and propanediol and glycogen concentrations in mM_C (**right column**) measured during shaking flask cultivations with *Synechocystis* PG, as well as the supplied light intensity at each time point during cultivation. The light intensity was increased stepwise during cultivation from 25 to 250 µmol m^{-2} s^{-1}. Cultures were grown under different CO_2 concentrations, increasing from 0.04 to 2 and 5% from the top to the bottom row (main data points summarized in Table 3-5).

Table 3-5: Maximal Glycogen and propanediol concentrations, as well as production and turnover rates measured at different CO_2 concentrations

CO_2 [%]	$c_{PDO,max}$ [mM_C, ±0.8]	$r_{PDO,max}$ [mM_C d^{-1}, ±1.6]	$c_{Gly,max}$ [mM_C, ±1.0]	$r_{Gly,max}$ [mM_C d^{-1}, ±2.0]
0.04 (ambient)	21.2	10.6	9.1	-1.9
2.0	30.4	10.7	27.5	-7.0
5.0	14.3	2.0	37.3	-5.0

Data derived from Figure 3-14.

3.4 Impact of storage compounds glycogen and PHB in the photoautotrophic production of 1,2-propanediol with *Synechocystis* PG

In all experiments conducted so far, 1,2-propanediol production was restricted to the late growth and stationary phase. During this phase, the optical density of *Synechocystis* PG decreased significantly, while the cell number remained stable. The decrease in optical density correlates to a simultaneous decrease in cell size (e.g., Figure 3-11), which could be caused by decreasing amounts of storage compounds. If this is the case, the necessary carbon and energy for the synthesis of 1,2-propanediol may be derived either directly from the Calvin cycle or indirectly from the intracellular accumulated storage compounds PHB or glycogen. The influence of these storage compounds on the propanediol production was investigated in the following experiments.

1,2-propanediol production coincides with glycogen turn over

To elucidate the interrelation of storage compounds and 1,2-propanediol production, the intracellular glycogen and PHB pools have been monitored throughout the cultivation of *Synechocystis* PG and the wild-type strain (Figure 3-15). Both strains grew comparable to previous experiments. For this experiment, the measurement of cell numbers was replaced by the determination of the CDW because the decrease in storage compounds should be reflected in the CDW, whereas the cell number remains constant. PHB was not detected in significant amounts (< 1% of CDW), whereas the glycogen concentration increased during the linear and late growth phase and reached a maximum of 18 $mmol_C\ L^{-1}$ (~24% of CDW) in the wild type. Notably, the glycogen pool was not instantly utilized with entry into the stationary phase, which was strikingly different in the recombinant strain *Synechocystis* PG. Here, glycogen accumulated to approximately 18% of the CDW and then decreased to zero during the production phase. The decrease in biomass concentration of 0.4 $g\ L^{-1}$ during the production phase fits precisely the amount of glycogen consumed. From these findings, we conclude that the decline in biomass was due to glycogen turn-over. After the glycogen pool was depleted, no further 1,2-propanediol formation could be observed.

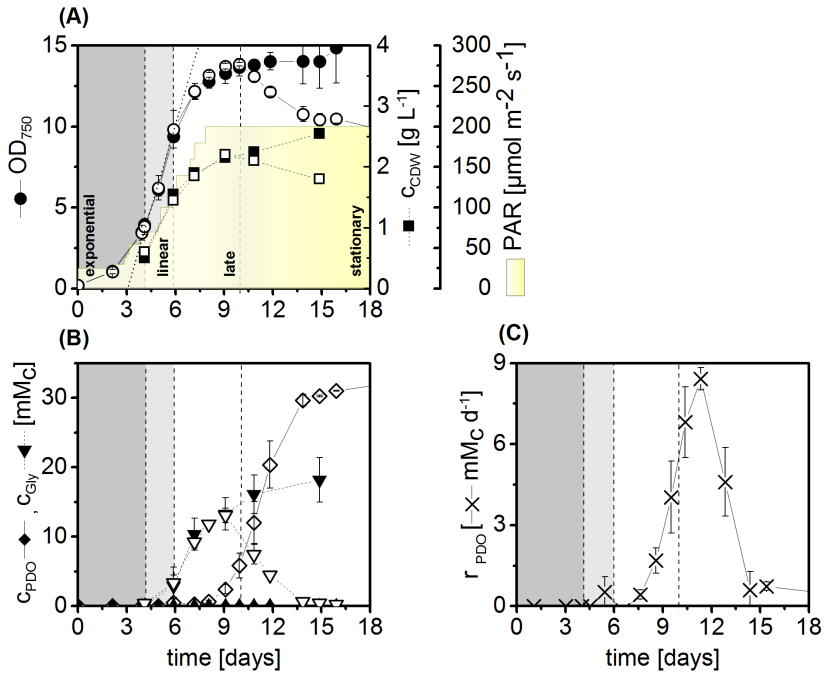

Figure 3-15: Growth and production parameters of the recombinant strain *Synechocystis* PG in comparison to the wild-type

(A) Growth and **(B)** glycogen as well as 1,2-propanediol production of *Synechocystis* PG (white symbols) in comparison to the wild type (black symbols) **(C)** Volumetric 1,2-propanediol productivity of *Synechocystis* PG over the time course of cultivation. Experiments were carried out in 250 mL baffled shaking flasks with a culture volume of 50 mL under increasing light intensity (25 – 200 µmol m^{-2} s^{-1}), 2% CO_2, 30°C, 150 rpm, and 75% humidity in an INFORS Multitron photosynthesis plus incubator. Note that the growth curves have not been corrected for the evaporation of the aqueous phase (0.2 mL day^{-1}) during the long cultivation times. With the exception of CDW, mean values and standard deviation of 4 biological replicates are shown.

Reduced 1,2-propanediol production due to impaired glycogen synthesis

To further elucidate the importance of the glycogen pool for 1,2-propanediol production, the strain *Synechocystis* Δ*glgC* PG was designed. The *glgC* deletion prevents the formation of glucose-1-phosphate adenylyl transferase and thereby, the conversion of glucose-1-phosphate to ADP-glucose. Without ADP-glucose, glycogen cannot be synthesized (Figure 1-3). The knockout strains were constructed based on the same *Synechocystis* PCC 6803 strain delivered by the Pasteur culture collection as the recombinant *Synechocystis* PG.

In addition, a *Synechocystis* sp. PCC6803 Δ*glgC* mutant kindly donated from the Hellingwerf lab (Van der Woude et al., 2014) was transformed with the genes for the 1,2-propanediol pathway. The two strains with different background were annotated with *Synechocystis*^{PCC} in case of the original strain derived from the Pasteur culture collection and with *Synechocystis*ST for the Stanford strain derived from the Hellingwerf lab. Shaking flask cultivations were performed with wild-

type *Synechocystis*^{PCC}, *Synechocystis*^{PCC} Δ*glgC* (Figure 3-16, A), *Synechocystis*^{PCC} PG, and Δ*glgC* PG (Figure 3-16, B, D) as well as with the respective Stanford strains (Figure 3-16, C, E). All four *Synechocystis*^{PCC} strains, wild-type, Δ*glgC*, PG, and Δ*glgC* PG grew comparable to an OD_{750} of 15 with minor deviations in the late growth phase. Significant differences occurred in the stationary phase.

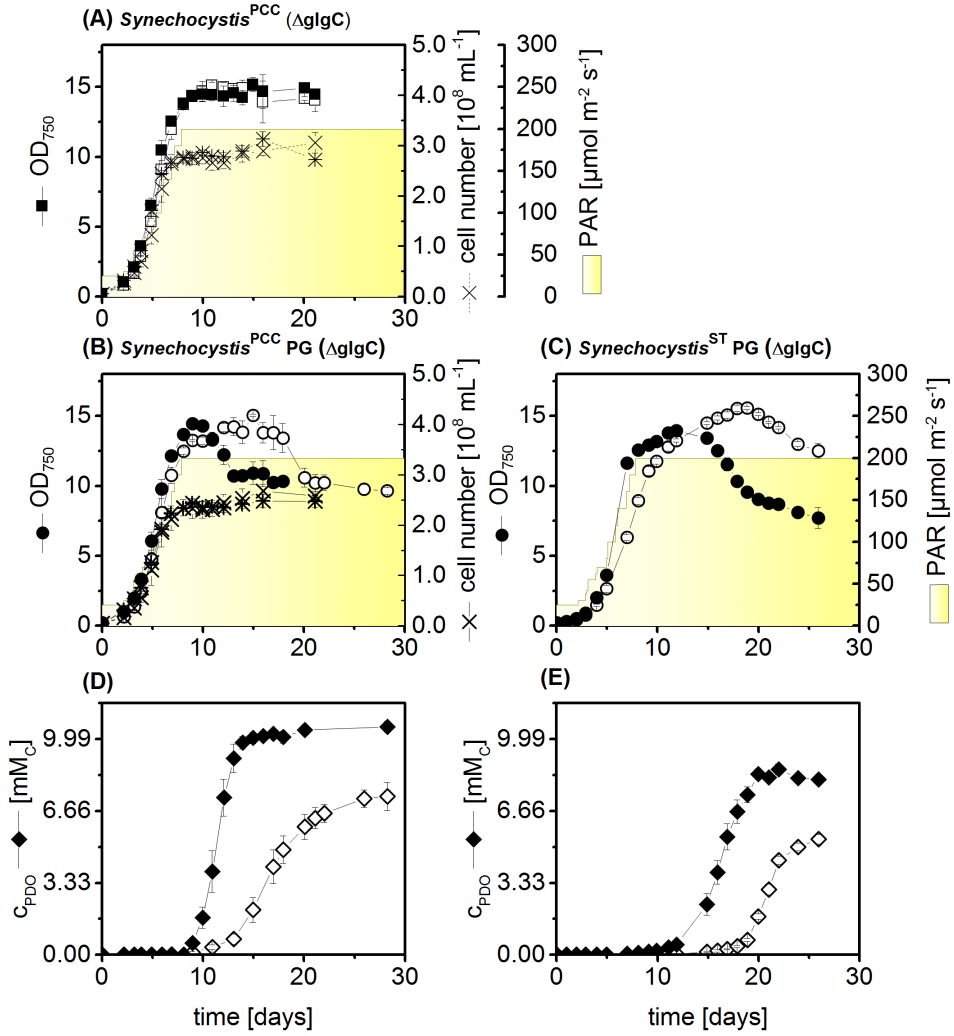

Figure 3-16: Influence of impaired glycogen synthesis (*ΔglgC*) on growth and 1,2-propanediol production of *Synechocystis* PG

Growth of *Synechocystis*^{PCC} **(A)**, *Synechocystis*^{PCC} PG **(B)**, *Synechocystis*ST PG **(C)** (black symbols) and their respective *glgC* deletions (white symbols), as well as the comparison of produced 1,2-propanediol concentrations, either with or without *glgC* deletion **(D,E).** Experiments were carried out in 250 mL baffled shaking flasks with a culture volume of 50 mL under increasing light intensity (25 – 200 µmol m^{-2} s^{-1}), 2% CO_2, 30°C, 150 rpm, and 75% humidity in an INFORS Multitron photosynthesis plus incubator. Mean values and standard deviation of 4 biological replicates are shown. Note that the growth curves have not been corrected for the evaporation of the aqueous phase (0.2 mL day^{-1}) during the long cultivation times.

While the wild-type and the Δ*glgC* strain showed a stable OD_{750} at 15 for more than 10 days, both PG and Δ*glgC* PG decreased to an OD_{750} of 10 during the stationary phase. For the PG strain, this is simultaneous with the beginning of the stationary phase as already observed in previous experiments. However, although *glgC* was apparently deleted, there were indications that glycogen was still produced, as the same decrease in the growth curve was observed during the stationary phase in case of the Δ*glgC* PG strain, which was attributed to glycogen turnover. Notably, the Δ*glgC* PG strain produced about 30% less 1,2-propanediol than the PG strain (Figure 3-16, D). In the same experiment with the respective *Synechocystis*ST strains, the Δ*glgC* PG strain grew significantly slower than the PG strain. In comparison to the experiment with the respective PCC strains, the final 1,2-propanediol titer was reduced from 26 mM_C to 16 mM_C with the Stanford strain. Nevertheless, the knockout of *glgC* had the same impact (Figure 3-16, C, E). Again, the *glgC* knockout strain produced about 38% less 1,2-propanediol. The decrease in optical density for both Δ*glgC* PG strains opens up questions regarding glycogen metabolism and segregation of mutations throughout all chromosome copies in *Synechocystis.*

	PG	Δ*glgC* PG
SynechocystisST	25.8	16.1
Synechocystis^{PCC}	31.7	22.0

Table 3-6: Maximal propanediol concentrations measured during cultivation with PG and Δ*glgC* PG strains based on *Synechocystis*^{PCC} and *Synechocystis*ST

Data derived from Figure 3-16.

1,2-propanediol is partly derived from previously accumulated glycogen

Previous experiments showed a correlation between the presence of glycogen and the production of 1,2-propanediol. This dependency is reflected in the start of propanediol production, which is correlating with the phase of glycogen degradation, as could be seen in the experiments with impaired glycogen formation. To determine the origin of the carbon flux towards the synthetic pathway, experiments with ^{13}C labeled CO_2 were conducted. Initially performed growth experiments, performed with the new setup showed no significant influence in comparison to previous shaking flask experiments (data not shown).

In the following, the shaking flasks were inoculated with *Synechocystis* PG and grown under a $^{13}CO_2$ enriched atmosphere for 8 days, up to a maximal optical density of 12 and the transition to the stationary phase. This way incorporation of almost exclusively (>98%) labeled carbon atoms into the 17.2 mM_C amounting glycogen pool could be achieved (Figure 3-17, C). In this context, only insignificant amounts of PHB (<0.2 mM_C) were measured. With the beginning of propanedi-

ol formation, the headspace of the shaking flasks was flushed with synthetic air without CO_2 for 10 min to remove most of the labeled CO_2 from the medium before the mass flow controllers were switched from labeled to unlabeled CO_2.

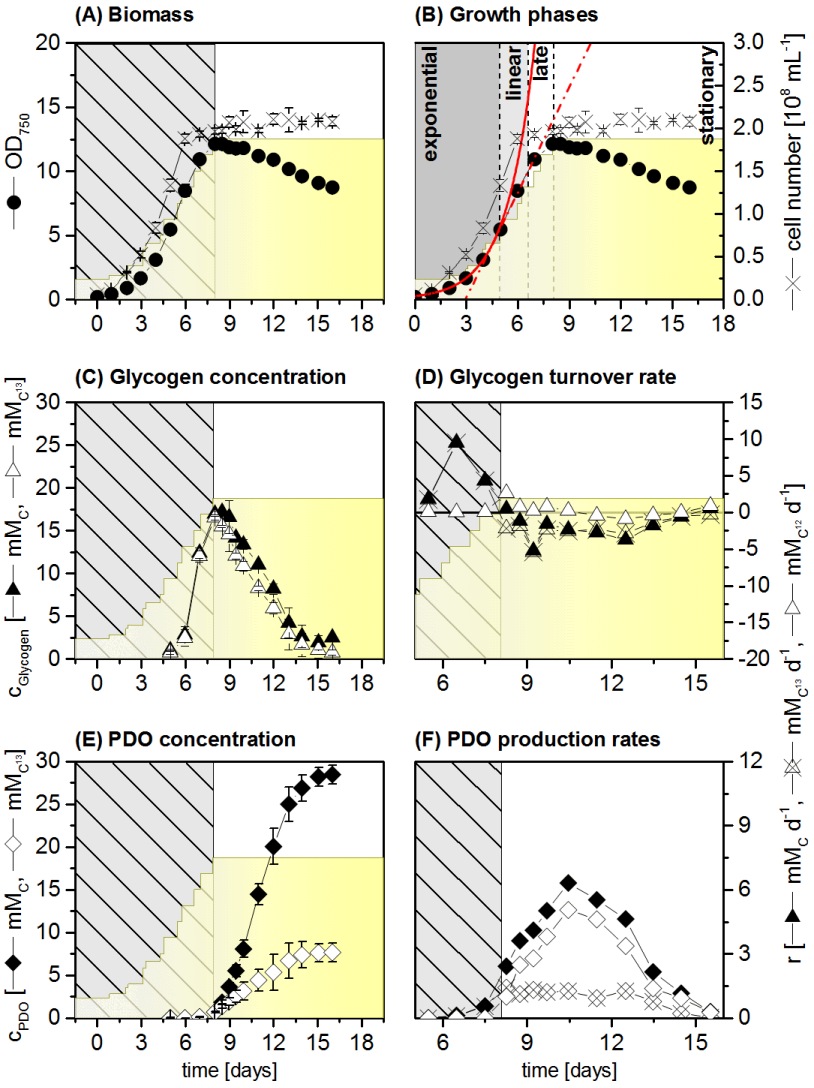

Figure 3-17: Carbon partitioning during 1,2-propanediol production of *Synechocystis* PG

Growth **(A)**, assessment of growth phases **(B)** and glycogen turn-over **(C, D)** of *Synechocystis* PG in a $^{13}CO_2$ enriched atmosphere (indicated by the gray fasciated background) followed by the production of 1,2-propanediol **(E, F)** in an atmosphere enriched with natural CO_2 (white background). Cultivation was conducted in an INFORS Minitron incubator at 30°C, 150 rpm, 2% CO_2/$^{13}CO_2$, 75% humidity, and under increasing PAR (25-200 µmol m^{-2} s^{-1}, indicated in yellow) in the growth phase, followed by subsequent constant irradiation of 200 µmol m^{-2} s^{-1} for another 10 days. Presented are the OD_{750} and cell number **(A)**, the 1,2-propanediol and glycogen concentrations in mM carbon and mM labeled carbon **(C, E)**, as well as the respective production rates for 1,2-propanediol and glycogen, again divided into overall production and production from labeled carbon atoms **(D, F)**. Important concentrations are summarized in Table 3-7.

With glycogen, PHB, and biomass as only remaining sources for labeled CO_2 and the Calvin cycle as the sole source for unlabeled CO_2, the labeling of the produced propanediol allows for the differentiation of carbon derived from the pool of storage compounds and carbon derived from photosynthetic carbon fixation.

Table 3-7: Glycogen and propanediol concentrations, as well as ^{13}C incorporation before and after the production phase

	Glycogen [mMc]		1,2-propanediol [mMc]		∑ [mMc]	
	^{12}C	^{13}C	^{12}C	^{13}C	^{12}C	^{13}C
day 8	0.5±0.0	16.5±0.3	0±0.0	0.7±0.1	0.5	17.2
day 16	1.7±0.2	0.8±0.1	20.8±0.7	7.7±0.3	22.5	8.5
Balance	+1.2	-15.7	+20.8	+7.0	+22.0	-8.7

Data derived from Figure 3-17.

At the end of the cultivation, 9.3 mM propanediol were produced, containing 28 mM_C, composed of 26% (7.5 mM) labeled and 74% (20.5 mM) unlabeled carbon atoms (Figure 3-17, E, Table 3-7). During the linear growth phase, the glycogen production rate increases up to 9.5 $mM_C\ d^{-1}$, while the consumption rate in the stationary phase was about 2.5 $mM_C\ d^{-1}$ (Figure 3-17, D, Table 3-7). During the production in the stationary phase, glycogen represented the only significantly decreasing intracellular carbon pool. Therefore, up to 26% of the carbon entering the synthetic pathway was derived from glycogen turn over. The remaining 74% were unlabeled and therefore captured by the Calvin cycle. The overall propanediol production rate was increased up to 7 $mM_C\ d^{-1}$. Thereof, the labeled carbon derived from glycogen contributes constantly 1.25 $mM_C\ d^{-1}$, whereas the unlabeled carbon contributed from the Calvin cycle increases from 1 $mM_C\ d^{-1}$ at day 8 to 5 $mM_C\ d^{-1}$ at day 10 (Figure 3-17, F). Afterward the Calvin cycle activity is decreasing and stopped entirely at day 16 when the glycogen pool was depleted. This implies that only 7.5 mM_C of the 17.2 mM_C previously stored in the glycogen pool were redirected to propanediol. The remaining 56% (9.7 mM_C) could be used for cellular maintenance or were completely oxidized to CO_2 again.

1,2-propanediol cannot be produced in the absence of an external energy source

From the conducted experiments two question arise. First, if 1,2-propanediol can be produced from glycogen alone and secondly if an energy limitation can induce glycogen degradation and thereby propanediol production. To answer these questions, the previous experiment was repeated with the following modification. With the beginning of the stationary phase, the cul-

tures were not only aerated with unlabeled CO_2 but also kept in darkness for 5 days, followed by 5 days at 200 µmol m^{-2} s^{-1} (Figure 3-18).

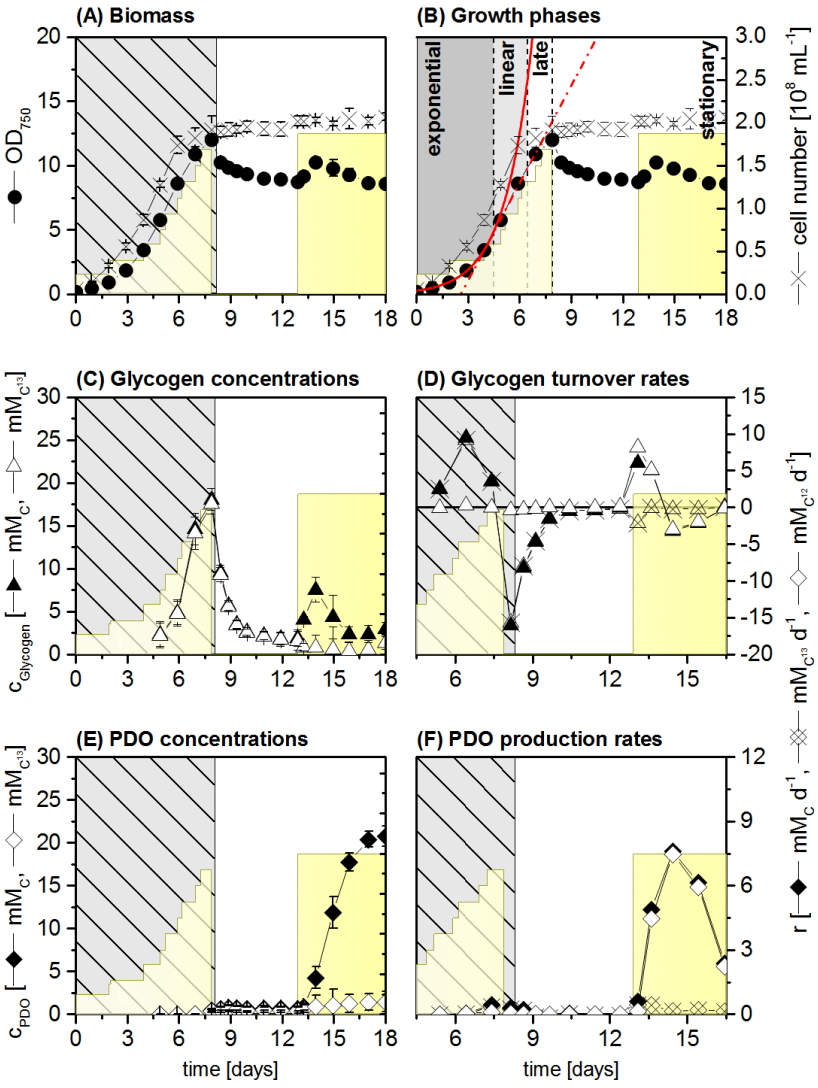

Figure 3-18: Influence of dark/light regime on carbon partitioning and productivity in Synechocystis PG

Growth **(A),** assessment of growth phases **(B)**, and glycogen turn-over **(C, D)** of the recombinant strain *Synechocystis* PG under $^{13}CO_2$ enriched atmosphere (indicated by the gray fasciated background) followed by the production of 1,2-propanediol **(E, F)** in an atmosphere enriched with natural CO_2 (white background). Cultivation was conducted in an INFORS Minitron incubator at 30°C, 150 rpm, 2% CO_2/$^{13}CO_2$, 75% humidity, and under increasing PAR (25-200 µmol m^{-2} s^{-1}, indicated by the yellow background) in the growth phase, followed by darkness for 5 days and subsequent constant irradiation of 200 µmol m^{-2} s^{-1} for another 5 days. Presented are the OD_{750} and cell number **(A)**, the 1,2-propanediol and glycogen concentrations in mM carbon and mM labeled carbon **(C, E)**, as well as the respective production rates for 1,2-propanediol and glycogen, again divided into overall production and production from labeled carbon atoms **(D, F)**. Important concentrations are summarized in Table 3-8.

During the initial growth phase under labeled CO_2, no significant differences between the cultivations could be observed, as expected. The cultures reached a maximal optical density of 12 after 8 days of growth and produced 18.1 mM_C entirely labeled glycogen with the same maximal rate of 9.5 $mM_C\ d^{-1}$. Notably, without light as an external energy source in the stationary phase, no 1,2-propanediol was formed. Nevertheless, glycogen degradation occurred with a three times faster rate (16.0 $mM_C\ d^{-1}$) compared to the same situation with active irradiation. Within 2 days only 2.5 mM_C glycogen remained. After 5 days in darkness, when light was provided again, the glycogen pool increased from initially 1.9 to 7.5 mM_C again. Only after glycogen accumulated again, propanediol production was observed (day 13, Figure 3-18, D, F). In the following, 20.7 mM_C almost unlabeled (< 5%) 1,2-propanediol were produced from the newly assembled unlabeled glycogen and CO_2.

Table 3-8: Glycogen and propanediol concentrations, as well as ^{13}C incorporation after the growth phase, after cultivation in darkness, and before and after the production phase

	Glycogen [mMc]		1,2-propanediol [mMc]		∑ [mMc]	
	^{12}C	^{13}C	^{12}C	^{13}C	^{12}C	^{13}C
day 8	0.5±0.0	17.6±1.2	0.1±0.0	0.4±0.1	0.6	18.0
day 13	0.3±0.2	1.6±0.8	0.2±0.1	0.5±0.2	0.5	2.1
day 14	6.7±1.3	0.8±0.2	3.4±1.0	0.9±0.3	10.1	1.7
day 18	1.7±0.5	1.3±0.3	19.3±1.1	1.5±0.1	21.0	2.8
Balance	+1.2	-16.3	+19.2	+1.1	+20.4	-15.2

Data derived from Figure 3-18.

On day 14, glycogen synthesis with 5.1 $mM_C\ d^{-1}$ and 1,2-propanediol production with 4.9 $mM_C\ d^{-1}$ were running simultaneously, which is in sum close to the 9.5 $mM_C\ d^{-1}$ that could be observed as maximal glycogen formation rate on day 7 when cell division already ceased. With the product formation and glycogen accumulation taking place simultaneously and the now unlabeled glycogen pool, no prediction of the carbon flux through the glycogen pool into the product was possible. However, it became evident that both glycogen and external light energy are crucial for propanediol production.

3.5 Establishing photoautotrophic 1,2-propanediol production on the 2-3 L scale

As discussed already in the introduction (chapter 1.3.3), different reactor setups have been developed for the unique requirements of photoautotrophic biocatalysts. For the here conducted initial experiments, stirred-tank-photo-bioreactors (STPBR) and flatpanel-airlift-photobioreactors (FPBR) were used, and their efficiency regarding 1,2-propanediol production was compared (Figure 3-19).

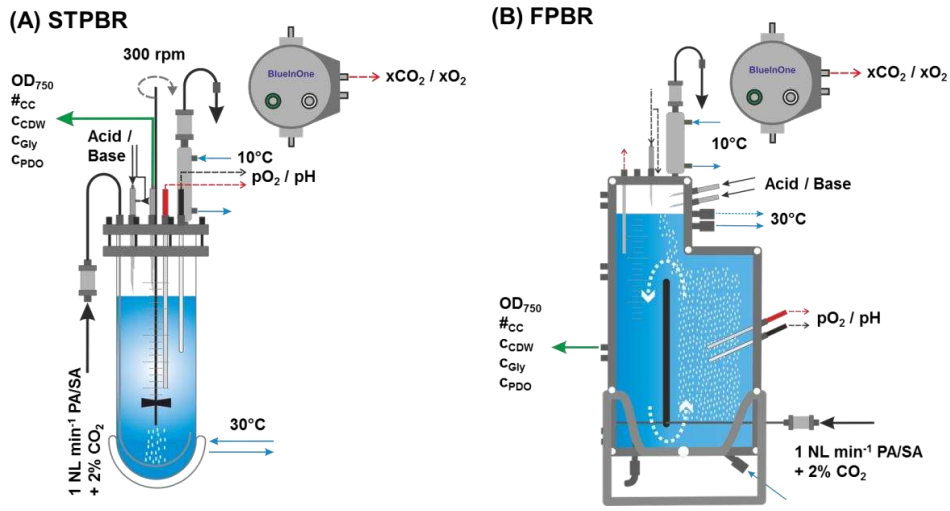

Figure 3-19: Stirred tank photobioreactor (STPBR) and flat-panel airlift photobioreactor (FPBR)

3 L stirred tank photobioreactor (STPBR, INFORS Labfors 5 LUX) (**A**) and 2 L flatpanel airlift photobioreactor (FPBR, INFORS Labfors 5 LUX) with 20 mm wide culture vessel (**B**), both equipped with Hamilton pO_2 and pH probes and BlueSens BlueInOne off-gas analytics for the measurement of the CO_2 and O_2 concentrations. Aeration with either pressurized air (PA) or synthetic air (SA) enriched with 2% CO_2 and controlled by respective thermal mass flow controllers (red-y, Vögtlin instruments). A controllable LED panel provides illumination.

First, the process was transferred to a 3 L benchtop stirred tank photobioreactor (STPBR) equipped with a small heating jacket (Figure 3-19, A) and surrounded by a cylindrical jacket of white light LEDs supplying light. Mixing was realized with a propeller stirrer set to 300 rpm to prevent excessive shear forces. The *Synechocystis* PG preculture was grown in shaking flasks as described before and used at an OD of 6 to inoculate 2 L YBG11 to a starting OD of 0.2. The reactor was aerated at 1vvm with 2% carbon dioxide-enriched air. The pH was not actively controlled and increased from 7.2 to 7.4 during the cultivation. This is in accordance with the pH increase detected during shaking flask cultivation (data not shown).

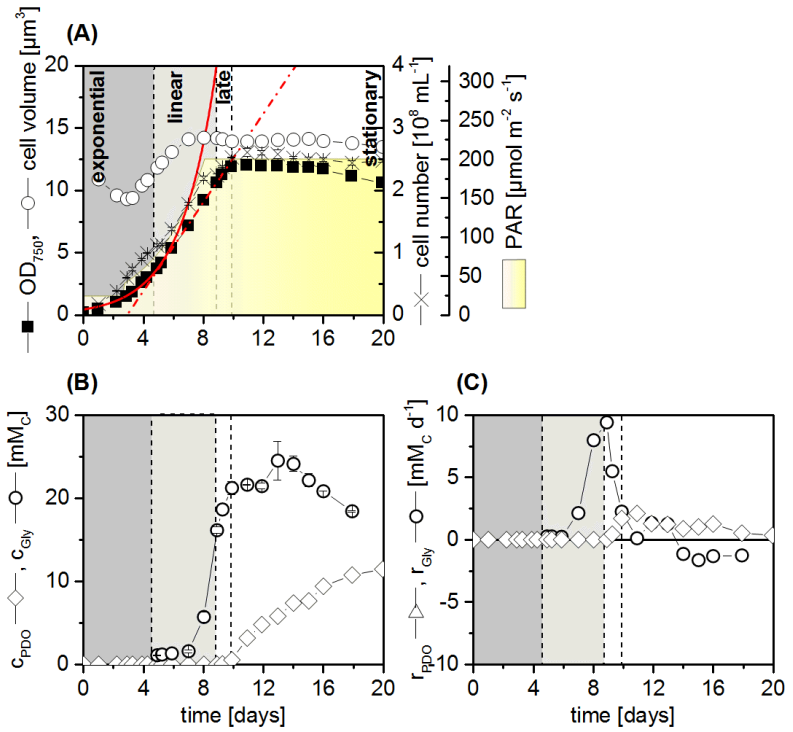

Figure 3-20: Growth, glycogen, and 1,2-propanediol production of *Synechocystis* PG in a STPBR

Growth of *Synechocystis* PG, classification into growth phases (**A**) as well as 1,2-propanediol and glycogen concentrations (**B**). In addition, the corresponding rates were calculated (**C**). Cultivation in a 3L INFORS Labfors 5 LUX stirred tank photobioreactor in 2L YBG11 (pH 7.2, 50 mM HEPES) at 30°C, 1 vvm enriched with 2% CO_2, and under increasing PAR (25-200 µmol m^{-2} s^{-1}, see Panel (**A**)). Presented are the OD_{750}, cell number, and the cellular volume of the cultures (**A**), 1,2-propanediol and glycogen concentrations in mM_C (**B**), and finally the corresponding rates in mM_C d^{-1} (**C**).

During the first 5 days, the cells grew exponentially with a growth rate of 0.018±0.001 h^{-1} to an optical density of 5. Afterwards, a light-limited linear growth phase with a rate of 0.074±0.002 h^{-1} could be observed for additional 4 days. After in total 10 days, the maximal optical density of 12 and the maximal cell concentration of 2.6x10^8 mL^{-1} was reached and the culture entered the stationary phase (Figure 3-20, A). A maximal glycogen concentration of 21.5 mM_C was achieved. In comparison to the experiments in shaking flasks, the achieved glycogen concentration was almost 25% higher. Surprisingly, the glycogen was not utilized for propanediol production. A significant turnover of the glycogen pool in the stationary phase was not observed. Nevertheless, 1,2-propanediol was produced with a rate of maximal 2.0 mM_C d^{-1}. The final titer was 11.5 mM_C (Figure 3-20 (B, C)). The rate and the titer were three times lower in comparison to the experiments in shaking flasks.

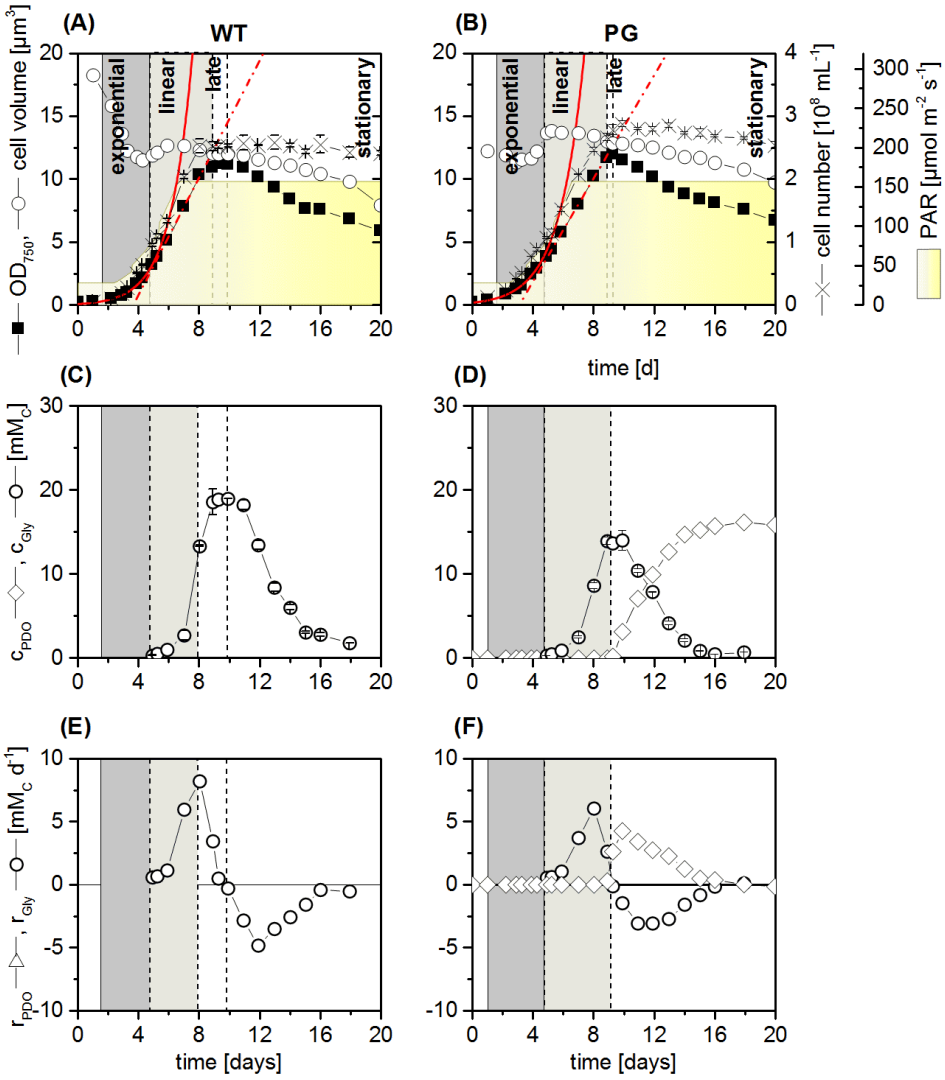

Figure 3-21: Growth, glycogen, and 1,2-propanediol production of *Synechocystis* PG and wild-type in a FPBR

Growth of *Synechocystis* wild-type (**A**) and recombinant PG strain (**B**), as well as 1,2-propanediol and glycogen concentrations (**C**, **D**). In addition, the corresponding rates were calculated (**E**, **F**). Cultivation in two 2 L INFORS Labfors 5 LUX flatpanel airlift photobioreactors in YBG11 (pH 7.2, 50 mM HEPES) at 30°C, 0.5 vvm enriched with 2% CO_2, and under increasing PAR (25-150 µmol m^{-2} s^{-1}, see Panel (**A**)). Presented are the OD_{750}, cell number, and the cellular volume of the cultures (**A**, **B**), 1,2-propanediol and glycogen concentrations in mM_C (**C**, **D**), and finally the corresponding rates in mM_C d^{-1} (**E**, **F**).

Afterwards, two benchtop flatpanel airlift photobioreactors equipped with LED panels were inoculated, one with *Synechocystis* wild type, one with *Synechocystis* PG. Cells were grown in a batch cultivation under increasing light intensity (25-150 µmol m^{-2} s^{-1}) to an optical density of 11.2 for the wild-type and 12.0 for the PG strain. In the stationary phase, the PAR was kept con-

stant at 150 µmol m^{-2} s^{-1} (Figure 3-21, A, B). Due to technical limitations at that time point the PAR could not be increased further to 200 µmol m^{-2} s^{-1}.

At the end of the growth phase, a cell concentration of 2.6x10^8 mL^{-1} was measured for the wild-type and 2.9x10^8 mL^{-1} for the recombinant strain, respectively. Exponential growth rates of 0.029 and 0.026 h^{-1} for the wild-type and the recombinant strain were measured. The increase in optical density during the linear growth phase was 0.10 and 0.09 h^{-1}, respectively (Table 3-9). The difference of the linear growth rate in comparison to the shaking flasks, where a linear growth rate of 0.18 h^{-1} was measured could be due to the exponential stepless increase in light intensity instead of the stepwise increasing light intensity in the flask incubators.

Table 3-9: Maximal exponential and linear growth rates, as well as maximal cell concentration and optical density during initial FPBR cultivation of *Synechocystis* WT and PG

Synechocystis strain	µ [h^{-1}, ±0.001]	r_L [h^{-1}, ±0.003]	$c_{cell\ \#}$ [10^8 ml^{-1}, ±0.1]	$OD_{750,max}$ [/]
WT	0.029	0.10	2.58	11.2
PG	0.026	0.09	2.88	12.0

Data derived from Figure 3-21.

Both strains produced glycogen during the linear and late growth phase. The maximal concentration in the wild-type was 35% higher in comparison to the PG strain, with 19 to 14 mM_C, respectively (Table 3-10). Afterward, the glycogen was degraded in both cultures. This represents a significant difference to the observations made in shaking flasks. Here, the glycogen concentration in the wild-type culture remained stable for 3 days. During this time the glycogen in the recombinant PG strain was completely consumed. During the 6 days of glycogen consumption in the FPBR, the PG strain produced 16.2 mM_C propanediol with a maximal rate of 4.3 mM_C d^{-1}, which is approximately 75% of the propanediol concentration reached in shaking flask under comparable light conditions (21 mM_C). The accumulated glycogen concentration at the transition from the growth to the stationary phase was not influenced by the lower light intensity of 150 µmol m^{-2} s^{-1}. The wild-type and the PG strain produced glycogen amounts that were comparable to what was observed in the shaking flask experiments. However, the final light intensity in the bioreactor was 50 µmol m^{-2} s^{-1} lower as in the respective shaking flask cultivations, which might have influenced the propanediol production in the stationary phase. The growth curves of the bioreactor cultivations are comparable to the ones measured in shaking flasks, only the lag phase was longer in the FPBR's (Figure 3-21, A, B).

Table 3-10: Maximal Glycogen and propanediol concentrations, as well as production and turnover rates measured during FPBR cultivation of *Synechocystis* WT and PG

Synechocystis strain	$c_{PDO,max}$ [mM_C, ±0.8]	$r_{PDO,max}$ [$mM_C\ d^{-1}$, ±1.6]	$c_{Gly,max}$ [mM_C, ±1.5]	$r_{Gly,max}$ [$mM_C\ d^{-1}$, ±3.0]
WT	/	/	19.0	-4.8
PG	16.2	4.3	14.0	-3.1

Data derived from Figure 3-21.

The cultivation of both *Synechocystis* strains could be transferred to the 2-3 L scale in benchtop bioreactors. Due to the improved provision of light in the FPBRs and the better comparability to the shaking flask experiments, further bioreactor cultivations were carried out in FPBRs. CO_2 uptake and O_2 evolution could not be quantified due to variations in the composition of the pressurized air (PA) during these experiments. For a carbon balance and reliable oxygen evolution measurements, synthetic air with a constant composition and without CO_2 is essential.

Closing the carbon balance for *Synechocystis* wild-type and PG

The previous experiment was repeated with synthetic air (SA) enriched with 2% CO_2. Synthetic air does not contain carbon dioxide and is therefore suited for precise balancing of carbon in the bioreactor. Additionally, the oxygen evolution of the culture can be quantified as a measure for the activity of the water-splitting reaction. The light intensity was increased up to 250 µmol $m^{-2}\ s^{-1}$ in this experiment. The growth phases were influenced by the increased availability of light (Figure 3-22, A, B). The exponential growth phase was prolonged by 1.5 days up to an optical density of more than 5, whereas the optical density achieved previously was below 4.

Table 3-11: Maximal exponential and linear growth rates, as well as maximal cell concentration and optical density during FPBR cultivation of *Synechocystis* WT and PG

Synechocystis strain	µ [h^{-1}, ±0.001]	r_L [h^{-1}, ±0.002]	$c_{cell\ \#}$ [$10^8\ ml^{-1}$, ±0.1]	$OD_{750,max}$ [/]
WT	0.026	0.12	2.71	12.1
PG	0.025	0.12	3.25	12.0

Data derived from Figure 3-22.

The exponential growth rates of 0.026 h^{-1} for the wild-type and 0.025 h^{-1} for the PG strain were comparable to the growth rates observed in the previous reactor runs (Table 3-11), whereas the linear growth rates were increased from 0.09 in the previous runs to 0.12 h^{-1} for both strains due

to the increased PAR. A late growth phase as it was observed in previous experiments with shaking flasks could not be observed.

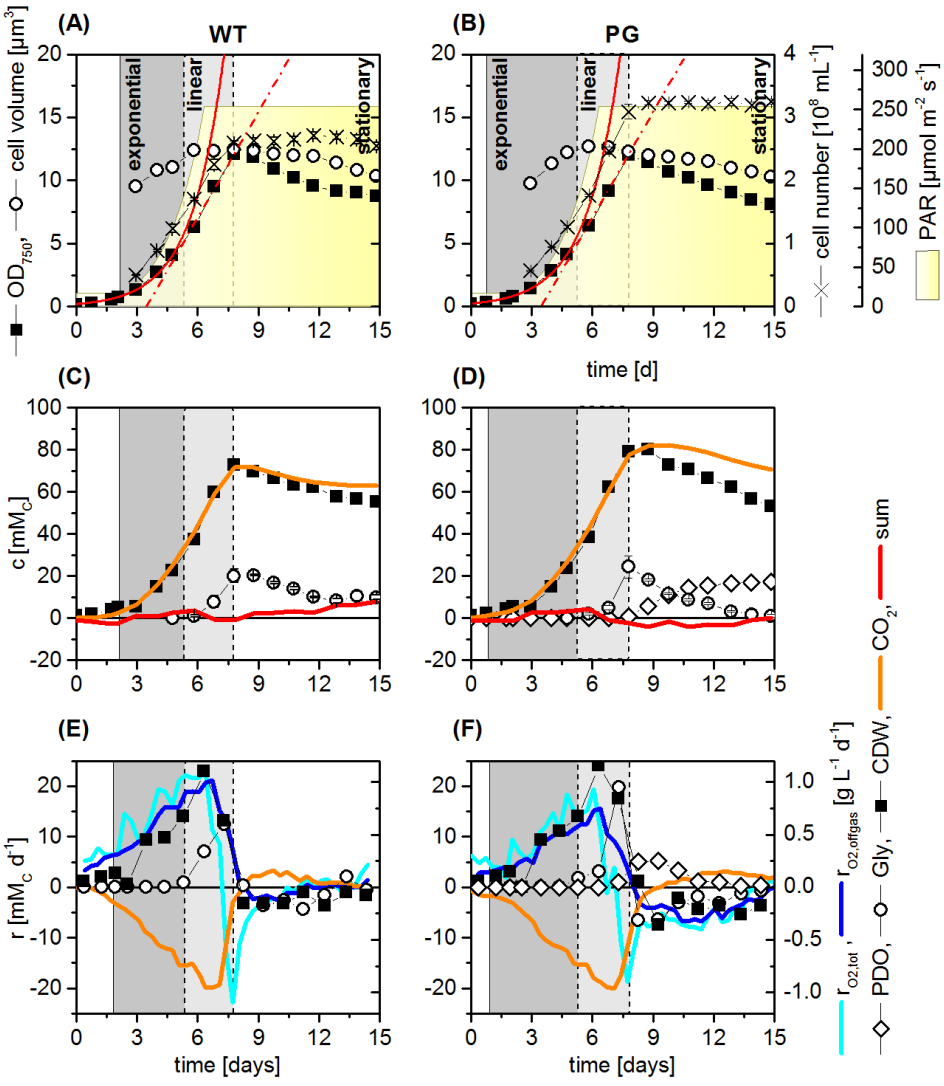

Figure 3-22: Carbon uptake during batch experiments in flat panel airlift bioreactors with *Synechocystis* PG in comparison to the wild-type strain

Growth of *Synechocystis* wild-type (**A**) and recombinant PG strain (**B**), as well as the carbon concentration taken up by the bioreactors in comparison to the accumulated amounts of carbon in the biomass, in 1,2-propanediol, and in the glycogen pool (**C**, **D**). In addition, the corresponding rates and the oxygen evolution were calculated (**E**, **F**). Cultivation in two 2L INFORS Labfors 5 LUX flatpanel airlift photobioreactors in YBG11 (pH 7.2, 50 mM HEPES) at 30°C, 0.5 vvm enriched with 2% CO_2, and under increasing PAR (25-250 µmol m^{-2} s^{-1}, see Panel (**A**)). Presented are the OD_{750}, cell number, and the cellular volume of the cultures (**A**,**B**), the absorbed carbon, biomass, 1,2-propanediol, and glycogen concentrations in mM_C (**C**,**D**), and finally the corresponding rates in mM_C d^{-1}, as well as the oxygen evolution in g L^{-1} d^{-1} (**E**,**F**).

In addition to the OD_{750} and the cell number, also the carbon content accumulated in the biomass was determined. Therefore, cell dry weight measurements were conducted. For the calculation of mM_C contained in the biomass, an overall carbon content of 51.4% was assumed (Shastri and Morgan, 2005). However, the elemental biomass composition is depending on growth conditions. For example, glycogen contains 40% carbon, whereas PHB contains 55%, and proteins have a carbon content of approximately 47%. If the amount and distribution of intracellular storage compounds changes, the carbon content of the biomass will be influenced as well. Measurements of the carbon content of *Synechocystis* biomass grown under various light intensities and CO_2 concentrations resulted in an average carbon content of 49±2% (Marcel Grund, personal communication), which is in good accordance to literature.

Table 3-12: Carbon concentrations stored in biomass, glycogen, and propanediol in comparison to the amount of carbon taken up by the bioreactor at the beginning (day 8) and the end of the production phase (day 15)

strain	day	CO_2 [mM_C]	Biomass [mM_C]	Glycogen [mM_C]	Propanediol [mM_C]	sum [mM_C, %]
WT	8	-71.7	72.7	(20.0)	0.0	1.0 (1.4%)
PG	8	-77.8	79.1	(24.4)	0.9	2.2 (2.8%)
WT	15	-62.8	55.1	(9.8)	0.0	-7.7 (12.3%)
PG	15	-70.6	53.1	(1.1)	17.4	-0.1 (0.1%)

Data derived from Figure 3-22. Glycogen (in brackets) is part of the biomass and is therefore not considered for the overall carbon balance.

The wild-type biomass increased to 72 mM_C (1.70±0.05 g L^{-1}) during the growth phase and declined afterward to 55 mM_C (1.29±0.05 g L^{-1}, Table 3-12). Part of the biomass is the storage compound glycogen which increased to 20 mM_C (0.60±0.05 g L^{-1}) during the linear growth phase and afterwards decreased to 10 mM_C (0.29±0.05 g L^{-1}) after 5 days of stationary phase. The decrease in CDW of 0.41±0.05 g L^{-1} is partly explained by the simultaneous turnover of 0.31 g L^{-1} glycogen. At the end of the cultivation, the glycogen concentration remained stable at 10 mM_C.

In comparison to the wild-type, the carbon content in the PG strains biomass increased to 80 mM_C (1.85±0.05 g L^{-1}) and decreased to 53 mM_C (1.24±0.05 g L^{-1}) again. The maximal glycogen concentration reached 24 mM_C (0.73±0.05 g L^{-1}), which were completely consumed at the end of the cultivation (Table 3-12). The PG strain loses 0.61±0.05 g L^{-1} CDW, while it is catabolizing 0.70 g L^{-1} glycogen. While utilizing glycogen, the recombinant strain secreted 17.4 mM_C propanediol.

The overall carbon uptake of the bioreactor was determined by in- and off-gas analytics. Overall, the general carbon recovery rate is satisfying for the *Synechocystis* PG cultivation (Table 3-12), whereas for the wild-type strain 7.7 mM_C are missing after the stationary phase. Most probably the wild-type strain produces additional fermentation products that were not identified.

After 8 days of growth, the highest CO_2 uptake of the bioreactor was reached with 71.7 mM_C for the wild-type and 77.8 mM_C for the PG strain respectively (Table 3-12). During the following stationary phase, CO_2 was released from the reactor leading to a decreased overall carbon uptake of 62.8 and 70.6 mM_C at the end of the experiment.

Table 3-13: Maximal Glycogen and propanediol concentrations, as well as production and turnover rates measured during FPBR cultivation of *Synechocystis* WT and PG

Synechocystis strain	$c_{PDO,max}$ [mM_C, ±0.8]	$r_{PDO,max}$ [$mM_C\ d^{-1}$, ±1.6]	$c_{Gly,max}$ [mM_C, ±3]	$r_{Gly,max}$ [$mM_C\ d^{-1}$, ±3.0]
WT	/	/	20.4	-4.3
PG	17.4	5.2	24.4	-6.5

Data derived from Figure 3-22.

The oxygen evolution rate (Figure 3-22, E, F) increased with increasing biomass and PAR. The peak evolution rates of 1000 mg $L^{-1}\ d^{-1}$ for the wild-type and 750 mg $L^{-1}\ d^{-1}$ for the PG strain were measured after 6.4 and 6.7 days, respectively, when the maximal light intensity was reached.

In conclusion, a carbon balance for the recombinant strain *Synechocystis* PG could be established, whereas for the wild-type strain an additional unknown carbon sink could not be identified. However, the 1,2-propanediol titers during the bioreactor experiments remained lower than in shaking flask cultivations.

Continuous production of 1,2-propanediol in bioreactor scale

In all previous experiments, 1,2-propanediol production was restricted to the late and stationary growth phase and limited to a production window of maximal 6 days. Thereby also the maximally achievable propanediol titer is limited, despite the reasonable production rates. To improve the final 1,2-propanediol titer, it is necessary to either stabilize the 1,2-propanediol production, so that it can be produced continuously or to produce 1,2-propanediol repeatedly in a kind of fed-batch process. In this process, glycogen would be alternatingly produced and consumed to produce 1,2-propanediol repeatedly and thereby increase the final product titer. Therefore, possible strategies for the continuous production of 1,2-propanediol were evaluated in the following

experiments, starting with continuous cultivation of *Synechocystis* PG in a FPBR. There are two major strategies to control a continuous bioreactor process, the turbidostat and the chemostat cultivation. In a turbidostat, the turbidity as a measure for the biomass concentration is analyzed and the feed is controlled to keep the biomass concentration constant. The FPBR setup applied in this study allows the measurement of the incident light intensity and the light intensity passed through the cultivation vessel. The PAR that passed through the culture can be used to keep the biomass concentration constant by altering the feed rate. However, for this application, a high biomass concentration is desired, in order to maximize propanediol production rates. At high biomass concentrations and irradiations that do not cause stress to the cells, there is no light passing through the culture anymore. Therefore at high cell densities, there is no online measured parameter available to control the biomass concentration. In any case, previous experiments showed that limited growth and a phosphate limitation are beneficial for glycerol and 1,2-propanediol production. Also, phosphate is the limiting nutrient in BG11 medium. Therefore, if a constant flow rate is applied, the biomass concentration is controlled by the phosphate concentration in the feed solution, as long as the dilution rate is below the maximal possible growth rate under these conditions. The resulting chemostat should allow propanediol production while controlling growth via phosphate availability. The *Synechocystis* PG culture was grown exponentially with a growth rate of 0.031±0.001 h^{-1} to an optical density of approximately 3, followed by a linear growth phase with a growth rate of 0.084±0.001 to an OD_{750} of 8. At this optical density, initial experiments with turbidostat cultivation in the linear growth phase at a high dilution rate and with cultivation under dark conditions were performed.

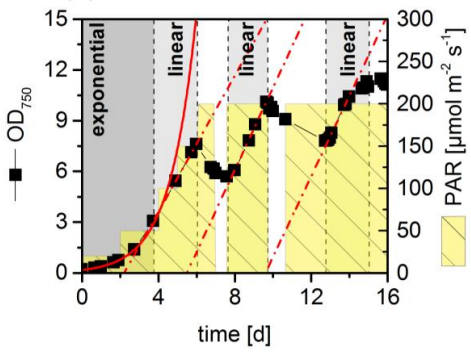

Figure 3-23: Initial growth of *Synechocystis* PG in a FPBR

OD_{750}, growth phases, and light intensity during cultivation in a 1.8 L INFORS Labfors 5 LUX flatpanel airlift photobioreactor in YBG11 (pH 7.2, 50 mM HEPES) at 30°C, 0.5 vvm enriched with 2% CO_2, and under increasing PAR (25-200 µmol m^{-2} s^{-1}).

Neither did the strain produce propanediol when continuously kept in the linear growth phase, nor did a dark phase without growth induce propanediol formation (data not shown). However, the optical density decreased, and the cells were grown to an optical density of approximately

10 were the same tests were repeated (Figure 3-23). Again, no propanediol formation could be observed (data not shown). However, propanediol formation was observed when the cells were grown to an OD of 12.3±0.2 and kept at the early transition from the linear to the late growth phase. Therefore, the dilution rate was set constant to 0.01 h^{-1} (0.32 mL min^{-1} / 1.8 L reactor volume), and growth was limited by nutrient allocation in the medium. At this point with a residence time of almost 4 days, a constant propanediol concentration of 1.07±0.05 mM_C was measured (Figure 3-24, C) with a rate of 0.27±0.01 mM_C d^{-1}. Also, the glycogen concentration was stable at 11.6±0.2 mM_C. As a consequence, glycogen was produced with a rate of 3.0±0.1 mM_C d^{-1}. The overall biomass formation rate was 18.5±0.3 mM_C d^{-1}, which in addition to the 1.07 mM_C d^{-1} propanediol produced is close to the overall carbon uptake of approximately 20.0±0.5 mM_C d^{-1}.

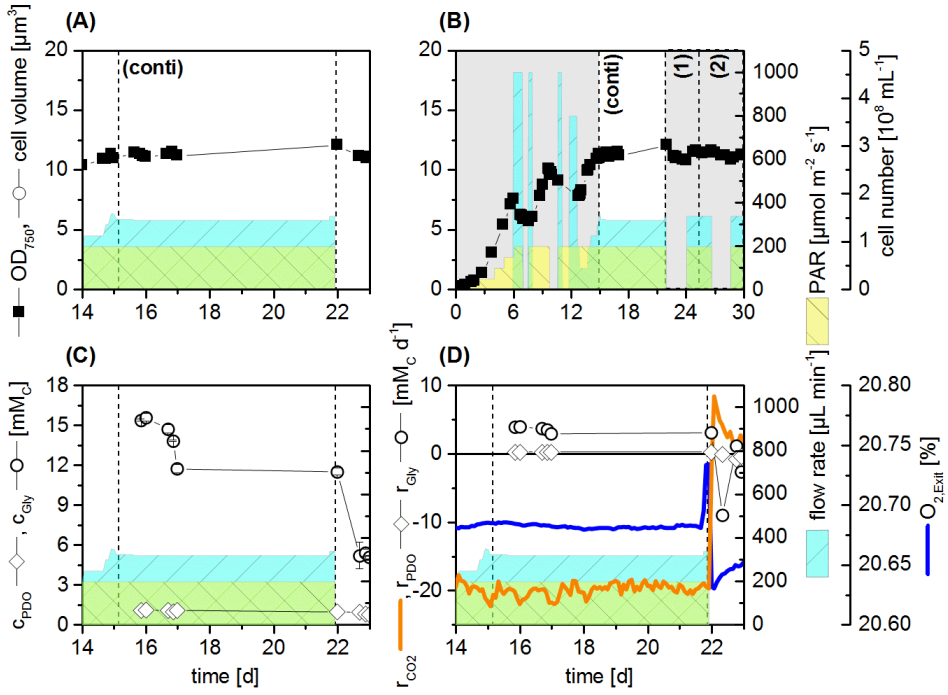

Figure 3-24: Continuous cultivation of *Synechocystis* PG in a FPBR

(**A**) Biomass, (**B**) glycogen, and 1,2-propanediol production, (**D**) CO_2 uptake and O_2 evolution during continuous cultivation of *Synechocystis* PG. (**B**) Overview showing the complete cultivation process, with the continuous cultivation phase indicated by the white background. Cultivation in a 1.8L INFORS Labfors 5 LUX flatpanel airlift photobioreactor under a dilution rate of 0.01 h^{-1} with YBG11 (pH 7.2, 50 mM HEPES) at 30°C, 0.5 vvm enriched with 2% CO_2, and under continuous illumination with 200 µmol m^{-2} s^{-1}

Propanediol could be successfully produced in a continuous setup, but with a low titer and production rate. The glycogen was not entirely consumed anymore but was constantly released

from the reactor, which is not beneficial for 1,2-propanediol production. For time reasons, the influence of different dilution rates on the glycogen utilization and propanediol production could not be investigated anymore. Nevertheless, an even lower dilution rate might increase glycogen utilization and 1,2-propanediol production, while preventing excessive biomass formation. This could be one of the starting points for further investigations.

Propanediol production under dark oxic and anoxic conditions

Previous experiments conducted in shaking flasks proved that propanediol production under standard cultivation conditions depends on the availability of light (Chapter 3.4). Recent studies with different recombinant *Synechocystis* based production strains showed the formation of fermentation products under dark conditions in the absence of oxygen (Hasunuma et al., 2016; Kusakabe et al., 2013).

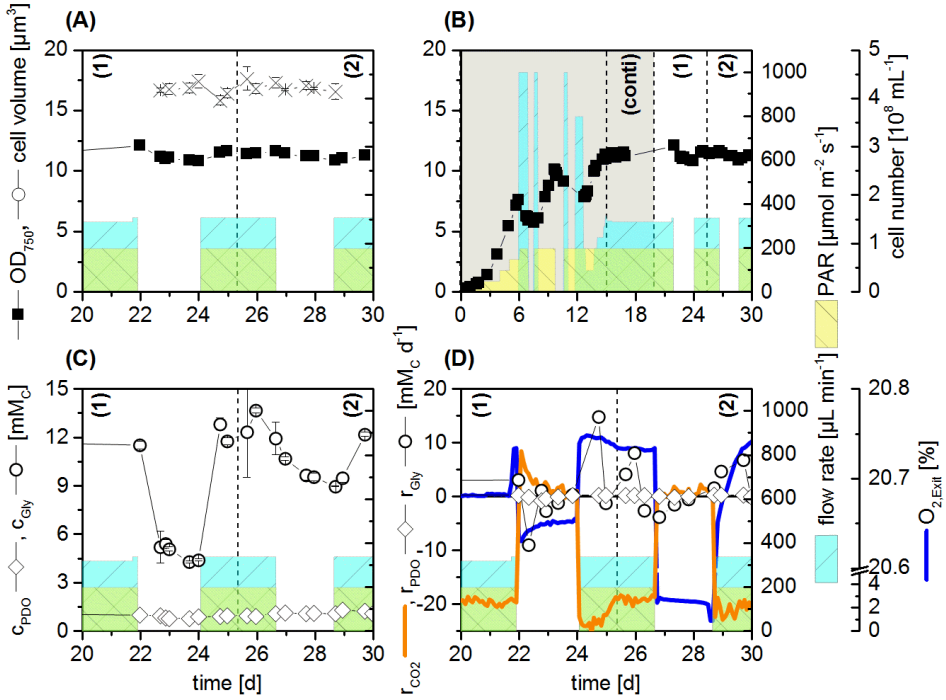

Figure 3-25: Cultivation of *Synechocystis* PG under dark oxic (1) and dark anoxic (2) conditions

(**A**) Biomass, (**B**) glycogen, and 1,2-propanediol production, (**D**) CO_2 uptake and O_2 evolution during cultivation of *Synechocystis* PG under dark and dark anoxic conditions. (**B**) Overview showing the complete cultivation process, with the dark oxic (1) and dark anoxic (2) cultivation phase indicated by the white background. Cultivation in a 1.8L INFORS Labfors 5 LUX flatpanel airlift photobioreactor in YBG11 (pH 7.2, 50 mM HEPES) at 30°C, 0.5 vvm air or nitrogen, enriched with 2% CO_2, and under continuous illumination with 200 µmol m^{-2} s^{-1}

A study concerning the metabolome during dark anaerobic cultivations revealed increased intracellular metabolite concentrations of DHAP (Hasunuma et al., 2016), which is the precursor for the propanediol pathway. To investigate the influence of dark anoxic conditions on the 1,2-propanediol formation, *Synechocystis* PG was grown continuously in a FPBR as described in the previous section. Then the culture was cultivated for 2 days under dark oxic conditions (Figure 3-25 (1)) and after an illuminated recovery phase under dark anoxic conditions (Figure 3-25 (2)). During these times, no dilution of the culture took place. With the transfer to dark conditions, the glycogen concentration declined by 60% from 11.5 to 4.5 mM_C within 16 hours (Figure 3-25 (C,1)). The remaining 4.5 mM_C were not degraded any further during the dark period. As expected from the experiments in shaking flasks, this decrease in glycogen was not accompanied by propanediol formation. Instead, the glycogen was almost completely oxidized to CO_2. During the dark period, 4.5 mM carbon dioxide were released, the rate mirroring the glycogen consumption rate. Due to the absence of light, oxygen evolution could not be observed. Instead, oxygen was consumed due to the glycogen oxidation. After 48 hours, illumination (200 µmol m^{-2} s^{-1}) and dilution were re-established. Within 12 h, the initial glycogen pool of 11.5 mM_C was restored. This was again reflected in the carbon uptake rate, which was initially higher. Later on, the carbon uptake stabilized at the same rate observed initially during the continuous cultivation. In addition, the increased energy demand was mirrored by an enhanced oxygen evolution between days 24 to 25 (Figure 3-25 (D,1)).

When the continuous culture stabilized again, the next condition was tested. In addition to cultivation under dark conditions, this time the aeration of the bioreactor was switched from synthetic air to nitrogen. Without oxygen evolution, the culture quickly became anaerobic (Figure 3-25 (D,2)). In contrast to the previous condition in the presence of oxygen, this time the glycogen was utilized slower with a maximal rate of approximately 3.8 in comparison to 8.9 mM_C d^{-1} under dark conditions only. Nevertheless, no propanediol formation could be observed. Instead an accumulation of 1.25 mM_C acetate was detected (data not shown). Acetate formation under dark anoxic conditions was already previously observed (Angermayr et al., 2016b). It was assumed that the degradation of glycogen to acetate is covering the maintenance needs during the dark period. Here, we measured accumulation of 1.25 mM_C, while the glycogen pool decreased by 3.0 mM_C. Additional fermentation products were not detected.

Finally, despite the reported changes in metabolome and proteome during dark anoxic cultivation, propanediol production could not be induced.

3.6 Cyanobacterial biofilm characterization

In all experiments conducted so far, most of the activated carbon was used for biomass formation. The same is true for nearly all heterologous chemicals produced with cyanobacteria up to now, including bioethanol production (Figure 1-3, and Table 1-1). The yield of 1,2-propanediol from carbon dioxide ($Y_{P/S}$) is only 0.25 $mol_C\ mol_C^{-1}$, whereas the yield of biomass from CO_2 ($Y_{X/S}$) is about 0.75 $mol_C\ mol_C^{-1}$. For 1 g of product, more than 2 g of biomass were produced. High cell densities of active biocatalysts are necessary to improve the volumetric production rate. This catalyst has to be regenerated and maintained. However, a continuously increasing amount of biocatalyst may not directly improve photoautotrophic fermentation processes. Instead, excessive biomass formation can lead to the fast depletion of nutrients and, more important, to light and or CO_2 limitation, leading to non-optimal production conditions. Therefore, a high biomass concentration is difficult to achieve in planktonically growing photoautotrophic cultures. The amount of catalyst applied is a tradeoff between volumetric production rate and process conditions. As long as the carbon flow cannot controlled and shifted from biomass to product formation, the production rates and titer will remain limited. Therefore, a strategy where growth can be controlled needs to be applied, were the biocatalyst is retained, and were the capacity for carbon fixation can be used for biocatalysis. One approach to achieve this is the cultivation of the whole cell biocatalyst as a self-immobilized and self-sustained biofilm. Cyanobacteria can be found in nature as part of a microbial mat, a multilayer, multispecies biofilm. Here, they live in symbiosis with different microorganisms. Studies regarding the biofilm formation of monoseptic cyanobacterial cultures are limited (chapter 1.3.4).

Robust biofilm formation with *Synechocystis* sp. PCC 6803

As part of this study, the capability of the two cyanobacterial model strains *Synechocystis* and S*ynechococcus* for biofilm formation was investigated. Therefore, both strains were grown in a glass capillary flow-through reactor system (Figure 2-2, Materials and Methods, Chapter 2.5). Initial cell attachment and subsequent biofilm growth were visualized by confocal laser scanning microscopy (CLSM), based on the autofluorescence of chlorophyll A, phycocyanin, and carotenoids (Materials & Methods, Chapter 2.14). Under the conditions applied, *Synechococcus* did not attach to the glass substratum. A reason why cell attachment and biofilm formation with this strain was not possible may be a mechanism for self-suppression of biofilm formation induced by

a self- produced extracellular compound, as reported recently (Schatz et al., 2013). In contrast to that, initial cell attachment of *Synechocystis* to the glass surface of the flow cell reactor took place within 4 h. Since *Synechocystis* showed strong biofilm formation, biofilm growth and morphology were characterized under different hydrodynamic conditions.

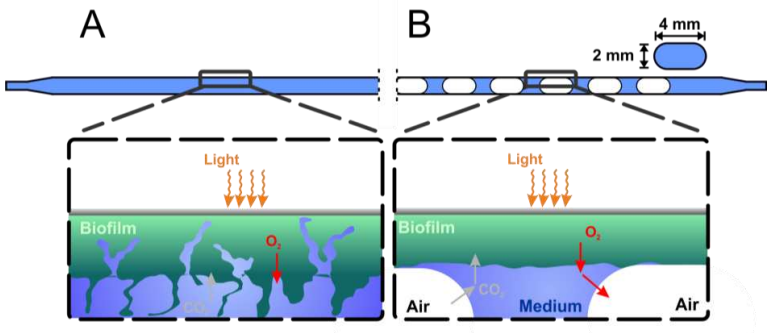

Figure 3-26: Glass capillary flow-through reactor system under single phase and segmented flow

Schematic representation of the glass capillary flow-through reactor system (capillary length 80 mm) operated in single-phase flow (A) and segmented flow mode (B). Light is absorbed and scattered on its way through the individual biofilm layers, whereas CO_2 is consumed by the cells resulting in a CO_2 gradient. O_2 produced by photosynthesis is leaving the system via the bulk phase.

Uncontrolled heterogeneous single species biofilm formation under single phase flow

No-flow, batch incubation in the tube allowed sufficient initial cell attachment overnight. Then, at an applied flow rate of 50 µL min^{-1} (0.7 cm min^{-1}), exponential growth was observed during the first 72 h of the experiment at a growth rate of 0.045 h^{-1}, calculated based on the increase in overall biofilm volume. A gradient in biofilm thickness towards a thinner film at the outflow was observed over the reactor length. Most probably this was due to carbon dioxide depletion at this low flow rate. *Synechocystis* formed a very heterogeneous patchy biofilm under these conditions, with a porous structure interconnected by channels and elongated streamers. Overall, this resulted in a high surface ratio of 5.5 μm^2 μm^{-2}, and an inhomogeneous thickness and light distribution (Figure 3-29 (A), Figure 3-26, (A) and Figure 3-27 (B, single phase)). After 7 days, the flow rate was increased to 100 µL min^{-1} (1.4 cm min^{-1}), preventing CO_2 limitation. To exclude an influence of the carbon dioxide limitation at the beginning of the experiment on the overall development of the biofilm structure, the experiment was repeated with an initial flux of 100 µL min^{-1} (1.4 cm min^{-1}). The same heterogeneous biofilm structure described before was observed. After 14 days of constant flow, the capillary started to clog and as a result the system pressure

loss increased, and a constant flow could not be maintained anymore. At this time point the biofilm was in large parts still permeable to light (Figure 3-27 (B, single phase, day 11), but could not be supplied with CO_2 any longer. During the cultivation loss of filamentous biofilm parts due to sloughing events could be observed (Figure 3-27 (C, single phase)).

Segmented flow shapes and stabilizes single species biofilm development

The capillary plug flow reactor was inoculated with *Synechocystis*. The system was left idle overnight for initial cell attachment followed by 2 days of single-phase flow (100 µL min^{-1}, 1.4 cm min^{-1}). Afterwards, air segments were introduced as described in the method section (50 $µL_{air}$ min^{-1} / 50 $µL_{medium}$ min^{-1}, 1.4 cm min^{-1}).

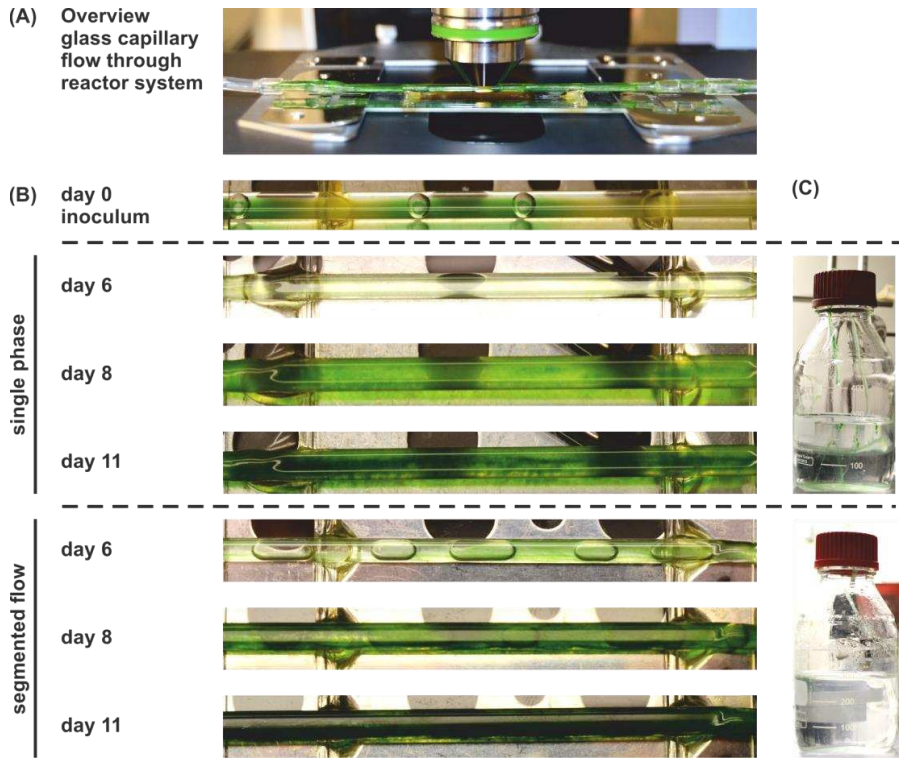

Figure 3-27: Cultivation of *Synechocystis* in a glass capillary flow-through reactor system

(A) Overview showing the glass capillary flow-through reactor system placed under the CLSM (B) *Synechocystis* biofilm development under single phase and segmented flow and the respective collected flow through (C).

In addition to the frictional forces caused by the moving liquid phase, additional forces were generated by the moving interphase separating medium and air. The surface tension of water, which allows the water skimmer to walk on water, effects cell attachment and shapes the biofilm structure. Typically, the water surface is flat with a minimized surface area. In this case, however, the surface is bent, because the adhesion of the water molecules to the glass surface of the capillary is stronger than the cohesion between individual water molecules. While passing a moving interphase, shear and surface tension forces act on small solid particles (< 500 µm)(Aramrak et al., 2011). A schematic representation of the acting forces in such a segmented flow system is presented in Figure 3-28.

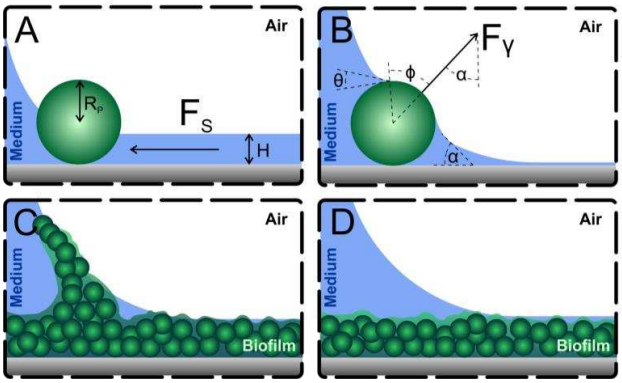

Figure 3-28: Forces acting on single cells and biofilm structures under segmented flow

(A) Shear force generated through the liquid film between glass surface and air bubble under segmented flow (B) Surface tension (interfacial) force generated by the moving air water interphase. Filamentous (C) and thin compact (D) biofilm structures under segmented flow.

In comparison to these, the gravity and buoyancy forces become negligible (Aramrak et al., 2011). Shear and surface tension forces have been intensively studied while investigating and applying the "Lotus Effect" for dust removal in industrial applications (Quan et al., 2016). The shear force F_S and the surface tension force F_γ can be calculated by equations (11) and (12), where µ is the dynamic viscosity of the liquid, γ is the surface tension, H is the film thickness between air and glass substratum (Figure 3-28 (A)), D_H the hydraulic diameter, R_P the particle radius, ϕ and θ are the filling angle and the contact angle (Figure 3-28 (B)), and v is the overall flow velocity.

(11) $$F_S = 1.7(6\pi)\mu_v\left(\frac{H}{2}\right)v$$ (Aramrak et al., 2011)

(12) $$F_\gamma = 2\pi R_p \gamma sin\phi sin(\theta - \phi)$$ (Aramrak et al., 2011)

(13) $$\frac{\mathrm{H}}{D_H} = 0.643\left(\frac{3\mu_v v}{\gamma}\right)^{0.67}$$ (Bretherton, 1961)

(14) $$F_d = 6\pi_v \mu R_P v$$ (Stokes law)

Table 3-14: Parameters for the calculation of shear and interfacial forces

Parameter			
radius of the particle	R_P	1.25 – 2	µm
surface tension of water	γ	0.072	N m^{-1}
dynamic viscosity of water	μ_v	8,01E-04	Pa s
water film thickness	H	0.9	µm
flow velocity	v	14	mm min^{-1}
hydraulic diameter	D_H	2.78	mm
filling angle and contact angle	$sin\phi sin(\theta - \phi)$	0.1 - 1	

This theory was transferred from solid particles with a diameter of 0.5 to 1 µm to bacterial cells (Boks et al., 2008; Karande et al., 2014) to estimat forces generated by passing air-liquid interfaces on single cells attached to a substratum and biofilm structures. Karande and coworkers estimated the shear and interfacial forces on the biofilm and compared it to attachment forces published for different cell types and biofilms. Whereas up to now published cell attachment forces of bacteria to a glass surface are in the range of 10^{-12} N (pN), biofilm attachment forces can be in the range of pN and higher (Boks et al., 2008).

According to the work of Karande et al. (Karande et al., 2014), the forces acting on a *Synechocystis* biofilm were calculated. The used parameters are given in Table 3-14. A water film thickness between glass capillary and air bubbles of 0.9 µm was estimated based on equation (13). With a cell diameter in between 2.5 to 4 µm, only the lower third of single cells attached to the glass substratum are subject to shear forces during the passage of air segments, whereas the rest is subject to interfacial forces. The air segments generated shear forces of approximately 2 pN, but interfacial forces between 0.15 and 1.5 µN. The frictional forces under laminar single phase flow can be calculated to approximately 10 pN by Stokes law (Equation (14)). Overall, the interfacial forces generated by segmented flow are orders of magnitude higher than the frictional forces acting on the biofilm under single-phase flow. Surprisingly, the interfacial forces did not result in significant detachment processes as observed for *Pseudomonas* under segmented flow

(Karande et al., 2014). In fact, no wash out of cells could be detected throughout the experiment. The attachment forces of the cells to the substratum are possibly much higher for *Synechocystis* compared to the heterotrophic *Pseudomonas* strain reported earlier. There, the interfacial forces generated by the segmented type of flow were strong enough to detach all cells from their growth surface almost completely. Cell attachment forces are depending on cell surface properties, EPS composition and excretion, and on the surrounding biofilm structure. With sufficient surface coverage and EPS production, the cells are not easily accessible to interfacial forces anymore (Figure 3-28, D).

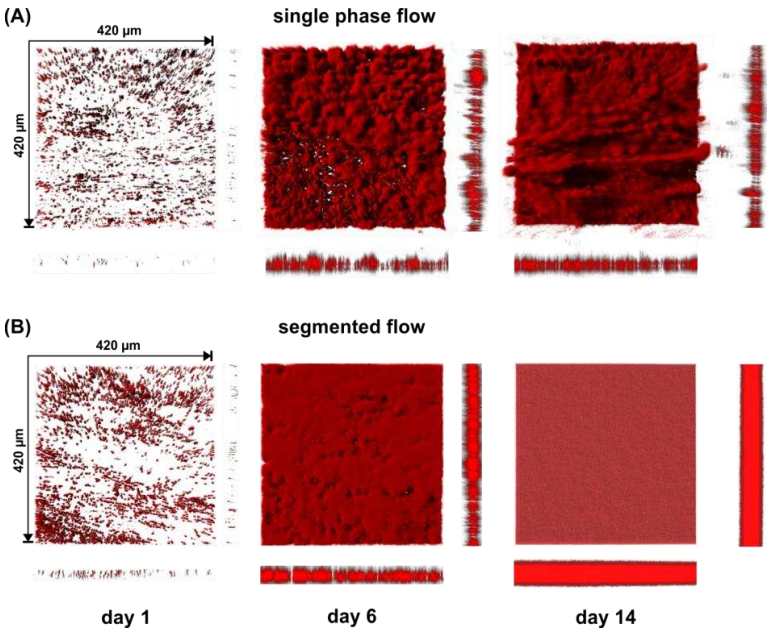

Figure 3-29: 3D reconstruction of CLSM pictures taken during *Synechocystis* biofilm development

Representative images showing the differences in development of *Synechocystis* biofilms grown under single-phase flow (A) and segmented flow (B). The illustrations are 3D-reconstructions of the biofilm generated from CLSM data by IMARIS. The top views on the biofilm surface, as well as cross sections of the biofilm, are included. The first pictures were taken directly after starting the flow. In the case of segmented flow, the biofilm thickness at day 6 and 14 exceeded already the penetration capacity of the applied LSM technique

During the first 72 h of this experiment, a growth rate of 0.045 h^{-1} was determined for *Synechocystis*, which is comparable to the growth rates without segmented flow described above. However, segmented flow changed the biofilm structure dramatically. If the CO_2 availability had any impact regarding the change in biofilm structure remains to be elucidated. There are no indications for a CO_2 limitation in either system (single (100 µL min^{-1})/ two-phase flow), as for both

equal biofilm thicknesses from the beginning to the end of the plug flow reactor were determined, pointing toward a sufficient supply of this substrate. During the first 14 days of the experiment, a homogenous, dense biofilm layer developed (Figure 3-29, B). The autofluorescence intensity, used for quantification of biomass development, is significantly higher compared to the biofilm grown under single-phase flow. The signal intensity determined from the biofilm was depending on cell density and pigment concentration within the cells. Especially the latter is subject to changes due to adaptation to different light conditions and is influenced by laser irradiation of the CLSM. Nevertheless, this signal may be used for a qualitative assessment of the biofilm biomass. At some point of growth, the biofilm thickness and the density of the mature biofilm grown under segmented flow exceeded the penetration capacity of the CLSM system, and the biofilm thickness could no longer be determined (Figure 3-29, B, days 6 and 14). However, it was possible to characterize the further development of the biofilm by eye (Figure 3-27, B, segmented flow). Within 2 weeks, the biofilm grown in the capillary appeared nearly black. In contrast to the non-segmented aqueous microreactor described above, the biofilm reactor could be continuously operated for 5 weeks further before it was actively terminated. There was neither an indication that the biomass increased further during this period, nor were any cells detectable in the flow through. The cultivation in segmented flow capillary biofilm reactors can achieve controlled biofilm growth and can even prevent excess biomass formation, which keeps the process controllable.

Key parameters affecting *Synechocystis* biofilm development

Critical parameters for biocatalytic and biotechnological applications of cyanobacterial biofilms are the distribution of light and the diffusional limitations of carbon dioxide and oxygen within the biofilm. In the case of heterotrophic biofilms, the efficient supply of nutrients is a matter of diffusion, in most cases directly from the aqueous bulk phase. In contrast, light availability, essential for the growth of phototrophic biofilms, is determined via light absorption and scattering within the biofilm.

The light attenuation caused by absorption can be calculated by Lambert-Beers law (Equation (15)), where I is the light intensity inside the biofilm at the position z, α_x is the biomass specific light absorption coefficient, and c_x the biomass concentration. Equitation (15) can be integrated within I_0 to I and 0 to z to obtain equation (16), where I_0 is the initial incident light intensity.

(15) $$\frac{dI}{dz} = -\alpha_x c_x I$$ (Lambert-Beers law)

(16) $$\mathrm{I} = I_0 e^{(\alpha_x c_x z)}$$

(17) $$\mathrm{I} = I_0 e^{(\alpha_x c_x c_I z)}$$ (Blanken et al., 2016)

(18) $$\mathrm{I} = I_0 e^{(K_0 z)}$$

The assumption that the specific absorption coefficient is constant allows the correlation of cell dry weight and cell concentration to the optical density and is the basis for optical density based growth curves. However, the optical density for *Synechocystis* cultures is typically measured at either 730 or 750 nm. High wavelengths are necessary to exclude absorption of light by chlorophyll a and the phycobilisome. That would influence the optical density with changing concentrations of photopigments, which is the case if the overall light attenuation inside a phototrophic biofilm is to be calculated. In addition, the linear correlation is only given for cultures diluted to a low optical density. At higher optical densities, as inside a biofilm, light scattering has to be taken into account. Scattering of light mainly extends the distance the light has to travel through the biofilm, which increases the probability that the light is absorbed (Klok et al., 2013). Therefore, equation (16) has to be modified to account for light scattering as well. This can be realized by introducing an additional correction factor c_I (Equation (17))(Blanken et al., 2016). The biomass specific light absorption coefficient, the biomass concentration and the correction factor can be combined to an overall light attenuation coefficient K_0 (Equation (18)). K_0 can be obtained from experimental data. However, it has to be mentioned that both light scattering and absorption are wavelength dependent and that therefore attenuation of light of different wavelengths will not be the same. In general, light scattering is increasing with decreasing wavelength.

In natural phototrophic-heterotrophic mixed species biofilm communities, the spatial distribution of photo- and heterotrophic organisms, the attenuation of light intensity and the photosynthesis rate within these microbial mats have been intensively investigated (Al-Najjar et al., 2012; Fenchel and Kühl, 2000; Kühl et al., 1996; Kühl and Fenchel, 2000). Depending on the densities of the investigated mats and the organisms contained specific light attenuation coefficients were

reported, which gave a basis for estimating respective values for the here cultivated *Synechocystis* biofilms (Figure 3-30, A). Related to the observed structure of the biofilm growing in the

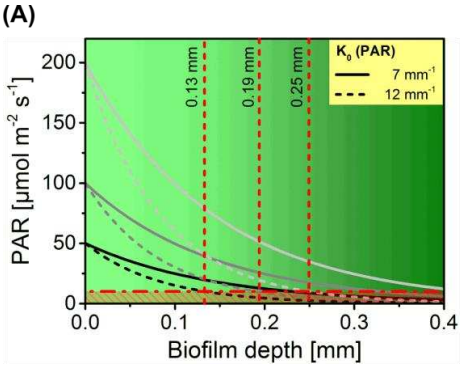

Figure 3-30: Light scattering and mass transport within the biofilm

(A) Theoretical exponential light attenuation within a cyanobacterial biofilm calculated from data published for an artificial cyanobacterial mat. Light attenuation coefficients between 7 and 12 mm^{-1} were estimated for a loose and dense biofilm, respectively. The horizontal line represents the boundary of 10 µmol m^{-2} s^{-1} where growth of *Synechocystis* is significantly decreased.

(B) Schematic distribution of the main substrate carbon dioxide, the produced oxygen, and the photosynthetically active radiation (PAR) within the biofilm.

microcapillaries, light attenuation coefficients between 7 and 12 mm^{-1} were estimated. The light attenuation coefficient together with the intensity of the available incident light defines the borders of growth in three-dimensional structures as biofilms. For the cyanobacterium *Oscillatoria agardhii* these limits have been closely evaluated. Below 20 µmol m^{-2} s^{-1}, a significant decrease in the growth rate was observed, while above 150 µE m^{-2} s^{-1} light inhibition occurred (Tilzer, 1987). In the case of *Synechocystis,* growth was significantly decreased at PAR below 10 µmol m^{-2} s^{-1} (data not shown). Based on these values, a maximal thickness for *Synechocystis* biofilms cultivated under the previously described conditions has been calculated (Figure 3-30, A). Assuming a maximal possible light intensity of 200 µE m^{-2} s^{-1} and a light attenuation coefficient of 7 mm^{-1}, which can be assumed for a loose biofilm, a maximal biofilm thickness of 400 µm can be theoretically achieved. For a biofilm grown under single-phase flow conditions ($K_0 \approx 9$ mm^{-1}), a maximal biofilm thickness of 300 µm can be theoretically achieved. The light attenuation coefficient under segmented flow is significantly higher because of higher cell densi-

ties within the biofilm. The maximal biofilm thickness to be expected for a dense biofilm under segmented flow ($K_0 \approx 12\ mm^{-1}$) is 250 µm. The expected thickness under the experimental conditions applied here (50 µE m^{-2} s^{-1}, segmented flow) was 130 µm (Figure 3-30, A), which is far beyond the detection limit of the available CLSM system.

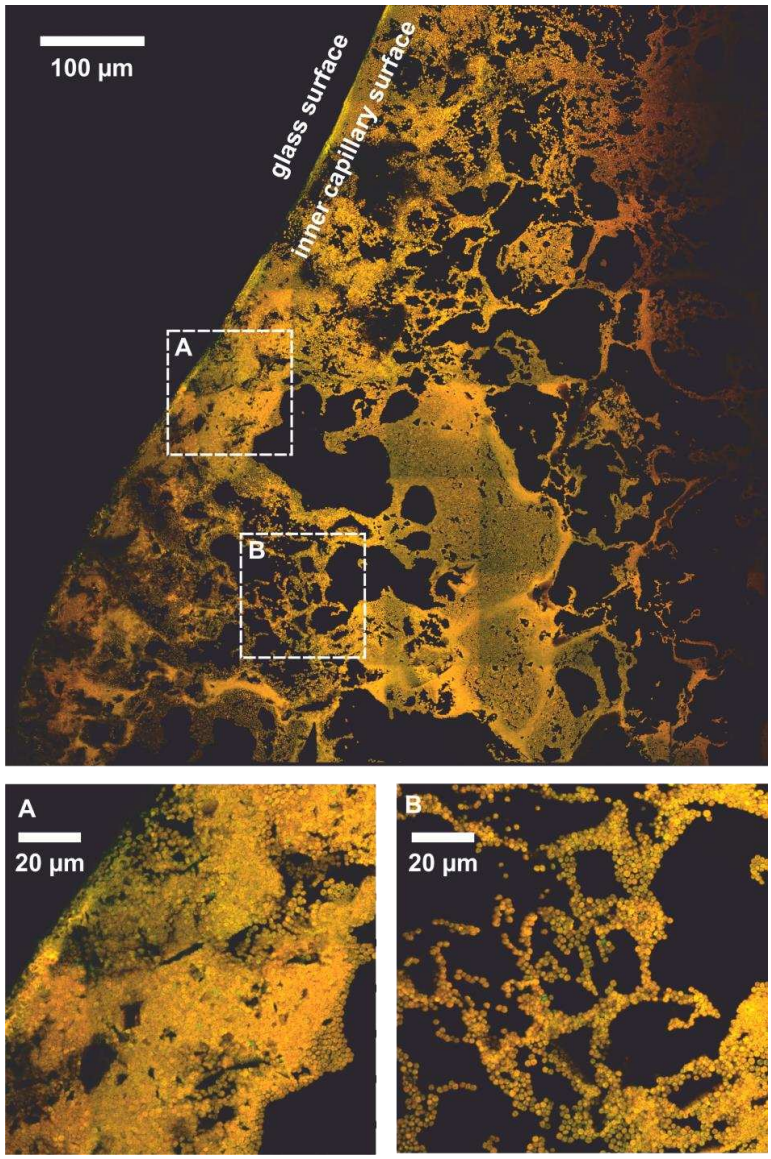

Figure 3-31: High-resolution CLSM picture taken of a *Synechocystis* biofilm capillary cross section

Side view of biofilm grown in a glass capillary for 5 weeks under segmented flow
(Zeiss LSM 780, 40x LD C-Apochromat / 1.2 W, excitation: 488 and 633 nm, emission: green [500-550 nm], red [650 – 700 nm])

Therefore, after 5 weeks of segmented flow biofilm development, cross sections have been prepared from the capillary and were investigated by CLSM (Figure 3-31). This allowed the determination of a thickness of the initial biofilm layer of between 70 and 120 µm. Biofilms are heterogenic, dynamic, three-dimensional structures comprising areas with high cell densities, low cell densities, and channels without any cells. These differences in the composition strongly influence the light attenuation in the biofilm and thus the possible biofilm thickness. Interestingly, the biofilm cross sections were made up nearly exclusively of photosynthetically active cells, and only a few cells (<1 %) without photopigments could be localized, homogenously distributed throughout the biofilm. The anticipated limit for light availability lies within the measured range. Also important, the observed differences in biofilm thickness are corresponding to the expected variances in light attenuation within the biofilm. The negligible biomass concentration in the outlet stream, in addition to the fact, that there were nearly no photosynthetically inactive cells detected at the inner-tube biofilm surface, led to the conclusion that there is no significant biomass formation within the reactor anymore.

Theoretically, one would expect biofilm growth up to a thickness, where one of its main substrates, DIC or light, becomes limiting or accumulated oxygen inhibits growth. Thus, maximal light and DIC penetration depth would define the borders of biofilm growth (Figure 3-30, B). This opens the question why further growth was not observed in these experiments. One explanation might be a quorum sensing signal, which prevents growth within the center of the biofilm, in the presence of high cell density (Ng and Bassler, 2009). Additionally, the oxygen produced within the biofilm might also be a reason for limited growth. A high oxygen concentration would have a negative impact on the carbon capture ability of the cells (Daley et al., 2012).

Improving CLSM biofilm analytics

The investigation of photoautotrophic biofilms by CLSM in the previously described experiments was limited in resolution and penetration depth. The applied capillary flow-through reactor system (Halan et al., 2011)(Figure 3-27, A) had certain advantages. The system could be autoclaved, it was easy to clean and operate, and it was entirely transparent for light. Also, due to the rectangularly shaped capillary, it allowed the formation of the segmented flow pattern without the creation of dead zones (Karande et al., 2014). However, there were also significant disadvantages. Due to the way the glass capillaries were manufactured, it was not possible to produce them as precisely as it is needed for high-resolution imaging with CLSM. The minimal possible

glass thickness available for these capillaries was 240 µm with a variance > ±25 µm. Although the here applied objective could be adjusted to glass thicknesses in between 130 and 210 µm, there was still spherical aberration caused by the thicker and inhomogeneous glass surface. Also, the shape of the capillaries was problematic. The plane area of the rectangularly shaped capillary that was designated especially for the microscopy investigation was still slightly bent, which influenced the measurements as well.

Alternative, commercially available setups are rare. The two contemplable setups, the FC 91 capillary flow cell from Biosurface Technologies (Biosurface Technologies Corporation, Bozeman, Montana, US) and the µ-Slide I Luer flow cell (ibidi GmbH, Martinsried, Germany) were tested but were not suited for segmented flow either due to the limited dimensions (1x1 mm) or the geometry (5x0.8 mm) (data not shown).

Therefore, based on an initial design of Tolker-Nielsen et al. (Tolker-Nielsen et al., 2011) a new flow-through reactor especially suited for this application was designed (Figure 3-32). The main body of the new reactor was laser sintered out of stainless steel and is therefore reusable, autoclavable, and easy to clean. By the addition of two high precision cover slides (170±5 µm, 60x24 mm), one to the top and one to the bottom of the reactor body (Figure 3-32, A.3), two rectangular shaped channels are created (Figure 3-32, A.4).

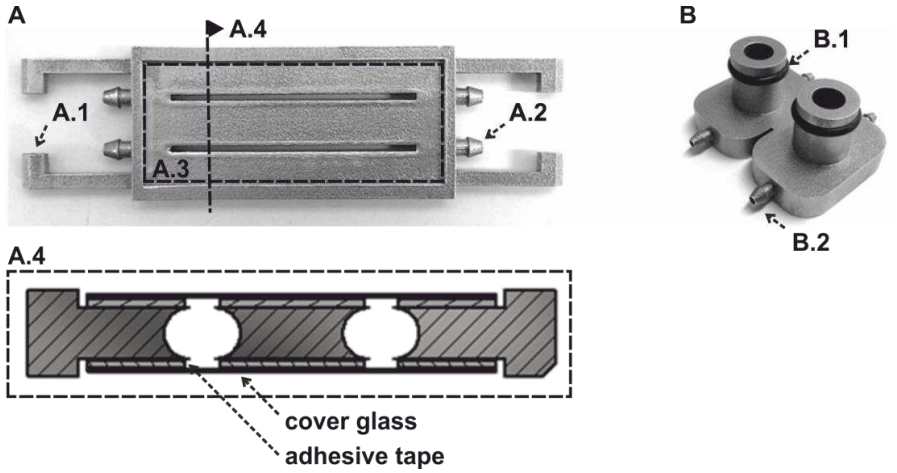

Figure 3-32: Improved flow through reactor and bubble trap design for CLSM biofilm investigation

(A) Flow through reactor design with mounts for the automated microscope stage (A.1), barbed connectors for the tube connections (A.2), and indentation for the cover glasses (A.3). A.4 shows a cross section of the flow through reactor wholly assembled with adhesive tape and cover glasses (B) Bubble trap with sealings (B.1) and barbed connectors (B.2).

The cover slides enable transmitted light as well as reflected light and laser scanning microscopy of the inner glass surfaces. The flow-through reactor is equipped with barbed connectors and can be easily connected to different types of tubing (Figure 3-32, A.2) and a peristaltic pump to realize a medium flow. Several strategies for the application of the coverslips were investigated, including silicon glue, two component adhesives, and adhesive tape, with tape being the most suitable solution. Using a template, the adhesive tape can be previously custom fitted and guarantees a consistent thickness throughout the connection. ACXplus 7054 High Transparency tape (Tesa SE, Norderstedt, Germany) was selected, because of its ability to force a strong connection between glass and metal surfaces, because it is chemically inert, and because of its high temperature and humidity resistance. This allows for the assembled flow cell to be autoclaved and thereby avoids the need for chemical sterilization. The new flow cell assembly allows both optimal conditions for LSM investigations of biofilms and for biofilm growth.

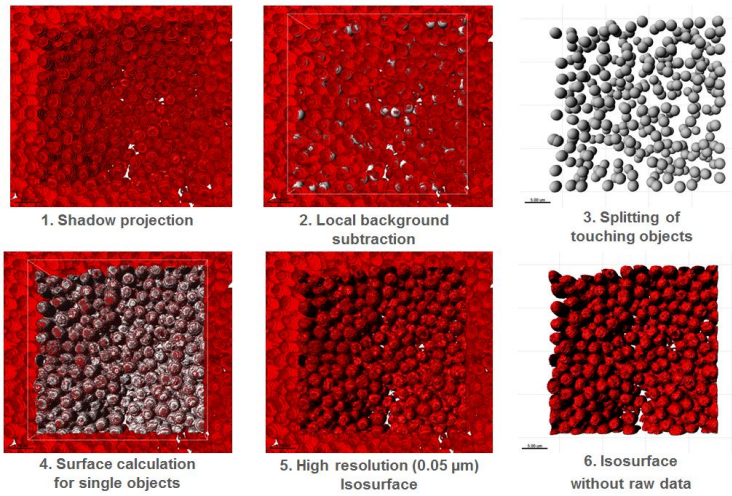

Figure 3-33: High-resolution biofilm surface reconstruction from CLSM raw data

Steps to 3D surface reconstruction from raw CLSM data with Imaris (Bitplane AG, Zürich, Switzerland). High-resolution imaging is restricted to the initial cell layers.

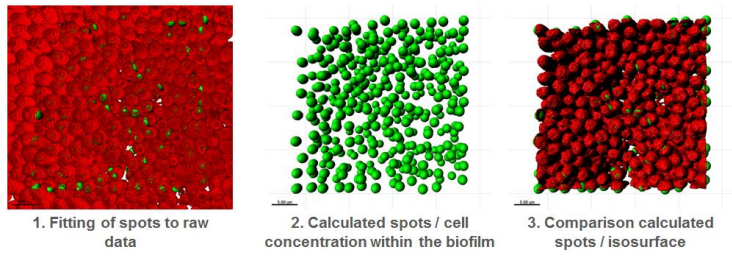

Figure 3-34: Cell detection in CLSM raw data

Cell detection from 3D reconstructions of a biofilm with IMARIS (Bitplane AG, Zürich, Switzerland). Cell detection is restricted to the first 2-3 cell layers.

However, in addition to these technical limitations imposed by the reactor system which influenced the resolution of the images, the capability of the CLSM system to penetrate the thick

photoautotrophic biofilm was limited (Figure 3-29 (B)). Therefore, cross sections had to be prepared to determine the final biofilm thickness (Figure 3-31). This does not allow continuous real-time determination of biofilm growth and structure. The limited penetration capacity is mainly caused by light absorption of chlorophyll a and the phycobilisome, which are both also responsible for the autofluorescence that was used to detect the cells in the first place. The autofluorescence was excited with monochromatic light of 633 nm, which causes an autofluorescence emission in the range of 650 to >700 nm. With this setting, full resolution imaging was restricted to the first 5 cell layers (<20 µm, Figure 3-33) and even with reduced resolution it was not possible to image biofilms that were thicker than 30 - 50 µm. High-resolution imaging of the biofilm would not only improve the determination of biofilm thickness, EPS, and structure (Figure 3-33), but would also enable the determination of cell numbers within the biofilm (Figure 3-34).

Two-photon excitation (TPE) is applied in biomedical research for live deep tissue imaging (Rubart, 2004) and can also enable an improved biofilm penetration (Gerritsen and De Grauw, 1999; Lakins et al., 2009; Neu et al., 2004b). Simultaneous multiphoton absorption allows excitation of fluorophores with near-infrared (NIR) light (700 – 1400 nm) which then emit fluorescence within the visible spectrum. A tunable mode-locked titanium-sapphire laser generates ultrashort pulses of NIR light that penetrates tissue up to 500 µm depth (Dunn and Young, 2006). The thereby generated high photon flux is focused to a sub femtoliter volume, exciting fluorescence exclusively within this area (König, 2000). This avoids the necessity of a confocal aperture, which rejects out of focus fluorescence, thereby minimizing fluorescence losses. More critical, NIR light is less affected by light scattering. Normal NIR light is not absorbed by S*ynechocystis* cells. However, TPE excitation of the photopigments is possible (Neu et al., 2004a). Recently, TPE was

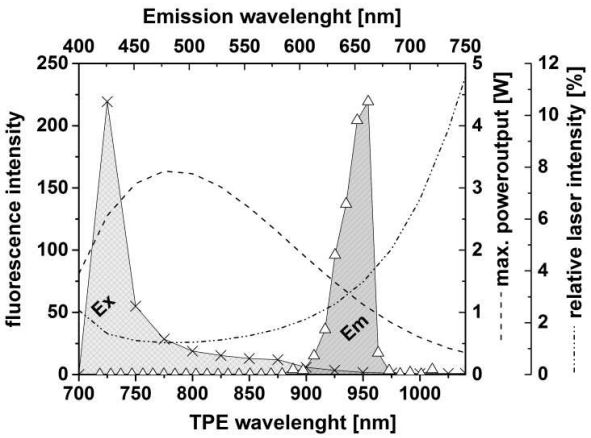

Figure 3-35: TPE fingerprint and respective emission spectrum of *Synechocystis* cells

Diagram showing the fluorescence spectrum and intensity of *Synechocystis* cells upon TPE (Em, upper X-axis). In addition the fluorescence response upon excitation with different wavelength is plotted (Ex, lower X-axis). The difference in power output of the laser at different wavelengths (max. power output) was compensated by variation of the relative laser intensity.

applied for the investigation of plant tissue (Mizuta et al., 2015). TPE proved to reduce the autofluorescence and allowed the detection of GFP tags up to 120 µm deep in leaf tissue.

A TPE fingerprint of *Synechocystis* cells ranging from 700 to 1040 nm revealed strong autofluorescence up to 875 nm. On the other hand, in the range of 900 – 1040 nm, no significant autofluorescence could be detected (Figure 3-35). Upon excitation, the cells emitted fluorescence light in the range from 600 - 675 nm. An optimal resolution could be achieved with a TPE at 850 nm (Figure 3-36, A). However, this resolution was lower in comparison to SPE. Imaging of TPE based autofluorescence did improve the penetration only very slightly (Figure 3-36, B).

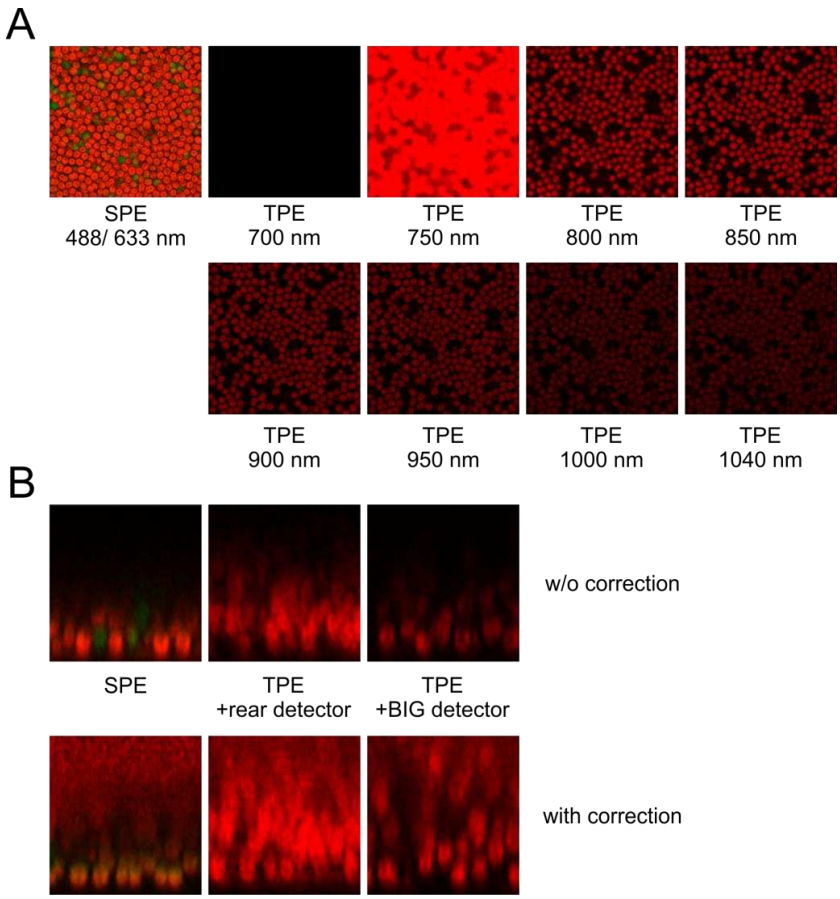

Figure 3-36: TPE resolution with different excitation wavelength in comparison to SPE (A) and penetration capacity and depth resolution of TPE excitation in comparison to SPE (B)

Visualization of the achievable resolution (A) and penetration (B) of a biofilm with TPE (700-1040 nm, 50 nm intervals) in comparison to standard LSM (SPE, 488/ 633 nm). Experiments were carried out with and without increasing the detector gain with depth (with, w/o correction).

Additionally, the resolution achieved with TPE in deeper layers of the biofilm was not significantly improved. Therefore, the TPE of the inherent autofluorescence of *Synechocystis* cells cannot improve the resolution and penetration capacity that would allow for improved biofilm analysis.

However, the absence of autofluorescence in the higher TPE range allows the implementation of specific fluorescent dyes and proteins. In order to further optimize the penetration of the monochromatic laser beam, a fluorophore with an excitation wavelength which does not interfere with the naturally present pigments should be used. In addition, this fluorophore should emit a wavelength that can easily pass the biofilm. In general, for biofilm investigation, a fluorophore can be applied in two different ways, as a non-permanent dye added to the biofilm prior to each investigation, or as constitutively expressed fluorescent protein. Fluorescent dyes are very specific and available for a wide range of applications, but they have the disadvantage that there are expensive and that the biofilm has to be stained in advance before taking an image. Genes of fluorescent proteins can be chromosomally integrated and constitutively expressed. They allow cell detection without staining. A wide range of fluorescent proteins is available today, covering the complete visible and also partly the infrared spectrum. The ideal protein for this application can be excited by TPE in the range of 860 – 1040 nm and emits light that is, if possible, not absorbed by the cells.

4 Discussion

Introduction. Cyanobacterial biotechnology has the potential for sustainable production of chemicals using CO_2, sunlight, and water exclusively. Within the last 10 years, photoautotrophic cyanobacteria, mainly *Synechococcus* and *Synechocystis* strains, have been genetically modified to produce several industrial relevant precursors (Table 1-1). However, the production rates and final titer achieved by these microbial cell factories are low, and an economically viable implementation of such a phototrophic bioprocess seems questionable at this time. In the future, the successful implementation of cyanobacteria as phototrophic microbial cell factories (PMCFs) in the chemical industry requires an improved performance of the biocatalyst. Several studies investigated strategies to overcome the limited production capability of photoautotrophic strains as mentioned in the introduction (Chapter 1.3.1., Table 1-1). Thereby, the research focused on the optimization of cofactor dependency (NADH vs. NADPH), deletion or suppression of competing carbon consuming pathways (e.g., glycogen and PHB synthesis), and optimization of gene expression (e.g., promotor development).

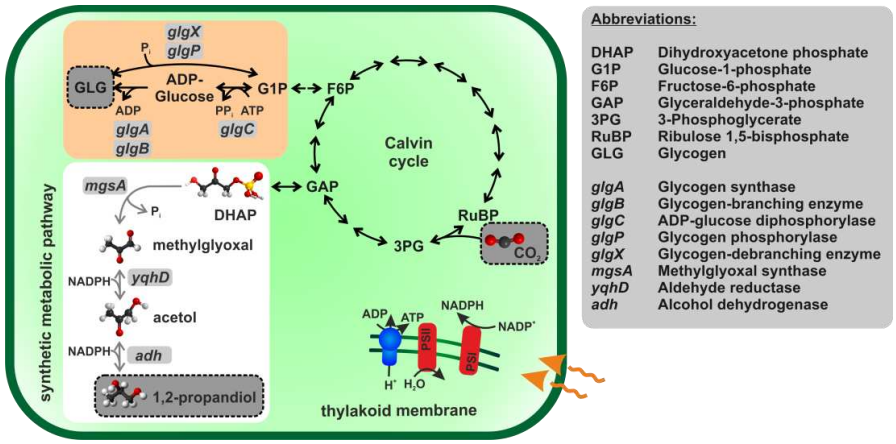

Figure 4-1: Synthetic 1,2 - propanediol pathway and glycogen synthesis in *Synechocystis* PG

In the first step of the propanediol pathway (indicated in the white box), methylglyoxal synthase (*mgsA*) converts the precursor dihydroxyacetone phosphate (DHAP) into methylglyoxal, which is subsequently reduced by a methylglyoxal reductase (*yqhD*) to acetol and then to 1,2-propanediol by a secondary alcohol dehydrogenase (*adh*). Thereby, two NADPH are consumed. Also, the endogenous pathway for the glycogen synthesis and degradation is shown (orange box). Glucose-1-phosphate is converted to ADP-glucose by ADP-glucose diphosphorylase (*glgC*), which is added to the growing glycogen chain by a glycogen synthase (*glgA*). Finally, branching of the polymer is catalyzed by the glycogen-branching enzyme (*glgB*). Glycogen is broken down to G1P by phosphorylation by glycogen phosphorylase (*glgP*).

One example of such an approach is the study by Li and Liao from 2013 (Li and Liao, 2013). In their publication, they describe the construction of a 1,2-propanediol producing *Synechococcus elongatus* PCC 7942 and the following pathway optimization. The authors focused on the redox

cofactor preference of the alcohol dehydrogenase converting acetol to 1,2-propanediol to maximize product titers. Changing from an NADH-dependent alcohol dehydrogenase to an NADPH-dependent enzyme increased the 1,2-propanediol titer significantly from 22 to 150 mg L^{-1}.

In addition, this *Synechococcus* strain produced approximately 85% of the 1,2-propanediol in the stationary phase. However, the phenomenon of 'non-growth'-related productivity was not addressed in that study. This observation is of particular interest because the production of significant amounts of product in the transition to and in the stationary phase was not only encountered with this PMCF but was also observed in some other studies as well. This includes the production of 2,3-butanediol (Oliver et al., 2013), n-butanol (Lan and Liao, 2012), isobutyraldehyde (Atsumi et al., 2009), glycerol (Savakis et al., 2015), and lactic acid (Angermayr et al., 2012; Varman et al., 2013). In the future, the successful implementation of cyanobacteria as "green" photosynthetic microbial cell factories in the chemical industry requires an extended understanding of the underlying regulation of carbon flux and especially of carbon partitioning between product and biomass. Production in the stationary phase prevents further production of biomass and allows the cell to channel all the available carbon into the desired product, which in theory should increase the production rate.

Therefore, a cyanobacterial PMCF producing 1,2-propanediol was created in this study, with the aim to further investigate the observed production of 1,2-propanediol exclusively during the stationary phase. In the following, the previously described results are discussed in detail. An overview of the developed whole cell biocatalyst, *Synechocystis* PG, is given in Figure 4-1, highlighting the central metabolic pathways.

1,2-propanediol formation in the stationary phase

The constructed biocatalyst *Synechocystis* PG produced 1,2-propanediol only during the late growth and stationary phase. In order to exclude missing gene transcription or protein synthesis during the exponential and linear growth phases, the transcript and the proteome were analyzed.

Gene expression and translation. The efficient expression of heterologous genes in the cyanobacterial strains *Synechocystis* and *Synechococcus* is hampered by the limited availability of orthogonal, tight, titratable, and strong promotors. The majority of the up to now used promotor systems is derived from the LacI regulated *lac* promotor. Thereof, the *trc* promotor, which was

also used in this study for the expression of the 1,2-propanediol pathway genes in *Synechocystis* PG, is the most frequently applied (Table 1-1). Expression studies with the *trc* promotor revealed a strong, but only leaky repressed gene transcription (Huang and Lindblad, 2013). This is in accordance with the results reported in chapter 3.2. Maximal 1,2-propanediol synthesis could already be observed in the non-induced culture, induction of *Synechocystis* PG with IPTG did not increase product formation rate or final titer. Expression levels with and without the presence of IPTG were not compared. In case that the addition of the inducer resulted in increased transcript levels, this resulted not in higher reaction rates. Research on modified *trc* descendants improved the repression of gene transcription in the absence of an inducer, but only at the expense of the maximal expression level achieved (Huang et al., 2010). This new generation of synthetic *trc* promotors could also be applied in a *Synechocystis* PG variant. The inducible and titratable expression could be beneficial in further experiments. However, if the protein amount becomes limiting, the inducible gene transcription will come at the expense of activity.

From the transcriptional analysis, it may be concluded that the transcript stability of the full-length RNA covering the whole operon is limiting 1,2-propanediol production, as it was not possible to detect full-length transcripts of *yqhD* and *adh*. However, the respective proteins could be detected by mass spectroscopy at high abundance in all samples. Not so clear was the situation regarding the methylglyoxal synthase (MsgA). Although the *msgA* transcript proofed to be very stable in the Northern Blot, it was not possible to detect the corresponding protein by mass spectroscopy. MgsA is the smallest protein of the three, with an unfavorable trypsin fragmentation pattern, yielding mostly either rather large or very small peptides or peptides with a high histidine content. This could hamper detection of the respective masses. Alternatively, it could be that the protein is indeed absent from the culture, meaning that the *mgsA* transcript is not translated and the conversion of the precursor dihydroxyacetone phosphate to methylglyoxal is catalyzed by a host intrinsic enzyme (*sll0036*, WP_010874019.1, Figure 4-3, Table 4-1). It is important to note that MgsA was not detected by mass spectroscopy during all phases of cultivation, even when 1,2-propanediol production took place. Future experiments should include activity assays with crude cell extracts of *Synechocystis* PG. These extracts should be obtained from different growth stages to finally verify the presence of comparable amounts of active enzyme during cultivation. Additionally, quantitative PCR analysis might give more detailed information on the transcript level during cultivation. However, due to the constraints regarding the PCR probe, only limited information about the stability of the transcript would be obtained in

comparison to the Northern Blot. Due to time limitations, these assays could not be carried out as part of this thesis.

Assuming that the respective enzymes of the 1,2-propanediol pathway were present in the cells at all time points of cultivation, the question remains why the production was restricted to the late and stationary phase. Therefore, the factors limiting growth were investigated.

Phosphate limitation. The data showed that all phosphate present in the YBG11 medium was taken up by the cells at the beginning of cultivation (Figure 3-9). The maximum optical density of the *Synechocystis* PG cultures correlated to the provided phosphate amount indicating a phosphate limitation at the end of batch growth in YBG11. However, other studies reported a sulfate (van Alphen et al., 2018) limitation or lower phosphate content of the cells during phosphate induced growth limitation as compared to our results (Trautmann et al., 2016). These differences might be related to the different strain background or might be caused by different cultivation conditions. Medium with twice the concentration of nutrients did not result in twice the amount of biomass (Figure 3-8) which indicates another limiting compound like PAR or DIC.

Limited improvement of 1,2-propanediol production due to elevated light intensities and CO_2 availability

In the experiments described in chapter 3.3, the influence of the provided light intensity and DIC on biomass formation, 1,2-propanediol production and glycogen accumulation of *Synechocystis* PG was investigated.

Biomass formation. Elevated light intensities led to a prolonged exponential growth phase and were also reflected in the slope during the linear growth phase (Figure 3-10, Table 3-1), which became steeper with increasing light intensity. Previously published studies with *Synechocystis* wild-type cultures reported increasing exponential growth rates with increasing light intensity (Trautmann et al., 2016; Zavřel et al., 2014). However, an increase in exponential growth rate was not expected during these experiments due to the applied stepwise increase in light intensity, which became necessary due to the light sensitivity of the recombinant strain.

It could also be shown that an atmosphere with an ambient CO_2 concentration (0.04%) limits the growth of *Synechocystis* PG (Figure 3-13, Table 3-4). This limitation was reflected in a shortened exponential growth phase accompanied by a low increase in biomass during the prolonged linear growth phase. All in all, light intensity and CO_2 partial pressure had only limited influence on the

process duration due to the overall slow growth rate of the *Synechocystis* strains. Anyhow, in this case the growth phase where the biocatalyst is produced has to be distinguished from the 1,2-propanediol production phase, even though both phases are linked via glycogen. Glycogen production was taking place during the linear and late growth phase, which had significant influence on the following production phase (Figure 4-2). Consequently, the influence of both substrates on the glycogen production during the growth phase and on the glycogen catabolism during the production phase was analyzed.

Glycogen accumulation and catabolism. The altered cultivation conditions influenced the accumulation of intracellular glycogen. The highest glycogen amount (27.5 mM_C) accumulated at high light and high carbon conditions (HL - 250 µmol m^{-2} s^{-1}, HC - 2%, Figure 4-2). While the accumulated glycogen concentration was dependent on the light intensity (Table 3-5, page 60), the maximal glycogen titer was stronger affected by a decreased carbon availability in the growth phase (Figure 4-2). This was also reflected in the rate of glycogen production. However, due to the limited amount of sampling points during this phase, the rates could not be determined reliably. This result was expected as glycogen is the major carbon storage compound and carbon will be directed to essential biomass components during carbon limited growth. The same dependency of glycogen accumulation and light intensity was also observed by Monshupanee (Monshupanee and Incharoensakdi, 2014). Taking a closer look at the production phase, the highest glycogen utilization rate was also observed under high light, high carbon conditions (-7.2 mM_C day^{-1}). The higher glycogen utilization rate might be a result of the higher glycogen amount available, or it could be connected to the performance of the synthetic pathway. Following experiments showed faster glycogen catabolism in the recombinant strain in comparison to the wild-type strain (Figure 3-15). Therefore, the faster glycogen turnover rate might be a direct result of the higher carbon drain due to the increased activity of the synthetic pathway.

1,2-propanediol production. The 1,2-propanediol production rate was highly dependent on the light intensity (-73%, HC, HL → HC, LL, Figure 4-2), whereas the influence of DIC was small in the investigated range (HC, HL → LC, HL, Figure 4-2). In contrast, the resulting final titer was equally dependent on light intensity and DIC. One explanation could be provided by the need of NADPH as reduction equivalent for the 1,2-propanediol production pathway. Following experiments revealed a major contribution (75%) by the Calvin cycle to the 1,2-propanediol synthesis. The energy dependency of the Calvin cycle might be reflected in these results. An alternative explanation might be the energy consumption of the 1,2-propanediol pathway itself. The reduction

of DHAP to 1,2-propanediol requires 2 NADPH which can be supplied by the light reactions whereas glycogen catabolism would provide mainly NADH. However, further investigations are necessary to explain this behavior. Those could include experiments with identical cultivation conditions in the growth phase, while only the light or DIC amounts during the production phase are varied. This would allow an independent study of the influence on the production phase without interference by the size of the previously accumulated glycogen pool. Experiments conducted by Li and coworkers (Li and Liao, 2013) revealed an improved 1,2-propanediol production when a NADPH-dependent replaced the applied NADH-dependent dehydrogenase. The investigation of a modified *Synechocystis* PG with the original NADH-dependent dehydrogenase instead of a NADPH-dependent might give insight into the source of reduction equivalents utilized for 1,2-propanediol production.

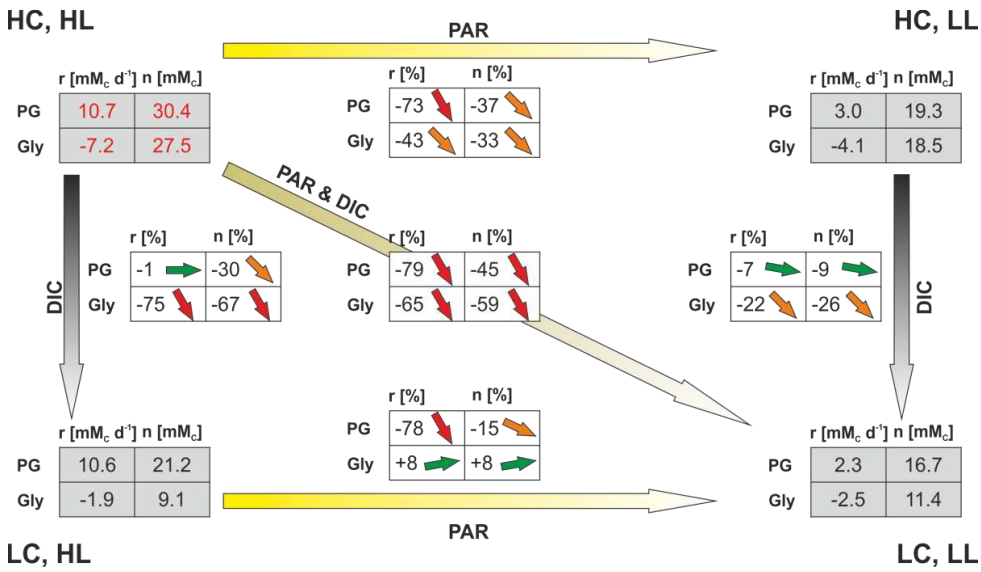

Figure 4-2: Influence of changed light intensity and CO_2 availability on glycogen and 1,2-propanediol titers and rates

PG – 1,2- propanediol, Gly – Glycogen, HC – high carbon (2%), LC – low carbon (0.04%), HL – high light (250 µmol m^{-2} s^{-1}), LL – low light (50 µmol m^{-2} s^{-1}), r – 1,2-propanediol production rate or glycogen turnover rate [mM_C d^{-1}], n – maximum 1,2-propanediol or glycogen titer [mM_C], changes are given as percentages of the maximal rates or concentrations at HC, HL conditions (marked in red), respectively. Data obtained from Figure 3-11, Figure 3-14, Table 3-2 and Table 3-5.

All in all, the accumulation of glycogen during the late growth phase is hampered by an insufficient CO_2 availability and also, but to a lower extent, by insufficient light intensities. The 1,2-propanediol production window correlated with the glycogen availability. Therefore, reduced glycogen resulted in shorter 1,2-propanediol production time. Even if the 1,2-propanediol pro-

duction rate is unaffected, 1,2-propanediol titers decreased. However, where the propanediol production rate is not affected by lower CO_2 availabilities, it is highly light dependent. The decreased 1,2-propanediol production rate under light limitation is partly compensated by increased production time. The results of the experiments with changing light intensities and variable CO_2 concentrations indicated a direct influence of the energy provided by the light reactions on the 1,2-propanediol production as well as a connection between the presence of glycogen and propanediol production.

The comparison to other studies is hindered by a wide range of light sources and CO_2 supply (see also chapter 1.3.2, Table 1-1). The influence of light intensity and CO_2 concentration on the growth of *Synechocystis* was investigated during the last years (e.g., Benschop et al., 2003; Martínez et al., 2011). Despite the importance of the substrates light and CO_2 also for the productivity of synthetic pathways, an optimization of cultivation conditions was seldomly published so far. The comparison of the process performance of the diverse processes with different irradiation intensities and DIC is inconclusive (Table 1-1). Due to the different branching points and a different carbon and energy consumption, a conclusion concerning the influence of light and DIC on the heterologous production in general cannot be derived.

Regarding process development, cultivation at 2% CO_2 and 200 - 250 µmol m^{-2} s^{-1} resulted in maximal 1,2-propanediol production rates. Higher light intensities and carbon dioxide concentrations did not improve propanediol production beyond this point.

Intracellular carbon fluxes during 1,2-propanediol production

The tight regulation of the carbon flux during photoautotrophic growth may be a reason for the limited production rates achieved with photoautotrophic hosts so far. As described in chapter 3.4, the 1,2-propanediol synthesis stopped as soon as the glycogen pool was depleted. Manipulating glycogen synthesis to reduce the carbon flux to glycogen did not have a beneficial effect on 1,2-propanediol synthesis (Figure 3-16, Table 3-6). Instead of improving productivities, product titers were dramatically reduced with no influence on the setting of the production phase. The synthesis of other fermentation products such as succinate and acetate were also reported to be directly coupled to glycogen. In these cases, the carbon and energy were solely delivered by the reactivation of the storage compounds in dark and anoxic conditions (Hasunuma et al., 2016).

Carbon flux analysis. To understand how the carbon is distributed between the different carbon sinks in the stationary phase, the glycogen pool was saturated with labeled carbon atoms. The experiment revealed that during propanediol production 25% of the used carbon was derived from glycogen whereas the other 75% were provided by the Calvin cycle (Figure 3-17, Table 3-7). This is in accordance with the results of the previously described knock-out experiments (Chapter 3.4). Consequently, the question occurred whether light is required for the generation of the carbon from the Calvin cycle. Therefore, further experiments under dark conditions were conducted. Surprisingly, no 1,2-propanediol synthesis took place without light (Figure 3-18, Table 3-8). It was expected that the 75% 1,2-propanediol contributed by the Calvin cycle cannot be produced in darkness as the Calvin cycle depends on the energy supply from the photosynthetic reactions. However, it was also expected that the 25% 1,2-propanediol contributed by glycogen would still be produced as glycogen was available at high concentrations. Nevertheless, this did not happen. Although glycogen was catabolized rapidly, no 1,2-propanediol was produced. Only after light was provided again and the glycogen pool was restored, 1,2-propanediol synthesis was observed.

The developed cultivation technique, which allows the differentiation of carbon derived from glycogen and the Calvin cycle directly, can be applied for further experiments in the future. The combination with experiments concerning the influence of light intensity and DIC on 1,2-propanediol formation as described in chapter 3.3 would allow the analysis of carbon fluxes during the production phase.

All in all, 1,2-propanediol is produced from carbon contributed by glycogen and the Calvin cycle. The production only takes place under phosphate limitation, carbon excess and while light is supplied. Therefore, an unknown underlying regulation of the carbon flux is suspected.

Methylglyoxal bypass. The heterologous methylglyoxal synthase applied here as part of the 1,2-propanediol synthesis pathway is in its natural host *E. coli* part of the methylglyoxal bypass (Figure 4-3). This bypass is active under phosphate-limiting conditions and when phosphorylated sugars (e.g., GAP, DHAP) accumulate (Hopper and Cooper, 1971). The methylglyoxal bypass enables bacteria to maintain carbon flux through the cell under phosphate starvation. DHAP is converted to methylglyoxal, whereby orthophosphate is liberated which can be used in glycolysis by the glyceraldehyde-3-phosphate dehydrogenase (GAPDH) for the conversion of GAP to 1,3-bisphosphoglycerate (1,3-BPG). The produced methylglyoxal is converted to lactate and finally to pyruvate without further production of ATP (Cooper, 1984). The activity of the methylglyoxal

pathway is also part of the overflow metabolism when an excess of carbohydrates enters the central metabolism (Tötemeyer et al., 1998). This pathway is tightly regulated due to the toxicity of methylglyoxal and the potentially wasted energy.

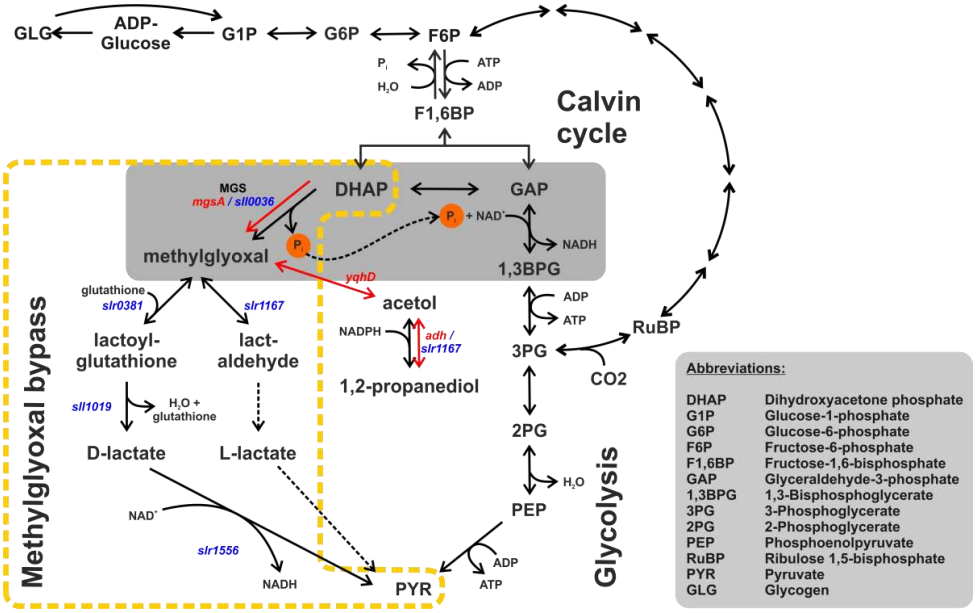

Figure 4-3: Proposed methylglyoxal bypass in *Synechocystis* PG

Schematic representation of the central carbon metabolism of *Synechocystis* PG showing the methylglyoxal bypass as found in various prokaryotes. Endogenous *Synechocystis g*enes with either high sequence identity (*sll0036*) to known pathway genes or with proven activity for this reaction are shown in blue. Introduced heterologous genes that are part of the 1,2-propanediol pathway are shown in red.

The methylglyoxal bypass has not yet been described in the here investigated host strain *Synechocystis*. However, candidate genes in the genomic sequence (Table 4-1) of *Synechocystis* PG could be identified which show a high sequence similarity and E-value to the ones encoding the methylglyoxal pathway in *E.coli*. Specifically, the amino acid sequence derived from the gene *sll0036* shows high similarity with other known MGS from *E. coli, Clostridium acetobutylicum,* and *Bacillus subtilis* (Huang et al., 1999). The proteins encoded by the genes *slr0381*, *sll1019*, and *slr1556* complete the methylglyoxal pathway (Figure 4-3). Respective catalytic activities have already been described in literature (Knoop et al., 2013; Miao et al., 2017; Shimakawa et al., 2013).

Table 4-1: Comparison of amino acid sequences derived from genes encoding for the enzymes of the methylglyoxal bypass in *E. coli* to respective putative enzymes in *Synechocystis* PCC 6803.

	Accession number						
	E. coli	*Synechocystis*	Total score	Query cover	E-value	Identity[4]	REF
methylglyoxal synthase	WP_000424181.1	WP_010874019.1	123	76%	4e-35	47%	[1]
lactoylglutathione lyase	WP_001237796.1	WP_010873329.1	176	92%	4e-59	65%	[2]
hydroxyacylglutathione hydrolase	WP_001052715.1	WP_010871579.1	206	100%	3e-67	41%	[2]
D-lactate dehydrogenase	WP_000762236.1	WP_010874176.1	357	99%	2e-124	51%	[3]

Data derived from BLASTP 2.8.0, NCBI. [1] (Huang et al., 1999), [2] (Shimakawa et al., 2013), [3] (Angermayr et al., 2016a) [4] the respective amino acid sequences have been compared.

Based on the results presented here, it can be hypothesized that *Synechocystis* utilizes a methylglyoxal bypass under phosphate starvation and that the heterologous 1,2-propanediol pathway of *Synechocystis* PG is indeed subject to the same regulation that controls the methylglyoxal bypass via the methylglyoxal synthase. A crucial component in this context would then be phosphate, which was the first essential compound to be depleted during batch growth. During the growth phase, excess phosphate and low DHAP/GAP concentrations would repress the methylglyoxal bypass (Figure 4-4, A). Carbon and energy are used for growth and glycogen synthesis. At one point phosphate is depleted, which would open the methylglyoxal bypass and simultaneously causes a growth arrest. During this phase glycogen catabolism is initiated, which in turn leads to enhanced GAP/DHAP levels potentially increasing the flux through the methylglyoxal bypass and thereby through the 1,2-propanediol pathway (Figure 4-4, B_L). Due to the orthophosphate dependency, the carbon flux from the glycogen reserve is split equimolar between the methylglyoxal bypass and the lower branch of the glycolysis (Figure 4-3), which is mirrored in the derived data showing about 50% of the carbon originating from glycogen being channeled into the product 1,2-propanediol (Figure 3-17, C and E). In the absence of light (Figure 3-18, C; Figure 4-4, B_D) the glycogen reserve was consumed rapidly. However, without the light reactions, no additional carbon inflow from the Calvin cycle is to be expected. The limited energy supply might even increase the P_i and PP_i availability. Therefore, the GAP/DHAP levels are low, and the methylglyoxal bypass is inactive. No 1,2-propanediol formation takes place. Restored PAR leads to glycogen production (Figure 3-18, C; Figure 4-4, C). With glycogen as a carbon sink, excess DHAP/GAP is channeled into the glycogen pool. The GAP/DHAP concentrations are kept low, and the methylglyoxal pathway stays inactive. However, as soon as glycogen is catabolized again in

the presence of an active Calvin cycle, the bypass is reactivated resulting in 1,2-propanediol production (Figure 3-18, C-F; Figure 4-4, D). In this context, deletion of *glgC* would prevent glycogen accumulation during the growth phase. Later on, during the stationary phase, the lack of glycogen would reduce the carbon flow into glycolysis and decrease the levels of phosphorylated carbohydrates. Subsequently, the flux into the methylglyoxal bypass would be lower, also causing a drop in 1,2-propanediol production. Precisely this behavior was seen for *Synechocystis* Δ*glgC* PG.

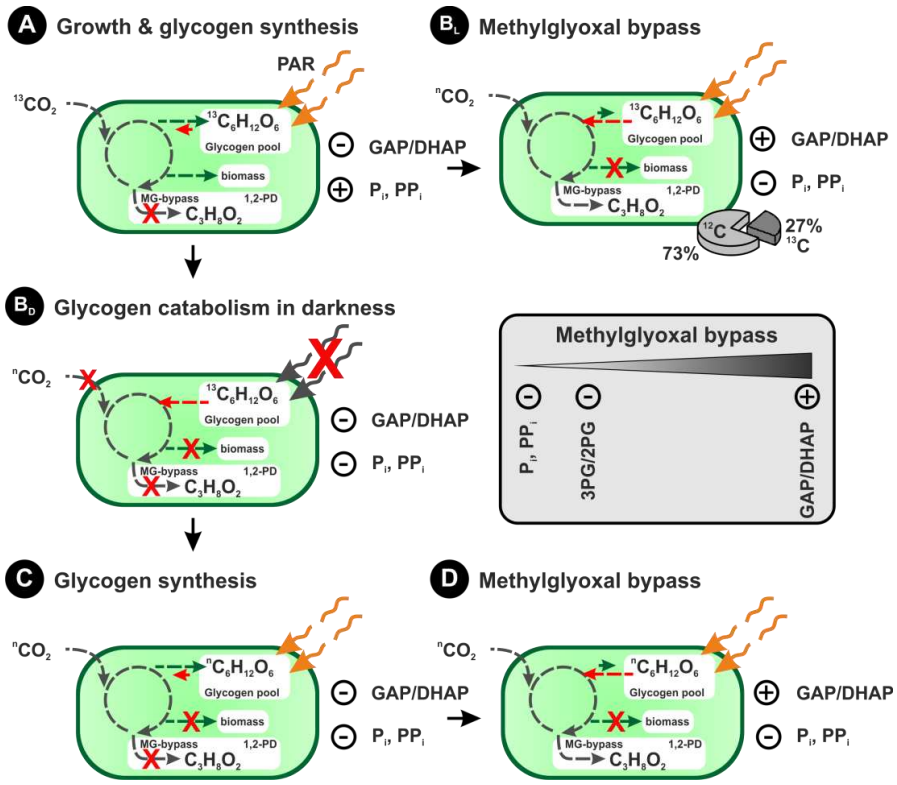

Figure 4-4: Interrelation of the different carbon sources and sinks considering biomass, glycogen turnover, and the methylglyoxal bypass

(A) Growth and accumulation of fully labeled glycogen from $^{13}CO_2$, **(B_L)** "mixotrophic" production of 1,2-propanediol from glycogen and $^{n}CO_2$, **(B_D)** glycogen turnover in darkness, **(C)** replenishing of the glycogen pool from $^{n}CO_2$ under light conditions, **(D)** production of unlabeled 1,2-propanediol from glycogen and $^{n}CO_2$ under light conditions.

It can be concluded that the activity of the 1,2-propanediol pathway is connected to a regulation that controls the entrance of DHAP into the methylglyoxal bypass. The activity of the 1,2-propanediol pathway is therefore controlled by phosphate and GAP/DHAP levels, which influence the activity of either the heterologous or the host intrinsic methylglyoxal synthase or both.

Glycogen content influences OD_{750} measurement

During the experiments with glycogen determination, it became apparent that the OD_{750} is influenced by the variable glycogen content inside the cells. The collected data sets could be used to establish a correlation between the ratio of OD_{750} and cell number and the intracellular glycogen content (Figure 4-5). This correlation can be applied above a ratio of 4.6 or a glycogen content of 2.5 mM_C, respectively. Below these values, the influence of the glycogen content on the OD_{750} is not pronounced enough to allow a reliable estimation. This correlation enables a fast and efficient estimation of the glycogen content of *Synechocystis* and *Synechocystis* PG cultures without the need for glycogen isolation, hydrolysis, and glucose determination.

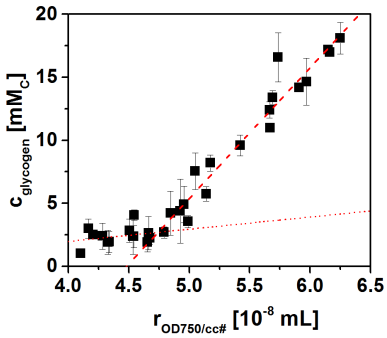

Figure 4-5: Correlation of the quotient of OD_{750} and cell concentration to the glycogen concentration

(Data derived from Figure 3-17 and Figure 3-18)

1,2-propanediol production in photobioreactors

Chapter 3.5 reports the transfer of the process from shaking flasks to the 2-3L bioreactor scale. While the process could be realized also in benchtop bioreactors, the final 1,2-propanediol titers were significantly reduced in comparison to the experiments conducted in shaking flasks. In case of the stirred tank bioreactor, lower product titers had to be expected. Due to the bioreactor design, light can only be supplied to the outer layers of the culture and cells will only seldomly pass an irradiated zone. Therefore, limited light availability is an issue. Insufficient irradiation has already proven to reduce product formation in shaking flask experiments (Chapter 3.3). However, this is not the case for the flatpanel bioreactors. These bioreactors were specially designed with a confined thickness of the culture vessel to prevent light limitation. Nevertheless, only 50% of the 1,2-propanediol titers achieved in shaking flasks could be realized in this reactor setup. The major differences during cultivation were the light intensity and the mode of aeration. The light unit in the shaking flask incubator was calibrated measuring light conditions in an empty incubator. Therefore, the adjusted light intensity during shaking flask cultivations was

overestimated, as the influence of the shaking flasks and their sterile closures on top on the light intensities in the bacterial cultures were not considered. An additional unknown factor is the mass transport resistance of the sterile closures, as explained in chapter 3.3. While the shaking flasks cultures sealed with a gas permeable closure stood in a chamber with an atmosphere containing 2% CO_2, the organisms in the bioreactors have been directly aerated with 2% CO_2 enriched air. The sterile closure represents a mass transport hindrance that reduces the carbon availability inside the flasks. However, all these factors do not satisfyingly explain the significantly lower productivities reached in the bioreactor in comparison to the shaking flask experiment.

A carbon balance (Chapter 3.5, Figure 3-22, Table 3-12) revealed the production of approximately 8 mM_C of unknown carbon-based side products by the wild-type strain. The applied analytics could not identify the side products. However, the formation of significant amounts of commonly known fermentation products (e.g., acetate, pyruvate) can be excluded. In contrast, it was possible to close the mass balance for the recombinant strain. Thus, side product formation of the recombinant strain under these conditions can be excluded. The carbon distribution at the beginning and the end of the 1,2-propanediol production phase is visualized in Figure 4-6. Before 1,2-propanediol synthesis, all the carbon taken up from the aeration (77.8 mM_C) was used to assemble 79.1 mM_C biomass including 24.4 mM_C glycogen (Figure 4-6, A).

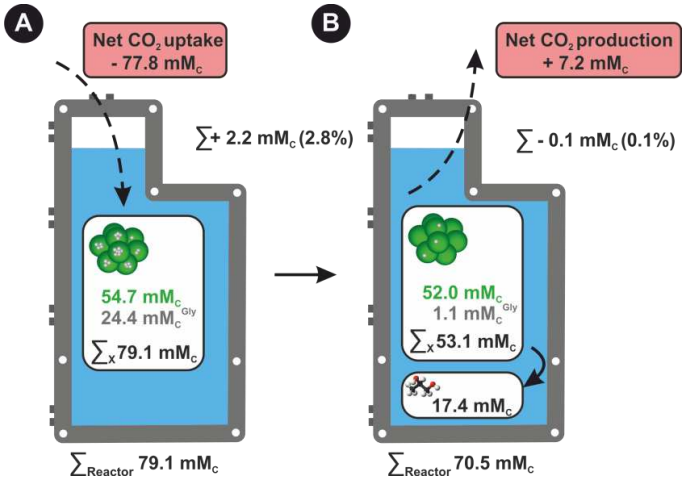

Figure 4-6: Carbon distribution at the start and the end of the production phase of *Synechocystis* PG

Schematic representation showing the carbon distribution after the growth phase (A) and after the production phase (B). The amount of carbon stored in biomass ($\sum x$) consists of the amount of carbon stored in glycogen (marked in grey) and carbon which is part of the remaining biomass (marked in green, data derived from Figure 3-22 and Table 3-12)

During 1,2-propanediol production, the glycogen pool was consumed while the rest of the biomass remained. The catabolized amount of glycogen (23.3 mM_C) could nearly sustain the production of 17.4 mM_C 1,2-propanediol as well as the evolution of 7.2 mM_C CO_2 (Figure 4-6, B). This is also supported by the net oxygen consumption during 1,2-propanediol production (Figure

3-22). With limited energy provided by the light reactions, reduced CO_2 fixation was to be expected.

In contrast to the observations in the shaking flasks experiments, no significant contribution of the Calvin cycle to the product formation could be observed. Whereas the shaking flasks had a net CO_2 uptake of at least 13 mM_C during the production phase (Table 3-7, 22 mM_C of unlabeled CO_2 taken up vs. 8.7 mM_C of glycogen that could be oxidized), a net production of 7.2 mM_C CO_2 was measured during the production phase of the bioreactors. The total carbon and energy needed for the propanediol production seemed to be provided by the glycogen pool. This is the most likely explanation for the by 50% decreased propanediol titer during these experiments.

The maximum CO_2 uptake rate (20.1 mM_C d^{-1}) measured at the transition from the late growth to the stationary phase could not be re-directed to the production of 1,2-propanediol under the applied conditions. However, also in comparison to the shaking flask experiments where a production rate of 6.3 mM_C d^{-1} was observed with 5 mM_C d^{-1} directly contributed by the Calvin cycle, the production rate was 25% lower than the maximal measured CO_2 fixation rate in this experiment. In comparison to the majority of processes listed in Table 1-1, the carbon provided by the Calvin cycle was utilized entirely for product synthesis by *Synechocystis* PG and is not shared with biomass formation during the production phase. The capacity for carbon assimilation is only partly utilized for product formation.

The determination of the carbon uptake rate also allows the calculation of the 1,2-Propanediol yield on CO_2 ($Y_{P/S}$). Approximately 22% of the assimilated carbon were finally redirected to the product. The carbon distribution between biomass and product was still in favor of biomass (66%). The yield of product on biomass ($Y_{P/X}$) is approximately 33%. If the glycogen storage can be replenished, 1,2-propanediol might be produced repeatedly. This would shift the carbon distribution towards the product and might allow the continuous usage of the biocatalyst.

The combination of reactor experiments and $^{13}CO_2$ experiments would be a starting point for in-depth flux investigation. However, $^{13}CO_2$ is too expensive for an economically feasible application in bioreactor experiments. Instead, the shaking flask cultivation system might be extended by off-gas analytics in the future, which would allow the measurement of carbon uptake while restricting the costs for labeled CO_2.

In addition to the batch experiments, it was also attempted to produce 1,2-propanediol continuously with *Synechocystis* PG (Chapter 3.5). Whereas production could not be established in a

turbidostat (data not shown), 1,2-propanediol formation with a low rate of 0.27 mM_C d^{-1} was observed under nutrient limitation in a chemostat (Figure 3-24). In this situation, growth was restricted by phosphate availability. However, cells were still growing, and glycogen was produced. Regarding the methylglyoxal bypass hypothesis, the phosphate limitation would enable methylglyoxal production by the methylglyoxal synthase. The remaining biomass synthesis, including glycogen, would keep the DHAP/GAP low restricting the 1,2-propanediol production. An even lower dilution rate might increase phosphate starvation and further restrict glycogen and biomass formation, which might enable higher continuous production rates for 1,2-propanediol.

Some studies reported the production of organic acids from storage compounds under dark and anoxic conditions (Table 1-1). In this context, the cells were also cultivated under dark oxic and dark anoxic conditions. Whereas glycogen catabolism was triggerd by dark oxic conditions, no product formation was observed. This result was already expected from the shaking flasks cultivation in darkness. After the replenishing of the glycogen pool, the cells were transferred to dark anoxic conditions. Under these conditions the cells utilized only minor amounts of their glycogen storage and again no product formation was observed. Instead, the accumulation of low amounts of organic acids in the medium could be detected. As already seen in the shaking flasks experiments, 1,2-propanediol production is depending on the availability of light and glycogen catabolism. Without both, no 1,2-propanediol production took place. Due to the regulation of the methylglyoxal bypass, different strategies for the successful production of 1,2-propanediol have to be developed.

Characterization of *Synechocystis* biofilms

For the successful application of photosynthetic microbial cell factories not only the biocatalyst performance has to be improved. Also, new process concepts have to be developed. Therefore, the capability of S*ynechocystis* to form a monospecies biofilm was investigated (Chapter 3.6). During these experiments, stable *Synechocystis* biofilms could be cultivated. Thereby, biofilm growth could be controlled by introducing air segments. The resulting interfacial and hydrodynamic forces shaped the biofilm structure and enabled continuous cultivation. The experiment was maintained for five weeks during which no additional biomass formation was observed. Neither grew the biofilm in size nor was biomass flushed out.

Investigation of the biofilm structure by CLSM revealed a flat, dense biofilm structure. However, the image quality of the biofilm was influenced by the reactor geometry. Therefore, a new flow cell design (Chapter3.6, Figure 3-32) specifically optimized for CLSM applications in biofilm research was developed. The new reactor design enabled high-resolution imaging of the initial biofilm layers. However, imaging was still restricted by the limited penetration of the specimen. One promising strategy for higher increased in depth resolution is the excitation with multiple photons simultaneously. Attempts to increase the penetration depth by multiphoton excitation showed only limited success (Figure 3-36). Due to the high density of cells and the resulting number of photopigments, light penetration and emission are especially problematic with photoautotrophic biofilms. Further improvement might be made with fluorescent proteins that are excited by and emit light at a wavelength that does not interact with the contained photopigments.

In summary, biofilm cultivation of *Synechocystis* could be established, and the successful continuous cultivation makes this a promising approach for further process development. Especially the immobilization of cells in combination with reduced biomass formation might reduce the carbon consumption by biomass formation and enable increased production rates.

5 Conclusions and Outlook

In the presented work, the strain *Synechocystis* sp. PCC 6803 was modified to enable the production of 1,2-propanediol from CO_2 and light. Therefore, different stages of bioprocess development have been addressed, including pathway engineering, biocatalyst characterization, reaction engineering, and process engineering.

Phosphate starvation, the resulting limitation of growth, active glycogen catabolism, and the availability of light were identified as the key factors influencing 1,2-propanediol production. Production of 1,2-propanediol is coupled to the stationary phase and concomitant glycogen catabolism. This behavior seems to be the result of methylglyoxal synthase regulation in the context of the methylglyoxal bypass. These findings are relevant also for other pathways withdrawing DHAP from the Calvin cycle via a methylglyoxal synthase. The influence of the carbon partitioning on biomass, storage compounds, and synthetic pathways is of primary interest for all photoautotrophic fermentation approaches. Redirection of the carbon flux towards the desired product is one fundamental approach for the large-scale application of this technology. These findings indicate that prevention of carbon flux to storage compounds is not always necessary to achieve high productivities. Synthesis and accumulation of storage compounds during photoautotrophic growth and semi-fermentative production of value-added compounds from glycogen might also be one promising strategy.

The optimization of CO_2 and light supply to the needs of the production host via reaction engineering resulted in an improvement of final product titers. A maximal product concentration of 12 mM was reached, which is six times higher than any previously reported value (Li and Liao, 2013). Similarly, the production rate was increased by a factor of 4. However, despite an evident influence of the cultivation parameters on 1,2-propanediol production, only limited improvement of the production rate and final titers could be made.

Further improvement of the biocatalyst performance might be achieved by enzyme engineering. Mutagenesis of the methylglyoxal synthase to reduce the inhibition by phosphate might release the restriction of 1,2-propanediol to the stationary phase. Additionally, future optimization of the biocatalysts expression cassette could involve the construction of separate transcriptional units for the three genes of the pathway to limit post-transcriptional events and to control the amount of each of the enzymes independently as was suggested by Savakis et al. (Savakis et al., 2013). Additional enzyme activity assays with crude cell extract could accompany this approach together with qPCR analysis as already discussed before (Chapter 4). Another possible strategy is the screening for different host strains. In addition to the here applied *Synechocystis* strain, *Syn-*

echococcus elongatus sp. PCC 7942 is often applied as chassis for biotechnology (Table 1-1). With *Synechococcus elongatus* UTEX 2973, another promising chassis with high growth rates was recently described (Yu et al., 2015). However, during initial experiments with both strains carrying the chromosomal integration of the 1,2-propanediol pathway, only the toxic intermediate methylglyoxal accumulated (data not shown).

Another target for optimization are the process conditions. The transfer of the process to the benchtop bioreactor scale resulted in significantly lowered product titers and revealed a strong influence of technical variations of the cultivation systems on the process performance. Nevertheless, phosphate limited continuous cultivation of the biocatalyst enabled ongoing 1,2-propanediol production in bioreactors. Despite the low observed production rate, this might be a starting point for further process improvement. A stronger phosphate limitation and therefore further limited growth has the potential to still maintain the biocatalyst while simultaneously increasing the activity of the methylglyoxal synthase and the carbon flow towards 1,2-propanediol.

Reactor and process engineering for phototrophic whole cell biocatalysis requires a re-thinking of familiar reactor concepts. The essential substrates light, water, and carbon dioxide necessitate different process concepts and technical solutions compared to today´s applications in biotechnology. The available reactor configurations aim at maximal biomass production. However, this is usually suboptimal for production. This is also true for the suitability of biofilms as catalysts for continuous chemical synthesis which necessitates controllable porosity and growth as well as the activity of all cells in the biofilms. These qualities could be achieved with the here described segmented flow concept. Continuous processes, controlled biomass formation and regeneration of the biocatalyst are mandatory to enable the efficient production of value-added compounds and biofuels from sunlight and CO_2.

The observation of continuous 1,2-propanediol production under phosphate-limited growth in combination with the established segmented flow biofilm cultivation could potentially enable biomass retention by self-immobilization and would allow an even stronger phosphate limitation. In addition to the results presented in this thesis, initial studies concerning the biofilm formation of *Synechocystis* PG and first attempts at an upscaling of the biofilm setup to bench scale were made. During those experiments conducted with different benchtop scale biofilm reactors concepts (data not shown), traces of 1,2-propanediol could be detected. Those reactor concepts might be used as a starting point for further process optimization.

Already published photosynthetic microbial cell factories (Table 1-1, Figure 5-1) cover the range from proof of principle studies with only traces of product produced to the benchmark processes for the production of ethanol (Gao et al., 2012), 2,3-butanediol (Oliver et al., 2013) and isobutyraldehyde (Atsumi et al., 2009). With the exception of bioethanol production, all these processes are far away from an economically feasible realization. Whereas ethanol could be produced with a rate of 87 mM_C d^{-1} up to an exceptionally high titer of 239 mM_C, already the second highest producer, butanediol, was produced with only a maximum rate of 17 mM_C d^{-1} to a final titer of 133 mM_C, while the strain producing isobutyraldehyde reached only rates of 8 mM_C d^{-1} and produced a final titer of 61 mM_C (Figure 5-1, Table 1-1). The realization of bioethanol production is favored by low downstream costs and a big potential market for low purity biofuel. Even so, ethanol can be taken as an example what becomes possible if there is a high interest in the development of a production process.

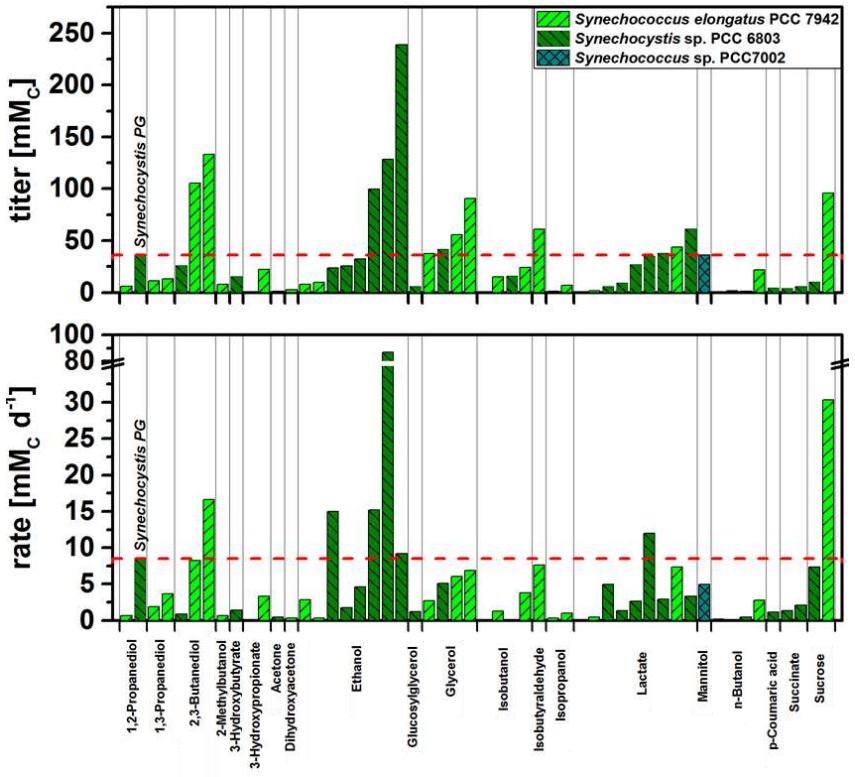

Figure 5-1: Product titers and rates of processes with cyanobacterial microbial cell factories

Product titer and production rate of *Synechocystis* PG in comparison to the performance of other cyanobacterial production strains (data taken from Table 1-1)

In comparison to these benchmark processes, the production capacity of 1,2-propanediol with *Synechocystis* PG is significantly lower (Figure 5-1, marked by a red and dotted line). Whereas the production rate within the stationary phase is high compared to the majority of published rates, the final titer is only slightly above the average.

The comparison to the 1,2-propanediol producing *Synechococcus* strain (Li and Liao, 2013) needs to consider the differences in strain background. The growth curve given for the recombinant *Synechococcus* strain is based on OD_{730} measurements, while this study used the optical density at 750 nm as a measure for the biomass concentration. Also, due to the differences in cell size and shape, the correlation factor of cell number to optical density deviates. However, in comparison, the titer and production rate of *Synechocystis* PG is significantly higher, while both strains produce the majority of the product during the stationary phase.

The same pattern, meaning the production of a majority of the product during the stationary phase, was also published for the three benchmark strains. Approximately 120 mM_C of ethanol and 60 mM_C 2, 3-butanediol were produced during the stationary phase. 2,3-butanediol was produced with a stable rate of 4.4 mM_C day^{-1} for 14 days. In the case of isobutyraldehyde, even 50 mM_C was produced in the stationary phase, almost 85% of the total product titer, with a stable rate of 7.2 mM_C day^{-1} for 6 days. This underlines the importance lying in the understanding of the underlying regulation leading to those carbon fluxes.

Nowadays, racemic 1,2-propanediol is produced by hydration of propylene oxide. Therefore, the precursor propylene oxide is either produced by the chlorohydrin process or the hydroperoxide process. Both processes are based on petrochemical resources, use hazardous chemicals, and produce unwanted byproducts (Saxena et al., 2010).

Biotechnological production of 1,2-propanediol has the advantages that it is based on renewable resources and that it does not apply hazardous chemicals. Additionally, biotechnological routes enable the enantioselective production of either the (R)- or (S)- enantiomer of 1,2-propanediol. Nevertheless, it is economically not competitive in comparison to the chemical process, due to the high costs of the raw materials (carbohydrates), slow reaction rates, and significantly lower product titers leading to higher downstream costs.

The fermentation of carbohydrates to 1,2-propanediol could be shown in different organisms, including recombinant strains like *E. coli, Corynebacterium glutamicum*, and *S. cerevisiae*, and wild-type strains like *Thermoanaerobacterium thermosaccharolyticum*. With the exception of

T. thermosaccharolyticum were up to 7.9 g L^{-1} were produced, the final titer was below 2 g L^{-1}. Additionally, the yield on glucose is relatively low because part of the glucose has to be used for biomass formation and to provide energy and reduction equivalents for the reaction. A maximal theoretical yield of 1.0 or 1.4 mol mol^{-1} glucose can be achieved under anaerobic or aerobic conditions, respectively (Cameron et al., 1998).

Alternatively, 1,2-propanediol can be produced from CO_2 by photoautotrophically growing strains as showed in this study. Thereby, there is no need for expensive carbon sources, and the light reactions of photosynthesis provide the energy. Photofermentative production of 1,2-propanediol could be established in *Synechococcus elongatus* PCC 7942 and 0.15 g L^{-1} were produced (Li and Liao, 2013). With the new biocatalyst *Synechocystis* PG developed in this study, the final titer could be improved to almost 1 g L^{-1}, which is close to the values reached in recombinant heterotrophic production processes.

Finally, photofermentative production of chemicals cannot compete with the space-time yield (STY) of a chemical process. Therefore, the cost reduction due to material input, reaction conditions, or the environmental benefit have to outweigh this drawback. At the current state, the performance of PMCFs is insufficient for an industrial application in general. A significant increase in final product titers is needed, which will require a better understanding of the carbon and energy fluxes in a photoautotrophic cell. An improved understanding might enable rational strain engineering to finally increase the titers of PMCFs to a point were commercial realization becomes feasible.

6 References

Al-Najjar M, de Beer D, Kühl M, Polerecky L. 2012. Light utilization efficiency in photosynthetic microbial mats. *Environ. Microbiol.* **14**: 982-992.

Van Alphen P, Najafabadi H, dos Santos F, Hellingwerf K. 2018. Increasing the photoautotrophic growth rate of *Synechocystis* sp. PCC 6803 by identifying the limitations of its cultivation. *Biotechnol. J*., **13**: 1700764.

Anfelt J, Kaczmarzyk D, Shabestary K, Renberg B, Uhlen M, Nielsen J, Hudson E. 2015. Genetic and nutrient modulation of acetyl-CoA levels in *Synechocystis* for n-butanol production. *Microb. Cell Fact.* **14**: 167.

Angermayr S, Gorchs Rovira A, Hellingwerf K. 2015. Metabolic engineering of cyanobacteria for the synthesis of commodity products. *Trends Biotechnol.* **33**: 352–361.

Angermayr S, Paszota M, Hellingwerf K. 2012. Engineering a cyanobacterial cell factory for production of lactic acid. *Appl. Environ. Microbiol.* **78**: 7098-7106.

Angermayr S, Van Der Woude A, Correddu D, Kern R, Hagemann M, Hellingwerf K. 2016a. Chirality matters: Synthesis and consumption of the D-enantiomer of lactic acid by *Synechocystis* sp. strain PCC 6803. *Appl. Environ. Microbiol.* **82**: 1295–1304.

Angermayr S, Van Alphen P, Hasdemir D, Kramer G, Iqbal M, Van Grondelle W, Hoefsloot H, Choi Y, Hellingwerf K. 2016b. Culturing *Synechocystis* sp. Strain PCC 6803 with N_2 and CO_2 in a Diel Regime Reveals Multiphase Glycogen Dynamics with Low Maintenance Costs. *Appl. Environ. Microbiol*. **82**: 4180–4189.

Aramrak S, Flury M, Harsh J. 2011. Detachment of deposited colloids by advancing and receding air-water interfaces. *Langmuir.* **27**: 9985–9993.

Beck C, Knoop H, Axmann I, Steuer R. 2012. The diversity of cyanobacterial metabolism: Genome analysis of multiple phototrophic microorganisms. *BMC Genomics.* **13**: 56.

Benschop J, Badger M, Price G. 2003. Characterisation of CO_2 and HCO_3^- uptake in the cyanobacterium *Synechocystis* sp . PCC 6803. *Photosynthesis Research*. **77**: 117–126.

Bertani G. 1951. Studies on lysogenesis. I. The mode of phage liberation by lysogenic *Escherichia coli*. *J. Bacteriol.* **62**: 293–300.

Blanken W, Postma P, de Winter L, Wijffels R, Janssen M. 2016. Predicting microalgae growth. *Algal Res.* **14**: 28–38.

Boks N, Norde W, van der Mei H, Busscher H. 2008. Forces involved in bacterial adhesion to hydrophilic and hydrophobic surfaces. *Microbiology* **154**: 3122–3133.

Bretherton F. 1961. The motion of long bubbles in tubes. *J. Fluid Mech.* **10**: 166.

Bridgwater A, Chinthapalli R, Smith P. 2010. Identification and market analysis of most promising added-value products to be co-produced with the fuels. *Ast. Univ.*: 1–132.

Cameron D, Altaras N, Hoffman M, Shaw A. 1998. Metabolic engineering of propanediol pathways. *Biotechnol. Prog.* **14**: 116–125.

Carpine R, Du W, Olivieri G, Pollio A, Hellingwerf K, Marzocchella A, Dos Santos F. 2017. Genetic engineering of *Synechocystis* sp. PCC 6803 for poly-β-hydroxybutyrate overproduction. *Algal Res.* **25**: 117–127.

Carvalho A, Meireles L, Malcata F. 2006. Microalgal reactors: a review of enclosed system designs and performances. *Biotechnol. Prog.* **22**: 1490–506.

Choi Y, Park J. 2015. Enhancing biomass and ethanol production by increasing NADPH production in *Synechocystis* sp. PCC 6803. *Bioresour. Technol.* **213**: 54–57.

Christenson L, Sims R. 2012. Rotating algal biofilm reactor and spool harvester for wastewater treatment with biofuels by-products. *Biotechnol. Bioeng.* **109**: 1674–1684.

Codd G, Stewart W. 1976. Proceedings of the Second International Symposium on Photosynthetic Prokaryotes. *FEMS*.

Cooper R. 1984. Metabolism of Methylglyoxal in Microorganisms. *Annu. Rev. Microbiol.* **38**: 49–68.

Daley S, Kappell A, Carrick M, Burnap R. 2012. Regulation of the cyanobacterial CO_2-concentrating mechanism involves internal sensing of $NADP^+$ and α-ketoglutarate levels by transcription factor CcmR. *PLoS One* **7**: e41286.

Dienst D, Dühring U, Mollenkopf H, Vogel J, Golecki J, Hess W, Wilde A. 2008. The cyanobacterial homologue of the RNA chaperone Hfq is essential for motility of *Synechocystis* sp. PCC 6803. *Microbiology* **154**:3134–3143.

Dunn K, Young P. 2006. Principles of multiphoton microscopy. *Nephron. Exp. Nephrol.* **103**: e33-40.

Ercan D, Pongtharangkul T, Demirci A, Pometto A. 2015. Applications of Biofilm Reactors for Production of Value - Added Products by Microbial Fermentation. *Biofilms in the Food Environment*.

European Commission. 2012. Innovating for Sustainable Growth: A Bioeconomy for Europe. *Communication*. Publications Office of the European Union.

Fenchel T, Kühl M. 2000. Artificial cyanobacterial mats: Growth, structure, and vertical zonation patterns. *Microb. Ecol.* **40**: 85–93.

Flemming H, Wingender J. 2010. The biofilm matrix. *Nat. Rev. Microbiol.* **8**:623–633.

Fresewinkel M, Rosello R, Wilhelm C, Kruse O, Hankamer B, Posten C. 2014. Integration in microalgal bioprocess development: Design of efficient, sustainable, and economic processes. *Eng. Life Sci.* **14**: 560-573.

Gao Z, Zhao H, Li Z, Tan X, Lu X. 2012. Photosynthetic production of ethanol from carbon dioxide in genetically engineered cyanobacteria. *Energy Environ. Sci.* **5:** 9857–9865.

Gerritsen H, De Grauw C. 1999. Imaging of optically thick specimen using two-photon excitation microscopy. *Microsc. Res. Tech.* **47**: 206–209.

Gibson D, Young L, Chuang R, Venter J, Hutchison C, Smith H. 2009. Enzymatic assembly of DNA

molecules up to several hundred kilobases. *Nat. Methods* 6: 343–345.

Gitelson A, Hu Q, Richmond A. 1996. Photic volume in photobioreactors supporting ultrahigh population densities of the photoautotroph *Spirulina platensis*. *Appl. Environ. Microbiol.* 62: 1570–1573.

Gross R, Buehler K, Schmid A. 2013. Engineered catalytic biofilms for continuous large scale production of n-octanol and (S)-styrene oxide. *Biotechnol. Bioeng.* 110: 424–436.

Gründel M, Scheunemann R, Lockau W, Zilliges Y. 2012. Impaired glycogen synthesis causes metabolic overflow reactions and affects stress responses in the cyanobacterium *Synechocystis* sp. PCC 6803. *Microbiol.* 158: 3032–3043.

Halan B, Buehler K, Schmid A. 2012. Biofilms as living catalysts in continuous chemical syntheses. *Trends Biotechnol.* 30: 453–65.

Halan B, Schmid A, Buehler K. 2011. Real-time solvent tolerance analysis of *Pseudomonas* sp. strain VLB120ΔC catalytic biofilms. *Appl. Environ. Microbiol.* 77: 1563–71.

Hasunuma T, Matsuda M, Kondo A. 2016. Improved sugar-free succinate production by *Synechocystis* sp. PCC 6803 following identification of the limiting steps in glycogen catabolism. *Metab. Eng. Commun.* 3: 130–141.

Hays S, Ducat D. 2015. Engineering cyanobacteria as photosynthetic feedstock factories. *Photosynth. Res.* 123: 285–295.

Heidorn T, Camsund D, Huang H, Lindberg P, Oliveira P, Stensjö K, Lindblad P. 2011. Synthetic biology in cyanobacteria: engineering and analyzing novel functions. *Methods Enzymol.* 497: 539-579.

Hirokawa Y, Suzuki I, Hanai T. 2015. Optimization of isopropanol production by engineered cyanobacteria with a synthetic metabolic pathway. *J. Biosci. Bioeng.* 119: 585–590.

Hopper D, Cooper R. 1971. The regulation of *Escherichia coli* methylglyoxal synthase; a new control site in glycolysis? *FEBS Lett.* 13:213–216.

Hu Q, Kurano N, Kawachi M, Iwasaki I, Miyachi S. 1998. Ultrahigh-cell-density culture of a marine green alga *Chlorococcum littorale* in a flat-plate photobioreactor. *Appl. Microbiol. Biotechnol.* 49: 655–662.

Huang H, Camsund D, Lindblad P, Heidorn T. 2010. Design and characterization of molecular tools for a Synthetic Biology approach towards developing cyanobacterial biotechnology. *Nucleic Acids Res.* 38: 2577–2593.

Huang H, Lindblad P. 2013. Wide-dynamic-range promoters engineered for cyanobacteria. *J. Biol. Eng.* 7: 10.

Huang K, Rudolph F, Bennett G. 1999. Characterization of Methylglyoxal Synthase from *Clostridium acetobutylicum* ATCC 824 and Its Use in the Formation of 1,2-Propanediol. *Appl. Environ. Microbiol*. 65: 3244–3247.

Kaneko T, Tabata S. 1997. Complete Genome Structure of the Unicellular Cyanobacterium *Synechocystis* sp. PCC 6803. *Plant Cell Physiol* **38**: 1171–1176.

Karande R, Halan B, Schmid A, Buehler K. 2014. Segmented flow is controlling growth of catalytic biofilms in continuous multiphase microreactors. *Biotechnol. Bioeng.* **111**: 1831-1840.

Klok A, Verbaanderd J, Lamers P, Martens D, Rinzema A, Wijffels R. 2013. A model for customising biomass composition in continuous microalgae production. *Bioresour. Technol.* **146**: 89–100.

Knoop H, Gründel M, Zilliges Y, Lehmann R, Hoffmann S, Lockau W, Steuer R. 2013. Flux Balance Analysis of Cyanobacterial Metabolism: The Metabolic Network of *Synechocystis* sp. PCC 6803. *PLoS Comput. Biol.* **9**: e1003081.

König K. 2000. Multiphoton microscopy in life sciences. *J. Microsc.* **200**: 83–104.

Kopecna J, Komenda J, Bucinska L, Sobotka R. 2012. Long-Term Acclimation of the Cyanobacterium *Synechocystis* sp. PCC 6803 to High Light Is Accompanied by an Enhanced Production of Chlorophyll That Is Preferentially Channeled to Trimeric Photosystem I. *Plant Physiol.* **160**: 2239–2250.

Kühl M, Fenchel T. 2000. Bio-optical characteristics and the vertical distribution of photosynthetic pigments and photosynthesis in an artificial cyanobacterial mat. *Microb. Ecol.* **40**: 94–103.

Kühl M, Glud R, Ploug H, Ramsing N. 1996. Microenvironmental Control of Photosynthesis and Photosynthesis-coupled Respiration in an Epilithic Cyanobacterial Biofilm. *J. Phycol.* **32**: 799–812.

Kuhne S, Lakatos M, Foltz S, Muffler K, Ulber R. 2013. Characterization of terrestrial cyanobacteria to increase process efficiency in low energy consuming production processes. *Sustain. Chem. Process.* **1**: 6.

Kumar K, Dasgupta C, Nayak B, Lindblad P, Das D. 2011. Development of suitable photobioreactors for CO2 sequestration addressing global warming using green algae and cyanobacteria. *Bioresour. Technol.* **102**: 4945–4953.

Kusakabe T, Tatsuke T, Tsuruno K, Hirokawa Y, Atsumi S, Liao J, Hanai T. 2013. Engineering a synthetic pathway in cyanobacteria for isopropanol production directly from carbon dioxide and light. *Metab. Eng.* **20**: 101–108.

Lakins M, Marrison J, O'Toole P, van der Woude M. 2009. Exploiting advances in imaging technology to study biofilms by applying multiphoton laser scanning microscopy as an imaging and manipulation tool. *J. Microsc.* **235**: 128–137.

Lan E, Liao J. 2011. Metabolic engineering of cyanobacteria for 1-butanol production from carbon dioxide. *Metab. Eng.* **13**: 353–363.

Laurens L, Melodie C, McMillan J. 2017. A perspective on renewable bioenergy from photosynthetic algae as feedstock for biofuels and bioproducts. *Algal Research.* **24**: 261-264

Li H, Liao J. 2013. Engineering a cyanobacterium as the catalyst for the photosynthetic conversion of CO_2 to 1,2-propanediol. *Microb. Cell Fact.* **12**: 4.

van Loosdrecht M, Heijnen S. 1993. Biofilm bioreactors for waste-water treatment. *Trends Biotechnol.* **11**: 117–121.

Marco-Urrea E, Paul S, Khodaverdi V, Seifert J, von Bergen M, Kretzschmar U, Adrian L. 2011. Identification and characterization of a Re-citrate synthase in *Dehalococcoides* strain CBDB1. *J. Bacteriol.* **193**: 5171–5178.

Mariné M, Clavero E, Roldán M. 2004. Microscopy methods applied to research on cyanobacteria. *Limnetica* **23**: 179–186.

Martínez L, Morán A, García A. 2011. Effect of light on *Synechocystis* sp. and modelling of its growth rate as a response to average irradiance. *J. Appl. Phycol.* **24**: 125–134.

Mazard S, Penesyan A, Ostrowski M, Paulsen I, Egan S. 2016. Tiny microbes with a big impact: The role of cyanobacteria and their metabolites in shaping our future. *Mar. Drugs* **14**: 97.

McCormick A, Bombelli P, Scott A, Philips A, Smith A, Fisher A, Howe C. 2011. Photosynthetic biofilms in pure culture harness solar energy in a mediatorless bio-photovoltaic cell (BPV) system. *Energy Environ. Sci.* **4**: 4699.

McEwen J, Kanno M, Atsumi S. 2016. 2,3-Butanediol production in an obligate photoautotrophic cyanobacterium in dark conditions via diverse sugar consumption. *Metab. Eng.* **36**: 28–36.

Miao R, Liu X, Englund E, Lindberg P, Lindblad P. 2017. Isobutanol production in *Synechocystis* PCC 6803 using heterologous and endogenous alcohol dehydrogenases. *Metab. Eng. Commun.* **5**: 45–53.

Millero F, Graham T, Huang F, Bustos-Serrano H, Pierrot D. 2006. Dissociation constants of carbonic acid in seawater as a function of salinity and temperature. *Mar. Chem.* **100**: 80–94.

Mizuta Y, Kurihara D, Higashiyama T. 2015. Two-photon imaging with longer wavelength excitation in intact *Arabidopsis* tissues. *Protoplasma* **252**: 1231–1240.

Monroe D. 2007. Looking for chinks in the armor of bacterial biofilms. *PLoS Biol.* **5**: 2458–2461.

Monshupanee T, Incharoensakdi A. 2014. Enhanced accumulation of glycogen, lipids and polyhydroxybutyrate under optimal nutrients and light intensities in the cyanobacterium *Synechocystis* sp. PCC 6803. *J. Appl. Microbiol.* **116**: 830–838.

Nägeli C. 1849. Gattungen einzelliger Algen physiologisch und systematisch bearbeitet. *Neue Denkschriften der Allg. Schweizerischen Gesellschaft für die Gesammten Naturwissenschaften* **10**: 1-139.

Namakoshi K, Nakajima T, Yoshikawa K, Toya Y, Shimizu H. 2016. Combinatorial deletions of *glgC* and *phaCE* enhance ethanol production in *Synechocystis* sp. PCC 6803. *J. Biotechnol.* **239**: 13–19.

Narala R, Garg S, Sharma K, Thomas-Hall S, Deme M, Li Y, Schenk P. 2016. Comparison of Microalgae Cultivation in Photobioreactor, Open Raceway Pond, and a Two-Stage Hybrid System. *Front. Energy Res.* **4**: 1–10.

Neu T, Woelfl S, Lawrence J. 2004a. Three-dimensional differentiation of photo-autotrophic biofilm constituents by multi-channel laser scanning microscopy (single-photon and two-photon excitation). *J. Microbiol. Methods* **56**: 161–172.

Neu T, Walczysko P, Lawrence J. 2004b. Minireview Two-Photon Imaging for Studying the Microbial Ecology of Biofilm Systems. *Microbes Environ.* **19**: 1–6.

Ng W, Bassler B. 2009. Bacterial quorum-sensing network architectures. *Annu. Rev. Genet.* **43**: 197–222.

Niederholtmeyer H, Wolfstädter B, Savage D, Silver P, Way J. 2010. Engineering cyanobacteria to synthesize and export hydrophilic products. *Appl. Environ. Microbiol.* **76**: 3462–3466.

Oliver J, Atsumi S. 2014. Metabolic design for cyanobacterial chemical synthesis. *Photosynth. Res.* **120**: 249–261.

Oliver J, Machado I, Yoneda H, Atsumi S. 2013. Cyanobacterial conversion of carbon dioxide to 2,3-butanediol. *Proc. Natl. Acad. Sci. U. S. A.* **110**: 1249–1254.

Pinto F, Thapper A, Sontheim W, Lindblad P. 2009. Analysis of current and alternative phenol based RNA extraction methodologies for cyanobacteria. *BMC Mol. Biol.* **10**: 79.

Quan Y, Zhang L, Qi R, Cai R. 2016. Self-cleaning of Surfaces: The role of surface wettability and dust types. *Sci. Rep.* **6**: 1–12.

Quek L, Wittmann C, Nielsen L, Krömer J. 2009. OpenFLUX: Efficient modelling software for ^{13}C-based metabolic flux analysis. *Microb. Cell Fact.* **8:** 25.

Qureshi N, Annous B, Ezeji T, Karcher P, Maddox I. 2005. Biofilm reactors for industrial bioconversion process: Employing potential of enhanced reaction rates. *Microb. Cell Fact.* **4**: 1–21.

Roeselers G, Van Loosdrecht M, Muyzer G. 2008. Phototrophic biofilms and their potential applications. *J. Appl. Phycol.* **20**: 227–235.

Rosche B, Li X, Hauer B, Schmid A, Buehler K. 2009. Microbial biofilms: a concept for industrial catalysis? *Trends Biotechnol.* **27**: 636–643.

Rubart M. 2004. Two-photon microscopy of cells and tissue. *Circ. Res.* **95**: 1154–1166.

Ruffing A, Jensen T, Strickland L. 2016. Genetic tools for advancement of *Synechococcus* sp. PCC 7002 as a cyanobacterial chassis. *Microb. Cell Fact.* **15**: 1–14.

Sander R. 2015. Compilation of Henry's law constants (version 4.0) for water as solvent. *Atmos. Chem. Phys.* **15**: 4399–4981.

Savakis P, Angermayr S, Hellingwerf K. 2013. Synthesis of 2,3-butanediol by *Synechocystis* sp. PCC 6803 via heterologous expression of a catabolic pathway from lactic acid- and enterobacteria. *Metab. Eng.* **20**: 121–130.

Savakis P, Hellingwerf K. 2015. Engineering cyanobacteria for direct biofuel production from CO_2. *Curr. Opin. Biotechnol.* **33**: 8–14.

Saxena R, Anand P, Saran S, Isar J, Agarwal L. 2010. Microbial production and applications of 1,2-propanediol. *Indian J. Microbiol.* **50**: 2–11.

Schatz D, Nagar E, Sendersky E, Parnasa R, Zilberman S, Carmeli S, Mastai Y, Shimoni E, Klein E, Yeger O, Reich Z, Schwarz R. 2013. Self-suppression of biofilm formation in the cyanobacterium *Synechococcus elongatus*. *Environ. Microbiol.* **15**: 1786–1794.

Schipp C, Marco-Urrea E, Kublik A, Seifert J, Adrian L. 2013. Organic cofactors in the metabolism of *Dehalococcoides mccartyi* strains. *Philos. Trans. R. Soc. B Biol. Sci.* **368**: 20120321.

Schulze K, López D, Tillich U, Frohme M. 2011. A simple viability analysis for unicellular cyanobacteria using a new autofluorescence assay, automated microscopy, and ImageJ. *BMC Biotechnol.* **11**: 118.

Schuurmans R, Matthijs J, Hellingwerf K. 2017. Transition from exponential to linear photoautotrophic growth changes the physiology of *Synechocystis* sp. PCC 6803. *Photosynth. Res.* **132**: 69–82.

Shastri A, Morgan J. 2005. Flux balance analysis of photoautotrophic metabolism. *Biotechnol. Prog.* **21**: 1617–1626.

Shcolnick S, Shaked Y, Keren N. 2007. A role for *mrgA*, a DPS family protein, in the internal transport of Fe in the cyanobacterium *Synechocystis* sp. PCC 6803. *Biochim. Biophys. Acta - Bioenerg.* **1767**: 814–819.

Shimakawa G, Suzuki M, Yamamoto E, Nishi A, Saito R, Sakamoto K, Yamamoto H, Makino A, Miyake C. 2013. Scavenging Systems for Reactive Carbonyls in the Cyanobacterium *Synechocystis* sp. PCC 6803. *Biosci. Biotechnol. Biochem.* **77**: 2441–2448.

Stanier R, Kunisawa R, Mandel M, Cohen-Bazire G. 1971. Purification and properties of unicellular blue-green algae (Order *Chroococcales*). *Bacteriol. Rev.* **35**: 171–205.

Steinhauser D, Fernie A, Araújo W. 2012. Unusual cyanobacterial TCA cycles: not broken just different. *Trends Plant Sci.* **17**: 503–509.

Suhag M, Sharma H. 2015. Biorefinery Concept: An Overview of Producing Energy, Fuels and Materials from Biomass Feedstocks. *Iarjset* **2**: 103–109.

Sutherland J, Herdman M, Stewart W. 1979. Akinetes of the Cyanobacterium *Nostoc* PCC 7524: Macromolecular Composition, Structure and Control of Differentiation. *J. Gen. Microbiol.* **115**: 273–287.

Taroncher-Oldenburg G, Nishina K, Stephanopoulos G. 2000. Identification and analysis of the polyhydroxyalkanoate-specific beta-ketothiolase and acetoacetyl coenzyme A reductase genes in the cyanobacterium *Synechocystis* sp. strain PCC 6803. *Appl. Environ. Microbiol.* **66**: 4440–4448.

Tilzer M. 1987. Light-dependence of photosynthesis and growth in cyanobacteria: Implications for their dominance in eutrophic lakes. *New Zeal. J. Mar. Freshw. Res.* **21**: 401–412.

Tolker-Nielsen T, Sternberg C. 2011. Growing and Analyzing Biofilms in Flow Chambers. *Curr. Protoc. Microbiol.* **21**: 1B.2.1-1B.2.17.

Tötemeyer S, Booth N, Nichols W, Dunbar B, Booth I. 1998. From famine to feast: The role of methylglyoxal production in *Escherichia coli*. *Mol. Microbiol.* **27**: 553–562.

Trautmann A, Watzer B, Wilde A, Forchhammer K, Posten C. 2016. Effect of phosphate availability on cyanophycin accumulation in *Synechocystis* sp. PCC 6803 and the production strain BW86. *Algal Res.* **20**: 189–196.

Varman A, Xiao Y, Pakrasi H, Tang Y. 2013a. Metabolic engineering of *Synechocystis* sp. strain PCC 6803 for isobutanol production. *Appl. Environ. Microbiol.* **79**: 908–914.

Varman A, Yu Y, You L, Tang Y. 2013b. Photoautotrophic production of D-lactic acid in an engineered cyanobacterium. *Microb. Cell Fact.* **12**: 117.

Vermaas W, Timlin J, Jones H, Sinclair M, Nieman L, Hamad S, Melgaard D, Haaland D. 2008. In vivo hyperspectral confocal fluorescence imaging to determine pigment localization and distribution in cyanobacterial cells. *Proc. Natl. Acad. Sci.* **105**: 4050–4055.

Wang B, Pugh S, Nielsen D, Zhang W, Meldrum D. 2013. Engineering cyanobacteria for photosynthetic production of 3-hydroxybutyrate directly from CO_2. *Metab. Eng.* **16**: 68-77.

Wang B, Wang J, Zhang W, Meldrum D. 2012. Application of synthetic biology in cyanobacteria and algae. *Front. Microbiol.* **3**:344.

Wang Y, Tao F, Ni J, Li C, Xu P. 2015. Production of C3 platform chemicals from CO_2 by genetically engineered cyanobacteria. *Green Chem.* **17**: 3100–3110.

Wijffels R, Kruse O, Hellingwerf K. 2013. Potential of industrial biotechnology with cyanobacteria and eukaryotic microalgae. *Curr. Opin. Biotechnol.* **24**: 1–9.

Williams J. 1988. Construction of specific mutations in photosystem II photosynthetic reaction center by genetic engineering methods in *Synechocystis* 6803. *Methods Enzymol.* **167**: 766-778.

Wingender J, Neu T, Flemming H. 1999. Microbial Extracellular Polymeric Substances. *Microb. Extracell. Polym. Subst.* 1–19.

Wolf G, Picioreanu C, van Loosdrecht M. 2007. Kinetic modeling of phototrophic biofilms: The PHOBIA model. *Biotechnol. Bioeng.* **97**: 1064–1079.

Van der Woude A, Angermayr S, Puthan Veetil V, Osnato A, Hellingwerf K. 2014. Carbon sink removal: Increased photosynthetic production of lactic acid by *Synechocystis* sp. PCC 6803 in a glycogen storage mutant. *J. Biotechnol.* **184**: 100–102.

Yan Y, Lee C, Liao J. 2009. Enantioselective synthesis of pure (R,R)-2,3-butanediol in *Escherichia coli* with stereospecific secondary alcohol dehydrogenases. *Org. Biomol. Chem.* **7**: 3914.

Yu J, Liberton M, Cliften P, Head R, Jacobs J, Smith R, Koppenaal D, Brand J, Pakrasi H. 2015. *Synechococcus elongatus* UTEX 2973, a fast growing cyanobacterial chassis for biosynthesis using light and CO2. *Sci. Rep.* **5**: 8132.

Yu Y, You L, Liu D, Hollinshead W, Tang Y, Zhang F. 2013. Development of *Synechocystis* sp. PCC 6803 as a phototrophic cell factory. *Mar. Drugs* **11**: 2894–916.

Zavřel T, Sinetová M., Búzová D, Literáková P, Červený J. 2014. Characterization of a model cyanobacterium *Synechocystis* sp. PCC 6803 autotrophic growth in a flat-panel photobioreactor. *Eng. Life Sci.* **15**: 122–132.

Zevenboom W, de Groot G, Mur L. 1980. Effects of light on nitrate-limited *Oscillatoria agardhii* in chemostat cultures. *Arch. Microbiol.* **125**: 59–65.

Zhou J, Zhang H, Meng H, Zhang Y, Li Y. 2014. Production of optically pure d-lactate from CO_2 by blocking the PHB and acetate pathways and expressing d-lactate dehydrogenase in cyanobacterium *Synechocystis* sp. PCC 6803. *Process Biochem.* **49**: 12–21.

Zhou J, Zhang H, Zhang Y, Li Y, Ma Y. 2012. Designing and creating a modularized synthetic pathway in cyanobacterium *Synechocystis* enables production of acetone from carbon dioxide. *Metab. Eng.* **14**: 394–400.

Zippel B, Neu T. 2005. Growth and structure of phototrophic biofilms under controlled light conditions. *Water Sci. Technol.* **52**: 203–209.

Zippel B, Rijstenbil J, Neu T. 2007. A flow-lane incubator for studying freshwater and marine phototrophic biofilms. *J. Microbiol. Methods* **70**: 336–345.

7 Appendix

7.1 List of abbreviations

Abbreviation	Meaning
1,3-BPG	1,3-bisphosphoglycerate
AB	antibiotics
Amp	ampicillin
ATP	adenosine triphosphate
BCP	1-bromo-3-chloropropane
BSTFA	N,O-bis-trimethylsilyl-trifluoroacetamide
CDW	cell dry weight
CLSM	confocal laser scanning microscopy
CoA	coenzyme A
CP	circular pond
DHAP	dihydroxyacetone phosphate
DIC	dissolved inorganic carbon
DMSO	dimethyl sulfoxide
FDM	fused deposition modeling
FDR	false discovery rate
FPBR	flat-panel photobioreactor
FPR	flat-panel reactor
G1P	glucose-1-phosphate
GAP	glyceraldehyde-3-phosphate
GAPDH	glyceraldehyde-3-phosphate dehydrogenase
GFP	green fluorescent protein
GLG	glycogen
Gly	glycogen
GMO	genetically modified organism
HC	high carbon
HeTR	helical tubular reactor
HL	high light
HTR	horizontal tubular reactor
IPTG	isopropyl β-D-1-thiogalactopyranoside
Km	kanamycin
LC	low carbon
LED	light emitting diodes
LL	low light
MBDSTFA	N-methyl-N-tert-butyldimethylsilyl-trifluoroacetamide
MFC	mass flow controller
NADH	nicotinamide adenine dinucleotide
NADPH	nicotinamide adenine dinucleotide phosphate
NIR	near-infrared

Abbreviation	Meaning
OD	optical density
OD_{750}	optical density at 750 nm
PA	polyamide
PAR	photosynthetic active radiation
PCR	polymerase chain reaction
PDO	1,2-propanediol
PG	propylene glycol
PHB	polyhydroxybutyrate
PLA	polylactic acid
PMFC	photosynthetic microbial cell factory
RP	raceway pond
RuBisCO	ribulose-1,5-bisphosphate carboxylase/oxygenase
SLS	selective laser sintering
Sm	streptomycin
SPE	single-photon excitation
STPBR	stirred tank photobioreactor
STR	stirred tank reactor
Synechococcus	*Synechococcus elongatus PCC 7942*
Synechocystis	*Synechocystis sp. PCC 6803*
Tc	tetracycline
TCA cycle	tricarboxylic acid cycle
TFA	trifluoroacetic acid
TMCS	trimethylchlorosilane
TPE	two-photon excitation
TR	tubular reactor
VTR	vertical tubular reactor
vvm	volume volume^{-1} minute^{-1}
αTR	alpha-shaped tubular reactor

7.2 List of symbols

Symbol	Meaning	Unit
c	concentration	mol L^{-1}
$c_{cell\ \#}$	concentration based on cell number	10^8 ml^{-1}
c_I	correction factor	-
c_{max}	maximal concentration	mol L^{-1}
$^{13}CO_2$	labeled CO_2	-
$^{n}CO_2$	natural CO_2	-
c_x	biomass concentration	mol l^{-1}
D_H	hydraulic diameter	mm
g_{CDW}	mass of cell dry weight	g
H	water film thickness	µm
H_{CO2}^{cp}	Henry coefficient for CO_2	mol m^{-3} Pa^{-1}
I	light intensity	µmol m^{-2} s^{-1}
I_0	initial incident light intensity	µmol m^{-2} s^{-1}
J_{CO2}	diffusion flux of CO_2	mol m^{-2} s^{-1}
K_0	overall light attenuation coefficient	mm^{-1}
K_1, K_2	equilibrium constant	varying
k_LA	volumetric gas transfer coefficient	m^{-2} s^{-1}
m	mass	g
Mc	c-molar concentration	mol C L^{-1}
$OD_{750,max}$	maximal OD_{750} measurement	-
p	pressure	bar
p_{CO2}	partial pressure of CO_2	bar
r	rate, either production or turnover	mM_C d^{-1}
R	gas constant	J $K^{-1}mol^{-1}$
r_L	linear growth rate	h^{-1}
r_{max}	maximum rate	mM_C d^{-1}
R_P	radius of the particle	µm
S	salinity	g_{salts} $kg_{solution}^{-1}$
T	temperature	Kelvin
v	flow velocity	mm min^{-1}
$Y_{P/S}$	yield of product on CO_2	-
$Y_{P/X}$	yield of product on biomass	-
z	position	-

Greek symbols

Symbol	Meaning	Unit
α_x	biomass specific light absorption coefficient	$m^2 \cdot mol^{-1}$
$\boldsymbol{\gamma}$	surface tension of water	$N\ m^{-1}$
μ	exponential growth rate based on OD_{750} measurements	h^{-1}
$\mu_{cell\ \#}$	exponential growth rate based on cell number	h^{-1}
μ_v	dynamic viscosity of water	Pa s
$\sin\phi\ \sin(\theta-\phi)$	filling angle and contact angle	-

7.3 List of figures

7.4 List of tables

7.5 Additional figures and tables

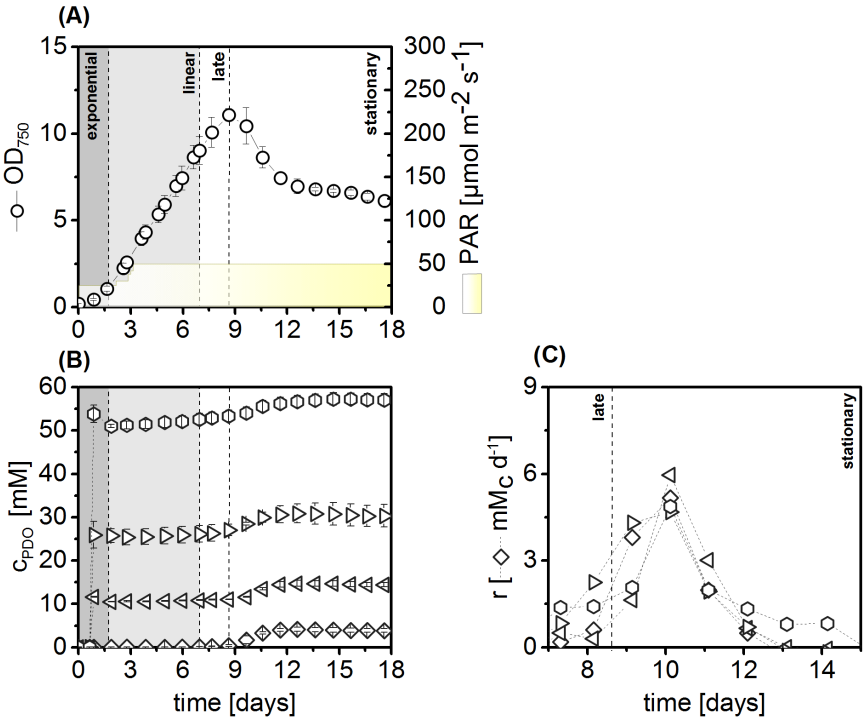

Figure 7-1: Growth and production after addition of varying amounts of 1,2-propanediol

(A) Growth (OD_{750}) of *Synechocystis* PG cultures in YBG11 after addition of 0, 10, 25, 50 mM 1,2-propanediol **(B)** 1,2-propanediol concentrations during cultivation. Mean values and standard deviation of 2 biological replicates are shown **(C)** 1,2-propanediol production rates.

Table 7-1: Abundance and ranking of YqhD (Accession number NP_417484.1) and Adh (Accession number WP_077844196.1) as detected by mass spectroscopy.

Proteins have been ranked according to their abundance. In total 1195 proteins have been identified. Only Protein #1 to 24 and #124 to 150 are shown. MgsA could not be detected. F1 and F2 refer to wt samples. PG refer to the recombinant *Synechocystis* PG. Two biological replicates have been measured. PG 1.1 and 2.1 = day 3.8; PG1.2 and 2.2 = day 5.9; PG1.3 and 2.3 = day 8.06; PG1.4 und 2.4 = day 10.9.

#	Accession #	Sum PEP Score	# Unique Peptides	Abundance Ratio: $wt_{(F2)/(F1)}$	PG 1.1	PG2.1	PG1.2	PG2.2	PG1.3	PG2.3	PG1.4	PG2.4	avgRank
1	**Q54714**	311,857	23	0,932	1	1	1	1	1	1	1	1	1,0
2	**Q54715**	284,207	23	0,958	2	2	2	2	2	2	2	2	2,0
3	**Q01952**	278,208	20	0,984	3	3	3	3	3	3	3	3	3,0
4	**Q01951**	169,796	15	1,053	4	4	4	4	4	4	4	4	4,0
5	**Q05972**	341,677	34	0,829	7	6	5	5	5	5	6	6	5,6
6	**P73203**	132,131	17	0,981	5	5	6	6	9	7	7	7	6,5
7	**P73093**	121,484	15	1,021	6	7	8	7	7	8	5	5	6,6
8	**P22034**	330,376	28	0,839	12	12	7	10	6	6	8	8	8,6
9	**P74227**	275,944	25	0,955	9	9	9	8	10	10	10	10	9,4
10	**Q55544**	328,16	39	0,893	11	14	10	9	8	9	9	9	9,9
11	**P77961**	302,147	24	0,912	10	10	11	11	11	11	11	11	10,8
12	**P54205**	154,647	21	0,855	8	8	17	12	14	14	16	16	13,1
13	**P73348**	133,666	13	0,836	17	19	12	14	12	12	15	12	14,1
14	**P73204**	88,044	12	0,993	14	15	15	13	16	17	14	15	14,9
15	**P80505**	131,602	16	0,935	13	11	14	15	20	15	18	17	15,4
16	**P22358**	396,299	35	0,884	27	29	13	18	13	13	12	13	17,3
17	**P73282**	261,862	23	1,038	18	17	16	17	17	16	22	21	18,0
18	**Q55013**	102,162	9	1,038	19	18	23	24	18	21	17	20	20,0
19	**P77972**	151,419	15	0,919	21	20	18	21	23	19	21	18	20,1
20	**P26527**	261,304	25	0,926	23	25	19	22	22	18	20	22	21,4
21	**P54206**	97,673	8	0,867	15	13	25	23	24	24	29	29	22,8
22	**NP_417484.1**	**157,843**	**15**		**38**	**38**	**30**	**28**	**19**	**20**	**13**	**14**	**25,0**
23	**P74421**	193,193	19	1,063	16	16	22	20	30	32	31	33	25,0

#	Accession#	Sum PEP Score	# Unique Peptides	Abundance Ratio: $wt_{(F2)\,/\,(F1)}$	PG 1.1	PG2.1	PG1.2	PG2.2	PG1.3	PG2.3	PG1.4	PG2.4	avgRank
124	Q55386	69,465	7	1,04	106	123	78	85	110	139	184	196	127,6
125	P73307	37,938	6	0,992	72	72	131	125	170	144	170	149	129,1
126	P74267	30,629	3	1,144	116	139	110	126	127	108	156	168	131,3
127	P74296	111,459	15	1	137	158	120	124	119	117	148	158	135,1
128	P74229	39,574	5	0,977	91	82	153	131	160	165	160	161	137,9
129	P74467	32,466	4	0,779	200	218	158	147	96	122	81	87	138,6
130	P74426	20,38	4	0,555	144	127	133	183	138	153	143	120	142,6
131	P74226	45,712	7	0,715	105	99	151	137	149	160	178	173	144,0
132	P48944	28,576	3	0,781	93	107	147	128	158	157	198	166	144,3
133	P73320	64,731	9	1,055	76	88	148	143	134	176	193	201	144,9
134	P73201	102,659	14	0,952	159	157	144	140	144	135	150	139	146,0
135	P49433	61,014	8	0,762	220	204	150	151	116	128	107	105	147,6
136	P27724	1,381	1	0,969	132	122	107	132	198	146	179	183	149,9
137	P72661	104,849	10	1,061	187	166	165	168	135	150	120	119	151,3
138	P73312	34,586	4	0,953	142	171	141	150	114	138	173	181	151,3
139	Q55665	76,196	10	0,893	108	100	193	158	157	195	157	160	153,5
140	P73530	47,3	7	0,887	111	118	152	144	177	154	208	194	157,3
141	P17253	86,986	11	1,083	166	146	191	173	142	156	139	145	157,3
142	P73971	146,81	15	0,901	296	277	171	156	88	131	65	77	157,6
143	Q55770	77,56	11	1,33	261	256	164	180	113	104	104	96	159,8
144	P74266	63,948	5	1,092	146	143	157	152	151	147	194	195	160,6
145	Q55385	54,769	4	1,056	123	104	155	148	210	173	181	197	161,4
146	**WP_077844196.1**	**37,147**	**6**		**182**	**227**	**192**	**175**	**91**	**102**	**260**	**75**	**163,0**
147	P72673	54,128	7	1,113	193	206	160	160	174	161	119	132	163,1
148	P74466	32,842	4	0,889	217	215	167	188	125	148	123	123	163,3
149	P73058	115,803	14	0,633	173	170	176	177	171	162	142	138	163,6
150	P52231	35,199	5	0,628	94	86	122	257	163	198	220	170	163,8

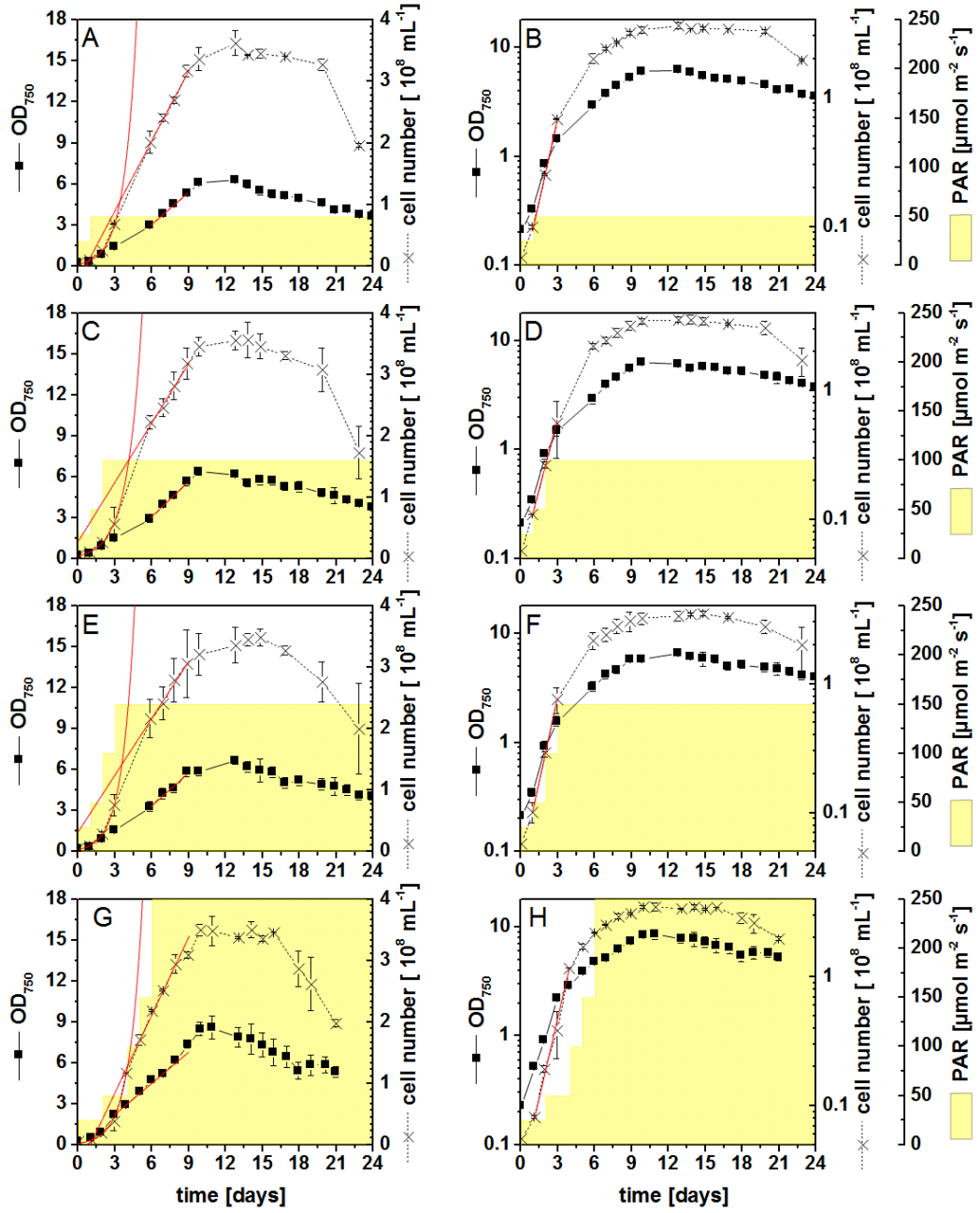

Figure 7-2: Influence of different light intensities on the growth of *Synechocystis* PG in an atmosphere with ambient CO_2

Optical density and cell concentration on a linear (**left column**) and logarithmic scale (**right column**) measured during shaking flask cultivations with *Synechocystis* PG. The light intensity is increased stepwise during cultivation. The final light intensities supplied were 50, 100, 150, and 250 µmol m^{-2} s^{-1}, increasing from the top to the bottom row. Cultivation took place at 30°C, 150 rpm, 75% humidity, and under ambient CO_2 in the atmosphere.

7.6 List of publications

This work was in parts previously published in peer-reviewed journals and presented as contribution to scientific conferences.

7.6.1 Peer-reviewed articles

David C, Bühler K and Schmid A. 2015. Stabilization of single species *Synechocystis* biofilms by cultivation under segmented flow. *J. Ind. Microbiol. Biotechnol.* 42:1083–1089.

David C, Schmid A, Adrian L, Wilde A and Bühler K. 2018. Production of 1,2-propanediol in photoautotrophic *Synechocystis* is linked to glycogen turn-over. *Biotechnol. Bioeng.* 115:300–311.

David C, Heuschkel I, Bühler K and Karande K. 2018. Cultivation of productive Biofilms in flow-reactors and their characterization by CLSM. Submitted

David C, Schmid A and Bühler K. 2018. Cellular physiology controls photoautotrophic production of 1,2-propanediol from pools of CO_2 and glycogen. Submitted

David C, Schmid A and Bühler K. 2018. CO_2 uptake during 1,2-propanediol production in 2 L photobioreactors. In preparation

7.6.2 Oral presentations

David, C., Wilde, A, Schmid, A and Bühler, K. Glycogen content defines propylene glycol production capacity in *Synechocystis*. International Solar Fuels 2017, San Diego, USA (2017)

7.6.3 Poster

David C, Schmid A and Bühler K. Recombinant *Synechocystis* biofilms for CO_2 based 1,2-propanediol production. Biofilms 7, Porto, Portugal (2016)

David C, Grund M, Bühler B, Bühler K and Schmid A. Applied Biocatalysis & Bio-Artificial Photosynthesis. POF III Evaluation Meeting, Berlin, Germany (2014)

Maaß M, David C, Altmann S and Bühler K. Cyanobacterial biofilms: Exploiting the potential of CO_2 as a non-fossil carbon source for the production of high value compounds. Biofilms 7, Porto, Portugal (2016)

Bühler K, David C and Schmid A. Stabilization of single species *Synechocystis* biofilms by hydrodynamic stress. 1st International Solar Fuels Conference, Uppsala, Sweden (2015)

7.7 Curriculum vitae

Personal data

Name	Christian David
Born	31.08.1983 in Meerbusch, Germany
Nationality	German

Education

01/2014-09/2018	**PhD Student** at the Department of Solar Materials, Helmholtz Centre for Environmental Research, Leipzig, Germany, under the supervision of Prof. Dr. Katja Bühler and Prof. Dr. Andreas Schmid
07/2013-12/2013	**PhD Student** at the Faculty of Biochemical and Chemical Engineering, TU Dortmund University, Germany, under the supervision of Prof. Dr. Andreas Schmid and Dr. Katja Bühler
10/2004-05/2013	**Studies in Biochemical Engineering**, Faculty of Biochemical and Chemical Engineering, TU Dortmund University, Germany Degree: Diplomingenieur
10/2003-07/2004	**Basic military service**, Luftwaffensanitätsstaffel, Jagdbombergeschwader 31, Cologne, Germany
08/1994-06/2003	**Gymnasium** Marienschule Krefeld, Krefeld, Germany Degree: Abitur